PHYSICAL REVIEW C **84**, 044905 (2011)

Heavy-quark production in $p + p$ and energy loss and flow of heavy quarks in Au + Au collisions at $\sqrt{s_{NN}} = 200$ GeV

A. Adare,[9] S. Afanasiev,[24] C. Aidala,[10] N. N. Ajitanand,[51] Y. Akiba,[45,46] H. Al-Bataineh,[40] J. Alexander,[51] A. Al-Jamel,[40] K. Aoki,[30,45] L. Aphecetche,[53] R. Armendariz,[40] S. H. Aronson,[4] J. Asai,[46] E. T. Atomssa,[31] R. Averbeck,[52] T. C. Awes,[41] B. Azmoun,[4] V. Babintsev,[19] G. Baksay,[15] L. Baksay,[15] A. Baldisseri,[12] K. N. Barish,[5] P. D. Barnes,[33,*] B. Bassalleck,[39] S. Bathe,[5] S. Batsouli,[10,41] V. Baublis,[44] F. Bauer,[5] A. Bazilevsky,[4] S. Belikov,[4,23,*] R. Bennett,[52] Y. Berdnikov,[48] A. A. Bickley,[9] M. T. Bjorndal,[10] J. G. Boissevain,[33] H. Borel,[12] K. Boyle,[52] M. L. Brooks,[33] D. S. Brown,[40] D. Bucher,[36] H. Buesching,[4] V. Bumazhnov,[19] G. Bunce,[4,46] J. M. Burward-Hoy,[33] S. Butsyk,[33,52] S. Campbell,[52] J.-S. Chai,[25] B. S. Chang,[60] J.-L. Charvet,[12] S. Chernichenko,[19] J. Chiba,[26] C. Y. Chi,[10] M. Chiu,[10,20] I. J. Choi,[60] T. Chujo,[57] P. Chung,[51] A. Churyn,[19] V. Cianciolo,[41] C. R. Cleven,[17] Y. Cobigo,[12] B. A. Cole,[10] M. P. Comets,[42] P. Constantin,[23,33] M. Csanád,[14] T. Csörgő,[27] T. Dahms,[52] K. Das,[16] G. David,[4] M. B. Deaton,[1] K. Dehmelt,[15] H. Delagrange,[53] A. Denisov,[19] D. d'Enterria,[10] A. Deshpande,[46,52] E. J. Desmond,[4] O. Dietzsch,[49] A. Dion,[52] M. Donadelli,[49] J. L. Drachenberg,[1] O. Drapier,[31] A. Drees,[52] A. K. Dubey,[59] A. Durum,[19] V. Dzhordzhadze,[5,54] Y. V. Efremenko,[41] J. Egdemir,[52] F. Ellinghaus,[9] W. S. Emam,[5] A. Enokizono,[18,32] H. En'yo,[45,46] B. Espagnon,[42] S. Esumi,[56] K. O. Eyser,[5] D. E. Fields,[39,46] M. Finger Jr.,[6,24] M. Finger,[6,24] F. Fleuret,[31] S. L. Fokin,[29] B. Forestier,[34] Z. Fraenkel,[59,*] J. E. Frantz,[10,52] A. Franz,[4] A. D. Frawley,[16] K. Fujiwara,[45] Y. Fukao,[30,45] S.-Y. Fung,[5] T. Fusayasu,[38] S. Gadrat,[34] I. Garishvili,[54] F. Gastineau,[53] M. Germain,[53] A. Glenn,[9,54] H. Gong,[52] M. Gonin,[31] J. Gosset,[12] Y. Goto,[45,46] R. Granier de Cassagnac,[31] N. Grau,[23] S. V. Greene,[57] M. Grosse Perdekamp,[20,46] T. Gunji,[8] H.-Å. Gustafsson,[35,*] T. Hachiya,[18,45] A. Hadj Henni,[53] C. Haegemann,[39] J. S. Haggerty,[4] M. N. Hagiwara,[1] H. Hamagaki,[8] R. Han,[43] H. Harada,[18] E. P. Hartouni,[32] K. Haruna,[18] M. Harvey,[4] E. Haslum,[35] K. Hasuko,[45] R. Hayano,[8] M. Heffner,[32] T. K. Hemmick,[52] T. Hester,[5] J. M. Heuser,[45] X. He,[17] H. Hiejima,[20] J. C. Hill,[23] R. Hobbs,[39] M. Hohlmann,[15] M. Holmes,[57] W. Holzmann,[51] K. Homma,[18] B. Hong,[28] T. Horaguchi,[45,55] D. Hornback,[54] M. G. Hur,[25] T. Ichihara,[45,46] H. Iinuma,[30,45] K. Imai,[30,45] M. Inaba,[56] Y. Inoue,[45,47] D. Isenhower,[1] L. Isenhower,[1] M. Ishihara,[45] T. Isobe,[8] M. Issah,[51] A. Isupov,[24] B. V. Jacak,[52,†] J. Jia,[10] J. Jin,[10] O. Jinnouchi,[46] B. M. Johnson,[4] K. S. Joo,[37] D. Jouan,[42] F. Kajihara,[8,45] S. Kametani,[8,58] N. Kamihara,[45,55] J. Kamin,[52] M. Kaneta,[46] J. H. Kang,[60] H. Kanou,[45,55] T. Kawagishi,[56] D. Kawall,[46] A. V. Kazantsev,[29] S. Kelly,[9] A. Khanzadeev,[44] J. Kikuchi,[58] D. H. Kim,[37] D. J. Kim,[60] E. Kim,[50] Y.-S. Kim,[25] E. Kinney,[9] Á. Kiss,[14] E. Kistenev,[4] A. Kiyomichi,[45] J. Klay,[32] C. Klein-Boesing,[36] L. Kochenda,[44] V. Kochetkov,[19] B. Komkov,[44] M. Konno,[56] D. Kotchetkov,[5] A. Kozlov,[59] A. Král,[11] A. Kravitz,[10] P. J. Kroon,[4] J. Kubart,[6,22] G. J. Kunde,[33] N. Kurihara,[8] K. Kurita,[45,47] M. J. Kweon,[28] Y. Kwon,[54,60] G. S. Kyle,[40] R. Lacey,[51] Y. S. Lai,[10] J. G. Lajoie,[23] A. Lebedev,[23] Y. Le Bornec,[42] S. Leckey,[52] D. M. Lee,[33] M. K. Lee,[60] T. Lee,[50] M. J. Leitch,[33] M. A. L. Leite,[49] B. Lenzi,[49] H. Lim,[50] T. Liška,[11] A. Litvinenko,[24] M. X. Liu,[33] X. Li,[7] X. H. Li,[5] B. Love,[57] D. Lynch,[4] C. F. Maguire,[57] Y. I. Makdisi,[3,4] A. Malakhov,[24] M. D. Malik,[39] V. I. Manko,[29] Y. Mao,[43,45] L. Mašek,[6,22] H. Masui,[56] F. Matathias,[10,52] M. C. McCain,[20] M. McCumber,[52] P. L. McGaughey,[33] Y. Miake,[56] P. Mikeš,[6,22] K. Miki,[45,56] T. E. Miller,[57] A. Milov,[52] S. Mioduszewski,[4] G. C. Mishra,[17] M. Mishra,[2] J. T. Mitchell,[4] M. Mitrovski,[51] A. Morreale,[5] D. P. Morrison,[4] J. M. Moss,[33] T. V. Moukhanova,[29] D. Mukhopadhyay,[57] J. Murata,[45,47] S. Nagamiya,[26] Y. Nagata,[56] J. L. Nagle,[9] M. Naglis,[59] I. Nakagawa,[45,46] Y. Nakamiya,[18] T. Nakamura,[18] K. Nakano,[45,55] J. Newby,[32] M. Nguyen,[52] B. E. Norman,[33] R. Nouicer,[4] A. S. Nyanin,[29] J. Nystrand,[35] E. O'Brien,[4] S. X. Oda,[8] C. A. Ogilvie,[23] H. Ohnishi,[45] I. D. Ojha,[57] K. Okada,[46] M. Oka,[56] O. O. Omiwade,[1] A. Oskarsson,[35] I. Otterlund,[35] M. Ouchida,[18,45] K. Ozawa,[8] R. Pak,[4] D. Pal,[57] A. P. T. Palounek,[33] V. Pantuev,[21,52] V. Papavassiliou,[40] J. Park,[50] W. J. Park,[28] S. F. Pate,[40] H. Pei,[23] J.-C. Peng,[20] H. Pereira,[12] V. Peresedov,[24] D. Yu. Peressounko,[29] C. Pinkenburg,[4] R. P. Pisani,[4] M. L. Purschke,[4] A. K. Purwar,[33,52] H. Qu,[17] J. Rak,[23,39] A. Rakotozafindrabe,[31] I. Ravinovich,[59] K. F. Read,[41,54] S. Rembeczki,[15] M. Reuter,[52] K. Reygers,[36] V. Riabov,[44] Y. Riabov,[44] G. Roche,[34] A. Romana,[31,*] M. Rosati,[23] S. S. E. Rosendahl,[35] P. Rosnet,[34] P. Rukoyatkin,[24] V. L. Rykov,[45] S. S. Ryu,[60] B. Sahlmueller,[36] N. Saito,[30,45,46] T. Sakaguchi,[4,8,58] S. Sakai,[56] H. Sakata,[18] V. Samsonov,[44] H. D. Sato,[30,45] S. Sato,[4,26,56] S. Sawada,[26] J. Seele,[9] R. Seidl,[20] V. Semenov,[19] R. Seto,[5] D. Sharma,[59] T. K. Shea,[4] I. Shein,[19] A. Shevel,[44,51] T.-A. Shibata,[45,55] K. Shigaki,[18] M. Shimomura,[56] T. Shohjoh,[56] K. Shoji,[30,45] A. Sickles,[52] C. L. Silva,[49] D. Silvermyr,[41] C. Silvestre,[12] K. S. Sim,[28] C. P. Singh,[2] V. Singh,[2] S. Skutnik,[23] M. Slunečka,[6,24] W. C. Smith,[1] A. Soldatov,[19] R. A. Soltz,[32] W. E. Sondheim,[33] S. P. Sorensen,[54] I. V. Sourikova,[4] F. Staley,[12] P. W. Stankus,[41] E. Stenlund,[35] M. Stepanov,[40] A. Ster,[27] S. P. Stoll,[4] T. Sugitate,[18] C. Suire,[42] J. P. Sullivan,[33] J. Sziklai,[27] T. Tabaru,[46] S. Takagi,[56] E. M. Takagui,[49] A. Taketani,[45,46] K. H. Tanaka,[26] Y. Tanaka,[38] K. Tanida,[45,46,50] M. J. Tannenbaum,[4] A. Taranenko,[51] P. Tarján,[13] T. L. Thomas,[39] M. Togawa,[30,45] A. Toia,[52] J. Tojo,[45] L. Tomášek,[22] H. Torii,[45] R. S. Towell,[1] V.-N. Tram,[31] I. Tserruya,[59] Y. Tsuchimoto,[18,45] S. K. Tuli,[2,*] H. Tydesjö,[35] N. Tyurin,[19] C. Vale,[23] H. Valle,[57] H. W. van Hecke,[33] J. Velkovska,[57] R. Vértesi,[13] A. A. Vinogradov,[29] M. Virius,[11] V. Vrba,[22] E. Vznuzdaev,[44] M. Wagner,[30,45] D. Walker,[52] X. R. Wang,[40] Y. Watanabe,[45,46] J. Wessels,[36] S. N. White,[4] N. Willis,[42] D. Winter,[10] C. L. Woody,[4] M. Wysocki,[9] W. Xie,[5,46] Y. L. Yamaguchi,[58] A. Yanovich,[19] Z. Yasin,[5] J. Ying,[17] S. Yokkaichi,[45,46] G. R. Young,[41] I. Younus,[39] I. E. Yushmanov,[29] W. A. Zajc,[10] O. Zaudtke,[36] C. Zhang,[10,41] S. Zhou,[7] J. Zimányi,[27,*] and L. Zolin[24]
(PHENIX Collaboration)

[1]*Abilene Christian University, Abilene, Texas 79699, USA*
[2]*Department of Physics, Banaras Hindu University, Varanasi 221005, India*
[3]*Collider-Accelerator Department, Brookhaven National Laboratory, Upton, New York 11973-5000, USA*
[4]*Brookhaven National Laboratory, Upton, New York 11973-5000, USA*
[5]*University of California-Riverside, Riverside, California 92521, USA*
[6]*Charles University, Ovocný trh 5, Praha 1, 116 36, Prague, Czech Republic*
[7]*Science and Technology on Nuclear Data Laboratory, China Institute of Atomic Energy, Beijing 102413, People's Republic of China*
[8]*Center for Nuclear Study, Graduate School of Science, University of Tokyo, 7-3-1 Hongo, Bunkyo, Tokyo 113-0033, Japan*
[9]*University of Colorado, Boulder, Colorado 80309, USA*
[10]*Columbia University, New York, New York 10027 and Nevis Laboratories, Irvington, New York 10533, USA*
[11]*Czech Technical University, Zikova 4, 166 36 Prague 6, Czech Republic*
[12]*Dapnia, CEA Saclay, F-91191, Gif-sur-Yvette, France*
[13]*Debrecen University, H-4010 Debrecen, Egyetem tér 1, Hungary*
[14]*ELTE, Eötvös Loránd University, H-1117 Budapest, Pázmány P. s. 1/A, Hungary*
[15]*Florida Institute of Technology, Melbourne, Florida 32901, USA*
[16]*Florida State University, Tallahassee, Florida 32306, USA*
[17]*Georgia State University, Atlanta, Georgia 30303, USA*
[18]*Hiroshima University, Kagamiyama, Higashi-Hiroshima 739-8526, Japan*
[19]*IHEP Protvino, State Research Center of Russian Federation, Institute for High Energy Physics, Protvino, 142281, Russia*
[20]*University of Illinois at Urbana-Champaign, Urbana, Illinois 61801, USA*
[21]*Institute for Nuclear Research of the Russian Academy of Sciences, Prospekt 60-letiya Oktyabrya 7a, Moscow 117312, Russia*
[22]*Institute of Physics, Academy of Sciences of the Czech Republic, Na Slovance 2, 182 21 Prague 8, Czech Republic*
[23]*Iowa State University, Ames, Iowa 50011, USA*
[24]*Joint Institute for Nuclear Research, Dubna, Moscow Region, 141980, Russia*
[25]*KAERI, Cyclotron Application Laboratory, Seoul, Korea*
[26]*KEK, High Energy Accelerator Research Organization, Tsukuba, Ibaraki 305-0801, Japan*
[27]*KFKI Research Institute for Particle and Nuclear Physics of the Hungarian Academy of Sciences (MTA KFKI RMKI),*
H-1525 Budapest 114, P.O. Box 49, Budapest, Hungary
[28]*Korea University, Seoul 136-701, Korea*
[29]*Russian Research Center "Kurchatov Institute," Moscow 123098, Russia*
[30]*Kyoto University, Kyoto 606-8502, Japan*
[31]*Laboratoire Leprince-Ringuet, Ecole Polytechnique, CNRS-IN2P3, Route de Saclay, F-91128, Palaiseau, France*
[32]*Lawrence Livermore National Laboratory, Livermore, California 94550, USA*
[33]*Los Alamos National Laboratory, Los Alamos, New Mexico 87545, USA*
[34]*LPC, Université Blaise Pascal, CNRS-IN2P3, Clermont-Fd, F-63177 Aubiere Cedex, France*
[35]*Department of Physics, Lund University, Box 118, SE-221 00 Lund, Sweden*
[36]*Institut für Kernphysik, University of Muenster, D-48149 Muenster, Germany*
[37]*Myongji University, Yongin, Kyonggido 449-728, Korea*
[38]*Nagasaki Institute of Applied Science, Nagasaki-shi, Nagasaki 851-0193, Japan*
[39]*University of New Mexico, Albuquerque, New Mexico 87131, USA*
[40]*New Mexico State University, Las Cruces, New Mexico 88003, USA*
[41]*Oak Ridge National Laboratory, Oak Ridge, Tennessee 37831, USA*
[42]*IPN-Orsay, Universite Paris Sud, CNRS-IN2P3, BP1, F-91406, Orsay, France*
[43]*Peking University, Beijing 100871, People's Republic of China*
[44]*PNPI, Petersburg Nuclear Physics Institute, Gatchina, Leningrad Region 188300, Russia*
[45]*RIKEN Nishina Center for Accelerator-Based Science, Wako, Saitama 351-0198, Japan*
[46]*RIKEN BNL Research Center, Brookhaven National Laboratory, Upton, New York 11973-5000, USA*
[47]*Physics Department, Rikkyo University, 3-34-1 Nishi-Ikebukuro, Toshima, Tokyo 171-8501, Japan*
[48]*Saint Petersburg State Polytechnic University, St. Petersburg 195251, Russia*
[49]*Universidade de São Paulo, Instituto de Física, Caixa Postal 66318, São Paulo CEP05315-970, Brazil*
[50]*Seoul National University, Seoul, Korea*
[51]*Chemistry Department, Stony Brook University, Stony Brook, SUNY, New York 11794-3400, USA*
[52]*Department of Physics and Astronomy, Stony Brook University, SUNY, Stony Brook, New York 11794, USA*
[53]*SUBATECH (Ecole des Mines de Nantes, CNRS-IN2P3, Université de Nantes) BP 20722, F-44307 Nantes, France*
[54]*University of Tennessee, Knoxville, Tennessee 37996, USA*
[55]*Department of Physics, Tokyo Institute of Technology, Oh-okayama, Meguro, Tokyo 152-8551, Japan*
[56]*Institute of Physics, University of Tsukuba, Tsukuba, Ibaraki 305, Japan*
[57]*Vanderbilt University, Nashville, Tennessee 37235, USA*

[58]*Waseda University, Advanced Research Institute for Science and Engineering, 17 Kikui-cho, Shinjuku-ku, Tokyo 162-0044, Japan*
[59]*Weizmann Institute, Rehovot 76100, Israel*
[60]*Yonsei University, IPAP, Seoul 120-749, Korea*

(Received 17 May 2010; revised manuscript received 1 March 2011; published 10 October 2011)

Transverse momentum spectra of electrons (p_T^e) from semileptonic weak decays of heavy-flavor mesons in the range of $0.3 < p_T^e < 9.0$ GeV/c have been measured at midrapidity ($|y| < 0.35$) by the PHENIX experiment at the Relativistic Heavy Ion Collider in $p + p$ and Au + Au collisions at $\sqrt{s_{NN}} = 200$ GeV. In addition, the azimuthal anisotropy parameter v_2 has been measured for $0.3 < p_T^e < 5.0$ GeV/c in Au + Au collisions. The substantial modification in the p_T^e spectra in Au + Au compared with $p + p$ collisions as well as the nonzero v_2 indicate substantial interactions and flow of heavy quarks in traversing the produced medium. Comparisons of these observables with detailed theoretical calculations can be used to identify the nature of these interactions and to quantify their extent.

DOI: 10.1103/PhysRevC.84.044905 PACS number(s): 25.75.Dw

I. INTRODUCTION

Experimental results from the Relativistic Heavy Ion Collider (RHIC) at Brookhaven National Laboratory (BNL) have firmly established that the matter created in central Au + Au collisions at $\sqrt{s_{NN}} = 200$ GeV can neither be explained as a hadron gas nor as a weakly interacting gas of quarks and gluons at very high densities [1–4]. Strong suppression observed in measurements of the nuclear modification factor R_{AA} as function of the transverse momentum p_T for light-flavor hadrons shows that high-p_T scattered partons suffer a significant energy loss in the medium [5–7]. The large magnitude of elliptic flow v_2 and its p_T and mass dependencies show qualitative agreement with the theoretical predictions for an ideal hydrodynamic fluid [8–11]. These observations indicate that the medium is strongly interacting and exhibits nearly perfect fluid behavior. However, qualitative evidence for a near-perfect hydrodynamic fluid is not sufficient to extract quantitative values for thermodynamic and transport properties [12,13]. The issue is how perfect is the fluidity observed at RHIC. The validation of the perfect fluidity requires the ratio of shear viscosity η to entropy density s to be small, perhaps at the conjectured lower bound of $1/4\pi$ (in natural units) [14].

Heavy quarks (charm and bottom) are important probes of the dense matter formed at RHIC. Because of their large masses, their dominant production mechanism is restricted to parton-parton collisions in the initial stage of the reaction, and it is expected that next-to-leading-order perturbative QCD (NLO pQCD) calculations can describe the production cross section of charm and bottom at high energy, particularly at high p_T. Charm production cross sections at high p_T are found to be higher than such calculations by ≈50%, which is still compatible with the theoretical uncertainties [15]. At the Tevatron with $\sqrt{s} = 1.8$ TeV, bottom production is well described by NLO pQCD [16].

In heavy-ion collisions, after the heavy quarks are produced, they then interact with the medium. It has been predicted that the radiative energy loss of heavy quarks would be smaller than that of light quarks and gluons owing to suppression of small-angle gluon radiation, called the "dead cone effect" [17,18]. Recently, the contribution of other interaction mechanisms such as collisional energy loss and in-medium fragmentation have also been calculated. Another approach is to assume very strong interactions with the medium and treat the heavy quark via diffusion calculations. In these models, the heavy-quark diffusion coefficient D^{HQ} controls the extent to which the initial power-law p_T spectrum from perturbative QCD calculations approaches the thermal spectrum and the extent to which the heavy quark will follow the underlying flow of the medium. Simultaneous measurement of the heavy-quark $R_{AA}(p_T^e)$ and $v_2(p_T^e)$ can provide an estimate of this D^{HQ}, which can be related to the fluidity measure η/s.

There are several ways to measure heavy-quark production. The most direct method is to reconstruct D or B mesons from their decay products, such as $D \to K\pi$ or $B \to J/\psi K$. PHENIX is currently not capable of measuring the displaced decay vertex of the heavy meson, which makes this method challenging because of the low signal-to-background ratio. In the analysis presented here, the measurement is via single electrons from heavy-flavor decay. Both the charm and bottom mesons (D, B) have relatively large branching ratios (∼10%) to single electrons or single muons.

Single electrons in hadronic collisions were first observed in the early 1970s in $\sqrt{s} = 52.7$ GeV $p + p$ collisions at the CERN ISR [19] before the discovery of charm. In $p\bar{p}$ collisions at $\sqrt{s} = 630$ GeV, UA1 [20] measured bottom production via single muons and UA2 [21] reported the charm cross section from single-electron measurements. At the Tevatron collider, the CDF [22] and D0 [23] experiments measured bottom production via single muons or single electrons.

At RHIC, PHENIX first measured charm production in Au + Au collisions at $\sqrt{s_{NN}} = 130$ GeV via the measurement of single electrons [24]. Subsequently, PHENIX reported results from 2002 data of single electron measurements in $p + p$ collisions [25] and Au + Au collisions [26–28] at midrapidity. In Au + Au collisions at $\sqrt{s_{NN}} = 200$ GeV the total yield of heavy-flavor decay electrons was found to scale with the number of binary nucleon-nucleon collisions [26], as expected for a pointlike process. In contrast, a strong suppression of heavy-flavor electrons for $2 < p_T < 5$ GeV/c [28] and a nonzero electron v_2 for $p_T < 2$ GeV/c [27] were discovered.

---

[*] Deceased.

[†] jacak@skipper.physics.sunysb.edu

This article presents measurements of single electrons $[(N_{e^+} + N_{e^-})/2]$ from semileptonic decays of heavy quarks (charm and bottom) at midrapidity ($|y| < 0.35$) in $p + p$ and Au + Au collisions at $\sqrt{s_{NN}} = 200$ GeV. The data were collected in 2004 (Au + Au) and 2005 ($p + p$). We extend the previous PHENIX analyses of electron measurements in $p + p$ and Au + Au collisions at $\sqrt{s_{NN}} = 200$ GeV to a broader p_T^e range, $0.3 < p_T^e < 9.0$ GeV/c, and with a much higher precision. A subset of these results has been published in Refs. [29,30].

This article is organized as follows. Section II presents an overview of the PHENIX detector system related to the analysis. Section III presents the details of the data analysis. Section IV shows the fully corrected p_T^e distributions from $p + p$ and Au + Au collisions and the elliptic flow v_2 in Au + Au collisions. Section V compares the measurements with various theoretical predictions and discusses the physics implications. Finally, Sec. VI gives a brief summary.

II. PHENIX DETECTOR

A detailed description of the complete PHENIX detector system can be found elsewhere [31–36]. Here we describe the parts of the detector system that are used in this analysis, namely, two global detectors and two central arm spectrometers. The global detectors are the beam-beam counter (BBC) and the zero-degree calorimeter (ZDC). The electron measurements are made with two central arm spectrometers that each cover pseudorapidity $|\eta| < 0.35$ and azimuthal angle $\Delta\phi = \pi/2$. They contain the drift chamber (DC) and the multiwire proportional pad chamber (PC) for charged-particle tracking, the ring-imaging Čerenkov detector (RICH) for electron identification, and the electromagnetic calorimeter (EMCal) for energy measurement. Figure 1 shows the beam view of the PHENIX detector.

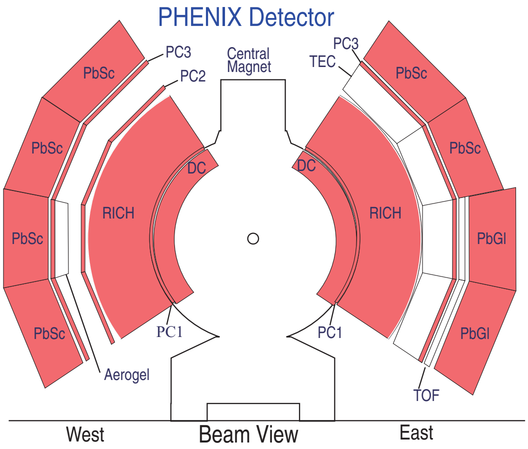

FIG. 1. (Color online) Beam view (at $z = 0$) of the PHENIX central arm detector in 2004 (Au + Au) and 2005 ($p + p$). The detectors used in the present analysis are the drift chamber (DC) and the multiwire proportional pad chambers (PC1, PC2, PC3) for charged particle tracking, the ring-imaging Čerenkov detector (RICH) for electron identification, and the electromagnetic calorimeters, which are lead glass (PbGl) and lead scintillator (PbSc), for energy measurement.

A. Global detectors

The BBC and the ZDC measure the collision time and the collision vertex position z_{vtx} along the beam axis. In Au + Au collisions, they are used to determine the centrality of the collision [36] and the azimuthal orientation of the reaction plane. They also provide the first level, minimum-bias (MB) trigger information for beam-beam collisions.

Two sets of BBCs are placed at ±1.44 m from the nominal interaction point along the beam line (one on the north side and one on the south). Each BBC comprises 64 Čerenkov counter modules, arranged radially around the beam pipe. Each module is made of a 3-cm-long quartz radiator and a photomultiplier tube (PMT). The PMTs can operate in a high magnetic field (∼0.3 T) that lies mostly parallel to the beam axis. The BBC is sensitive to the charged-particle multiplicity within pseudorapidity $3.0 < |\eta| < 3.9$. The vertex position resolution of the BBC is ∼0.6 cm for Au + Au collisions and ∼2.0 cm in $p + p$ collisions.

The ZDC measures the total energy carried by the forward neutrons produced along the beam direction. These neutrons are produced either by Coulomb dissociation of the beam particles or by evaporation from beam spectators. The ZDCs are placed at ±18 m from the interaction point along the beam line. The angular acceptance of each ZDC is $|\theta| < 2$ mrad ($|\eta| > 6$). Each ZDC comprises three modules of two-interaction-length-deep tungsten-quartz Čerenkov sampling calorimeters. The energy resolution of the ZDC is $\delta E/E \sim 218/\sqrt{E(\mathrm{GeV})}\%$ [37].

B. Central magnet

The transverse momentum of each charged particle is determined by its bending curvature in the magnetic field provided by the PHENIX central magnet (CM) system [32]. The CM is energized by two pairs of concentric coils and provides an axial magnetic field parallel to the beam pipe. The coils can be run with the fields for the two coil sets adding (the "++" and "−−" configurations) or canceling ("+−" configuration). During the Au + Au measurement in 2004 and the $p + p$ measurement in 2005, the CM was operated in the "++" and "−−" configurations. In these configurations, the field component parallel to the beam axis has an approximately Gaussian dependence on the radial distance from the beam axis, dropping from 0.9 T at the center to 0.096 T (0.048 T) at the inner (outer) radius of the DCs. The total field integral is $\int B \cdot dl = 1.15$ T m.

C. Tracking detectors

The DC and PC [33] in the central arms measure charged particle trajectories in the azimuthal direction to determine the transverse momentum (p_T) of each particle. By combining with the p_T the polar angle information from the innermost PC (PC1) and the vertex position along the beam line from the BBC, the total momentum (p) is determined.

The DC is positioned between 2.02 and 2.46 m in radial distance from the z axis for both the west and east arms. Each DC covers pseudorapidity $|\eta| < 0.35$ and $\pi/2$ in azimuth. Both DC volumes comprise 20 sectors, each of which covers 4.5°

in azimuth. Each sector has six types of wire modules stacked radially, named X1, U1, V1, X2, U2, and V2. Each module is further divided into four drift cells in the ϕ direction. A plane of sense wires is at the center of a drift cell, with 2 to 2.5 cm drift space. The X wires run parallel to the beam axis and measure the particle trajectory in the r-ϕ plane. The U and V wires have a stereo angle of about 6.0° relative to the X wires to measure the z coordinate of the track. The single X wire resolution is $\sigma \sim 150\ \mu$m. The intrinsic tracking efficiency of the X modules is greater than 99%. Helium bags were placed between the beam pipe and the DCs to reduce photon conversions and multiple scattering.

The PCs determine three-dimensional space points along the straight line particle trajectories outside the magnetic field. They are multiwire proportional chambers that form three separate layers of the central tracking system. The first PC layer (PC1) is located between the DC and RICH at 2.47–2.52 m in radial distance from the beam axis, while the third layer (PC3) is located in front of EMCal, occupying 4.91–4.98 m from the beam axis. The second layer (PC2) is at 4.15–4.21 m in radial distance in the west arm only.

D. Ring-imaging Čerenkov detector

The RICH is a threshold-type gas Čerenkov counter and the primary detector used to identify electrons in PHENIX [34,38]. It is located in the radial region of 2.5–4.1 m. The RICH in each central arm covers pseudorapidity $|\eta| < 0.35$ and $\pi/2$ in azimuth. Each volume contains mirror panels (0.53% of a radiation length thick), forming two intersecting spherical surfaces, with a total reflecting area of 20 m^2. The spherical mirrors focus Čerenkov light onto two arrays of $80(\phi) \times 16(z) = 1280$ PMTs, each located on either side of the RICH entrance window, as shown in Fig. 2. Each PMT has a magnetic shield that allows it to operate in a magnetic field up to 100 G. CO$_2$ gas at atmospheric pressure ($n = 1.000\,410$) is used as the Čerenkov radiator. The RICH has a Čerenkov threshold of $\gamma = 35$, which corresponds to $p > 20$ MeV/c for electrons and $p > 4.9$ GeV/c for charged pions. The average number of hit PMTs per electron track is ~5, and the average number of photoelectrons detected is ~10. Below the pion threshold the e/π separation is $\sim 10^4$ in low-occupancy $p + p$ collisions.

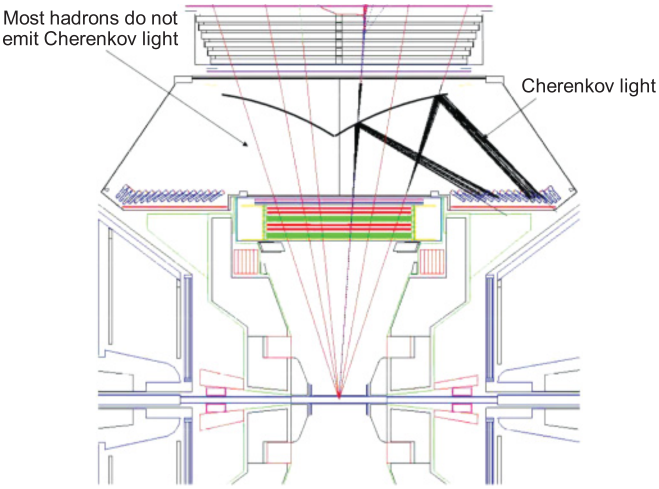

FIG. 2. (Color online) Top view (at $y = 0$) of the RICH in the PHENIX east arm.

E. Electromagnetic calorimeter

The EMCal [35] comprises two arms, each covering pseudorapidity $|\eta| < 0.35$ and $\pi/2$ in azimuth. Each of the two arms comprises four rectangular sectors. The two lowest sectors of the east arm are based on lead-glass (PbGl) calorimetry, whereas the remaining six sectors are based on lead-scintillator (PbSc) calorimetry. The radial distance from the z axis is 5.10 m for PbSc and 5.50 m for PbGl.

The PbSc is a Shashlik-type sampling calorimeter made of alternating tiles of lead and scintillator that comprises 15 552 individual towers and covers an area of approximately 48 m^2. It comprises 3888 rectangular modules ($10.5 \times 10.5 \times 37$cm^3), each of which is constructed from alternating layers of 1.5-mm-thick lead and 4-mm polystyrene-based scintillator. The light from the scintillator is collected by wavelength shifter fibers that run longitudinally through the module volume and are brought to four PMTs in the back end. This structure divides each module into four equal square cross-section towers, from which the light is collected separately by the fibers. The angular segmentation of PbSc is $\Delta\phi \times \Delta\eta \sim 0.01 \times 0.01$. The nominal energy resolution is $\delta E/E \sim 4.5\% \oplus 8.3/\sqrt{E(\mathrm{GeV})}\%$.

The PbGl comprises 9216 rectangular modules ($4 \times 4 \times 40$ cm^3), each of which is assembled from four PbGl crystals. Light emitted by particles depositing energy in the crystals is collected by a PMT at the back of each crystal. The angular segmentation of PbSc is $\Delta\phi \times \Delta\eta \sim 0.008 \times 0.008$. The PbGl has a nominal energy resolution of $\delta E/E \sim 4.3\% \oplus 7.7/\sqrt{E(\mathrm{GeV})}\%$.

The EMCal served as the electron trigger device in the 2005 $p + p$ data taking. This particular trigger is used for photons and electrons and is referred to as the PH trigger. The PH trigger fires whenever the energy sum in a 4×4 sum of EMCal towers (called a trigger tile) exceeds a threshold of 1.4 GeV. All trigger bits output from the trigger tiles are summed in each super module online. Because there are 172 EMCal supermodules (108 PbSc + 64 PbGl), the PH trigger has 172 output channels. Of them, 95% were active in the 2005 $p + p$ data. All the output bit information is summed and used for the event-trigger decision. The trigger efficiency evaluation is described in Sec. III G.

III. ANALYSIS

A. Data set and event selection (Au + Au)

The data for Au + Au collisions at $\sqrt{s_{\mathrm{NN}}} = 200$ GeV were taken during the 2004 run of RHIC. The MB trigger was defined as

$$\mathrm{MB} \equiv (\mathrm{BBC} \geqslant 2)\&(|\mathrm{bbc}z| < 38\ \mathrm{cm}). \tag{1}$$

Here BBC $\geqslant 2$ means that at least two hits are required in both the north and the south BBCs. The offline event selection also requires at least one hit in one of the ZDCs to remove a small remaining background contribution. The MB trigger efficiency for inelastic Au + Au collisions is evaluated as $92.2^{+2.5}_{-3.0}\%$ [39]. The vertex position, bbc$z$, along the beam line is determined online from the timing difference between the two BBCs.

In the offline analysis, a tighter BBC reconstructed vertex cut ($|\text{bbc}z| < 20$ cm) is required to eliminate conversion electrons from forward materials. The Au + Au MB data sample used for the analysis of electron p_T spectra is 7.48×10^8 events with normal running conditions and an additional 5.79×10^7 events with additional converter material introduced. Section III J details the methodology for analyzing the converter data set. For the v_2 analysis, only those events with a good reaction plane calibration were used. The number of MB events used for the v_2 analysis was 7.1×10^8 events.

B. Data set and event selection ($p + p$)

The data for $p + p$ collisions at $\sqrt{s} = 200$ GeV were collected in the 2005 run of RHIC. Two data sets are used for the electron analysis: (1) the $p + p$ MB data set and (2) the electron triggered data set (PH). The MB trigger for $p + p$ required at least one hit in both the north and the south BBC detectors and the event vertex position within $|\text{bbc}z| < 30$ cm from the nominal collision point along the beam axis. The PH trigger required a minimum energy deposit of 1.4 GeV in any trigger tile of 4 × 4 EMCal towers in coincidence with the MB trigger. The PH trigger had nearly 100% trigger efficiency for electrons with p_T above 2 GeV/c in the active trigger tiles.

The MB trigger cross section is $\sigma_{\text{BBC}} = 23.0 \pm 2.2$ mb [40]. Because only $\simeq$50% of inelastic $p + p$ collisions satisfy the MB trigger condition, only a fraction of the inclusive electron production events were triggered by the PH trigger. This fraction is assumed to be momentum and process independent and is determined to be $\epsilon_{\text{bias}} = 0.79 \pm 0.02$ [41] from the yield ratio of high-$p_T\pi^0$'s with and without the BBC trigger. The value of ϵ_{bias} is slightly higher than that of 2002 (0.75) [42], owing to a lower BBC threshold.

After the selection of good runs and the vertex cut, an integrated luminosity ($\mathcal{L}$) of 45 nb^{-1} in the MB data set and 1.57 pb^{-1} in the PH data set are used for the analysis. During a part of the 2005 $p + p$ run, the same photon converter that was used in the 2004 Au + Au run was inserted around the beam pipe. The integrated luminosity in the converter run period is approximately 7% of the total luminosity.

C. Centrality (Au + Au)

The centrality of each Au + Au collision is determined by the measurements of BBC charge and ZDC energy. Figure 3 shows the correlation between BBC total charge and ZDC total energy, each of which is normalized by the respective maximum value. The measured BBC charge is sensitive to the charged-particle multiplicity in the pseudorapidity range $|\eta| = 3.0$–3.9 and is monotonically correlated to the number of participating nucleons from the two colliding nuclei. In contrast, the total ZDC energy has a nonmonotonic relation to the number of participating nucleons. In the most peripheral collisions, many of the spectator nucleons are bound in large nuclear fragments. The ZDCs only measure free spectator neutrons because charged nuclear fragments are swept away from the ZDC acceptance by the DX magnet of RHIC and thus the ZDC response is small. For midcentral collisions the total number of spectator nucleons is smaller, but a larger fraction of them are free neutrons as opposed to larger nuclear fragments, giving rise to a high ZDC response. Finally, for the most central collisions there are very few spectator nucleons and the ZDC response is again small. The centrality determination from the BBC charge and ZDC energy is schematically shown in Fig. 3.

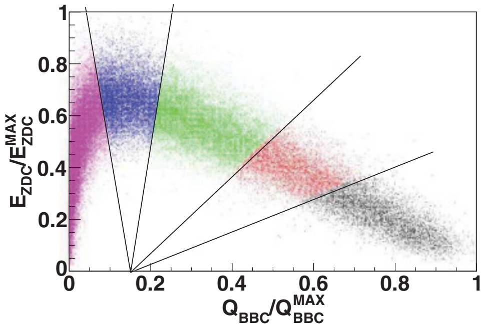

FIG. 3. (Color online) The correlation between fractional BBC charge Q/Q_{max} and fractional ZDC energy E/E_{max}. The selections from right to left correspond to centrality classes 0%–10%, 10%–20%, 20%–40%, 40%–60%, and 60%–92%.

The relation between centrality, the number of binary collisions (N_{coll}), and the number of participants (N_{part}) is obtained from a Glauber Monte Carlo simulation [43,44] combined with a simulation of the BBC and ZDC response. The systematic uncertainties in N_{coll} and N_{part} are calculated from the uncertainty in the Glauber parameters, the centrality determination, and BBC and ZDC responses. Table I summarizes the average N_{coll}, N_{part}, the associated nuclear overlap function (T_{AuAu}), and their systematic uncertainties for each centrality class.

D. Track reconstruction

Charged particles are reconstructed by the DC and PCs. Figure 4 shows an example charged-particle trajectory and the associated kinematic parameters. Assuming that the track originates on the beam axis, the intersections of the trajectory with each detector plane are uniquely determined by four initial kinematic parameters: z_{vtx}, θ, φ_{v}, and the transverse momentum p_T. Here z_{vtx} [denoted Z_{V} in Fig. 4(b)] is the interaction vertex along the z axis, θ is the angle between the initial direction of the particle track and the z axis, and φ_{v} is the initial azimuthal angle of the trajectory. These initial

TABLE I. N_{part}, N_{coll}, and T_{AA} with their systematic uncertainties [44] for Au + Au collisions at $\sqrt{s_{\text{NN}}} = 200$ GeV.

Centrality class	$\langle N_{\text{part}}\rangle$	$\langle N_{\text{coll}}\rangle$	$\langle T_{\text{AA}}\rangle(\text{mb}^{-1})$
0%–92%	109.1 ± 4.1	257.8 ± 25.4	6.14 ± 0.45
0%–10%	325.2 ± 3.3	955.4 ± 93.6	22.75 ± 1.56
10%–20%	234.6 ± 4.7	602.6 ± 59.3	14.35 ± 1.00
20%–40%	140.4 ± 4.9	296.8 ± 31.1	7.07 ± 0.58
40%–60%	59.95 ± 3.6	90.70 ± 11.8	2.15 ± 0.26
60%–92%	14.50 ± 2.5	14.50 ± 4.00	0.35 ± 0.10

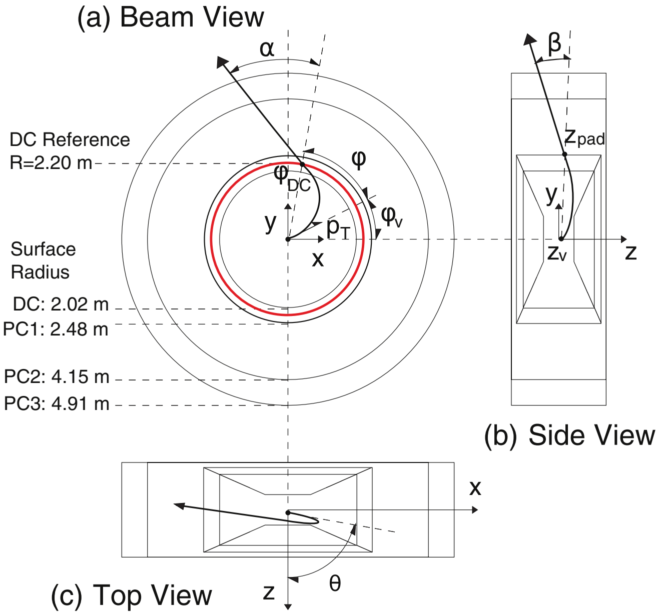

FIG. 4. (Color online) A charged particle trajectory and the kinematic parameters are shown in (a) beam view, (b) side view, and (c) top view of the PHENIX central region. In (b) the $Z_{\rm V}$ is the same as $z_{\rm vtx}$ in the text.

parameters are reconstructed from the measured variables: α, β, $z_{\rm pad}$, and $\varphi_{\rm DC}$. α is the angle between the projection of the trajectory in the x-y plane and the radial direction at the intersection point of the trajectory with the circle of DC reference radius ($R_{\rm DC} = 2.2m$). $z_{\rm pad}$ is the intersection point of the trajectory with the PC1 surface radius ($R_{\rm PC1} = 2.48$ m). β is obtained by considering the plane which includes the z axis and $z_{\rm pad}$. It is defined as the angle between the projection of the trajectory to the plane and the line connecting the vertex to the position of the PC hit. $\varphi_{\rm DC}$ is the azimuthal angle of intersection point of the trajectory with the circle of radius with $R_{\rm DC}$.

The tracking process starts by collecting hits in DC X1 and X2 wires. The hits are projected to the x-y plane at $z = 0$. Then, a Hough transform is applied to find the sets of hit points based on the assumption that the track has a straight line trajectory inside the DC volume [45,46]. The technique is performed using all possible X1 and X2 hit combinations taking α and $\varphi_{\rm DC}$ as the parameters in Hough space. After this process, the direction of the found track line is specified by α and $\varphi_{\rm DC}$. The hits in the U and V wires and PC1 hits are associated with the track to obtain $z_{\rm pad}$ and β. After the pattern recognition and track reconstruction, the initial momentum vector of the track at the collision vertex is calculated. A look-up-table technique is used for fast processing [47,48]. After the initial kinematic parameters are obtained, each reconstructed track is associated with hit information from the outer detectors (PC2, PC3, RICH, and EMCal).

E. Electron identification

Electron candidates are selected from reconstructed charged particle tracks based on information from the RICH and EMCal. For each of the reconstructed tracks, the following variables are calculated and used for electron identification (eID).

quality Tracks are required to have hits in both the X1 and the X2 sections of the DC and be uniquely associated with hits in the U or V stereo wires. At least one matching PC1 hit is also required.

emcsdphi_e Displacement in ϕ of the electron hit position of the associated EMCal cluster from the projected position of the track in units of standard deviations. For example, **emcsdphi_e** < 2 means that the position of the associated EMCal cluster in ϕ is within 2σ of the projected track position. This variable was calibrated specifically for electrons.

emcsdz_e Same as **emcsdphi_e**, but for the z coordinate.

prob The probability that the associated EMCal cluster is an electromagnetic shower. This variable is calculated from the χ^2 value between the actual tower energy distribution of the cluster and the expected distribution for an electromagnetic shower. For example, a cut, **prob** > 0.01, has 99% efficiency for a photon or electron shower, while it rejects a large fraction of hadrons.

n0 Number of hit RICH PMTs in an annular region with an inner radius of 3.4 cm and an outer radius of 8.4 cm around the track projection on the RICH. The expected radius of a Čerenkov ring emitted by an electron is 5.9 cm.

n1 The number of hit RICH PMTs within 11 cm around the projection point of the track.

chi2/npe0 A χ^2-like shape variable of the RICH ring associated with the track.

disp A variable representing the displacement of the RICH ring center from the projected track position. Units are cm.

dep A variable of energy momentum matching. This variable is calculated as **dep** $= (E/p - 1)/\sigma_{E/p}$, where E is the energy measured by EMCal, p is the momentum of the track, and $\sigma_{E/p}$ is the standard deviation of a Gaussian-like E/p distribution. E/p is less than 1 for hadrons because hadrons do not deposit their full energy in the calorimeter. $\sigma_{E/p}$ depends on the momentum of the electron.

Tables II and III summarize the eID cuts used for the Au + Au and $p + p$ analyses, respectively. For tracks with p_T below 4.8 GeV$/c$, the RICH is fired only by electrons. Thus, the RICH is the primary means of electron detection in this p_T region. The E/p cuts help remove any remaining background. The main cause of electron misidentification below 5 GeV$/c$ is that a charged hadron track is accidentally associated with hits in the RICH detector. Because the particle multiplicity in $p + p$ is very small, typically a few tracks in each of the central arm spectrometers, the probability of such an accidental overlap is much smaller. This permits us to use looser electron cuts in the $p + p$ analysis. Note that although hadrons could fire the RICH above 4.8 GeV$/c$, the number of photoelectrons is small for hadrons below 5 GeV$/c$, and such hadrons are easily distinguishable from electrons.

In $p + p$ collisions the hadron contamination after the eID cuts is very small. The contamination level is estimated by reversing the **prob** cuts to enhance the hadron background.

TABLE II. Electron ID cuts used in the Au + Au analysis.

eID cuts for Au + Au
$\sqrt{\text{emcsdphi\_e}^2 + \text{emcsdz\_e}^2} < 2.0$
n0 $\geqslant 2$
n1 $\geqslant 3$ if $p_T < 5.0$ GeV/c
n1 $\geqslant 5$ if $p_T > 5.0$ GeV/c
disp < 5.0
chi2/npe0 < 10.0
prob > 0.01 if $p_T < 5.0$ GeV/c
prob > 0.2 if $p_T > 5.0$ GeV/c
dep > -2.0

The estimated hadron contamination is 3% at $p_T = 0.3$ GeV/c and less than 1% for $0.8 < p_T < 5$ GeV/c while maintaining an eID efficiency ∼90%. In Au + Au collisions, a significant hadron background remains owing to accidental overlap between hadron tracks and RICH hits. This background is estimated and subtracted as described below.

Figures 5(a) and 5(b) show E/p distributions for two typical p_T ranges in Au + Au collisions. All cuts in Table II are applied except for the **dep** cut because it is just a p_T-dependent cut in E/p. The data points shown with square symbols are the estimated distributions of the remaining hadron background which are randomly associated with a ring in the RICH. This estimation is performed by swapping the north and south sides of the RICH in the same event in software and reconstructing the track matching to the RICH. That is, DC tracks from the south are matched with RICH hits in the north and vice versa. Because the north and the south sides of the RICH are identical and there was only ∼1% of dead channels in the RICH PMTs, this method gives a proper statistical estimate of the random hadron background in the electron sample.

After subtraction of the random hadron associations, an additional low E/p tail remains in the distribution at high p_T, as shown in Fig. 5(b). This tail is attributable to electrons from kaon decay ($K \to e\pi\nu$, referred to as K_{e3}) and photon conversions that occur far from the collision vertex. These background electrons are reconstructed with a momentum higher than the actual momentum of the electrons and, as such, have a low E/p.

TABLE III. Electron ID cuts used in the $p + p$ analysis.

eID cuts for $p + p$
|emcsdphi_e| < 4
|emcsdz_e| < 4
n0 $\geqslant 2$
n1 $\geqslant 2$
prob > 0.01
$0.50 < E/p < 1.3 (0.2 < p < 0.3$ GeV/$c)$
$0.55 < E/p < 1.3 (0.3 < p < 0.4$ GeV/$c)$
$0.60 < E/p < 1.3 (0.4 < p < 0.6$ GeV/$c)$
$0.65 < E/p < 1.3 (0.6 < p < 0.8$ GeV/$c)$
$0.70 < E/p < 1.3 (0.8 < p < 5.0$ GeV/$c)$

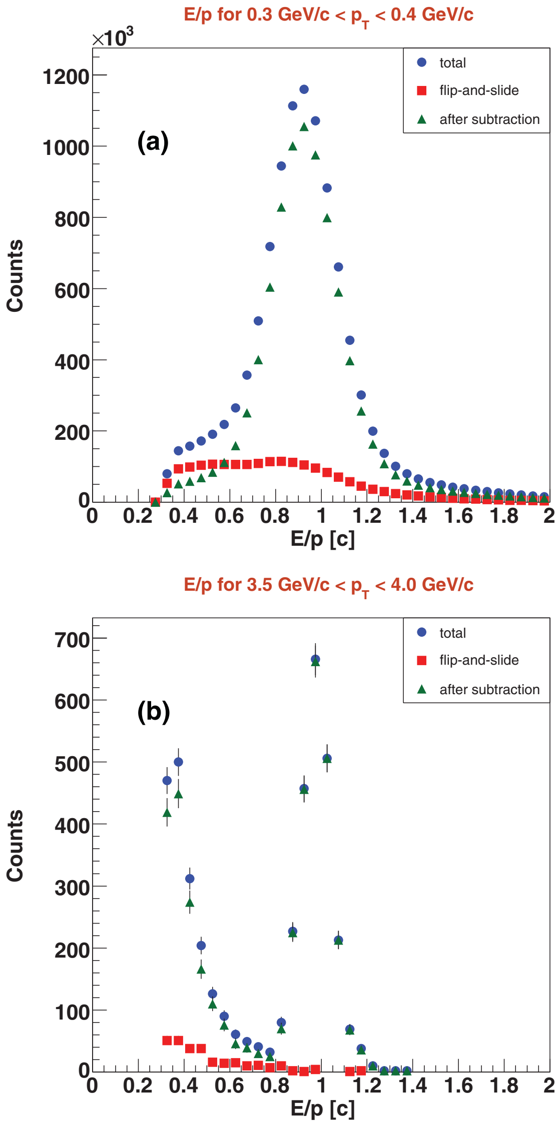

FIG. 5. (Color online) E/p distributions for (a) $0.3 < p_T < 0.4$ GeV/c and (b) $3.5 < p_T < 4.0$ GeV/c in Au + Au collisions. See text for more details.

To quantify these remaining background sources, we have carried out detailed simulations of these channels. For $p + p$ collisions, we use $d\sigma/dy(pp \to \pi^0) = 46.0$ mb and $d\sigma/dy(pp \to K^L) = d\sigma/dy(pp \to K^\pm) = 4.0$ mb at midrapidity. The momentum distribution of π^0 and kaons are based on PHENIX measurements in $p + p$. Then a full GEANT [49] simulation of the PHENIX detector was performed. Figure 6 shows the E/p distribution in $p + p$ for $0.8 < p_T < 1.0$ GeV/c compared with the GEANT simulation. The black stars are the data points and the circles show the simulation. The triangles and squares show the contributions from simulation of π^0 and K_{e3}, respectively. The simulated π^0 and K_{e3} decays went through the same offline analysis chain as in the real data, and identical eID cuts were applied. In the $p + p$ data, the contamination owing to hadron misidentification is negligible. In the π^0 simulation, electrons are mainly produced either by the Dalitz decay or by photon conversion in the beam

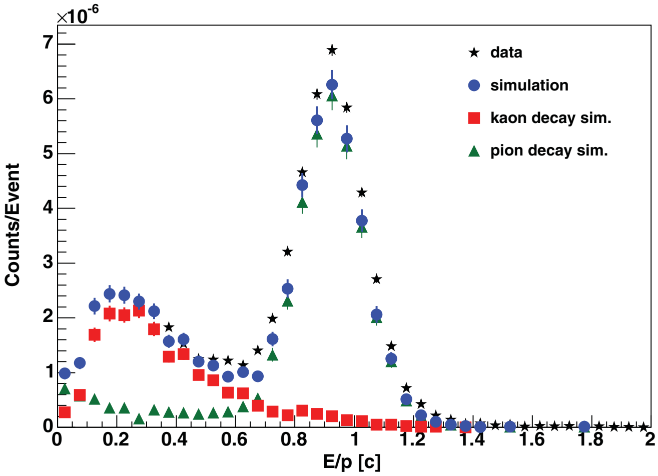

FIG. 6. (Color online) E/p distributions in $p + p$ collisions for $0.8 < p_T < 1.0$ GeV/c compared with the GEANT simulation. The black stars are the data points and the solid circles show the GEANT [49] simulation. The triangles and squares show the contributions from simulation of π^0 and K_{e3}, respectively. See text for more details.

pipe. These electrons produce the peak around $E/p = 1$. Note that in Fig. 6 the data is above the simulation because the data also contain nonphotonic electrons. A small number of conversions in the helium bag contribute to the tail in the low E/p region. The main cause of the low E/p tail is K_{e3} decay, shown as squares. Because the simulation reproduces the low E/p tail of the data very well, we conclude that the small K_{e3} background under the Gaussian peak, which will remain after the **dep** or E/p cuts, can be determined from the simulation.

For p_T above 4.8 GeV/c, charged pions begin to radiate Čherenkov light in the RICH. Thus, tighter electron selection cuts are applied to reject pion background. In both the Au + Au and $p + p$ analyses, tighter cuts of **n1** $\geqslant 5$ and **prob** > 0.2 are added. In the $p + p$ analysis, the E/p cut is tightened to $0.8 < E/p < 1.3$. With these cuts, the electron measurement is extended to 9 GeV/c in p_T.

The remaining hadronic background with the tighter cuts is studied using the shape of the E/p distribution. Here we rely on the fact that the distribution of the **prob** and E/p variables are roughly independent of p_T for hadrons at high p_T and that a cut on **prob** < 0.01 eliminates the vast majority of electrons. First, we obtain a sample of hadrons in the p_T range of 1–4 GeV/c by imposing a veto on the RICH. The hadron sample is then divided into two samples, one with **prob** > 0.01 and the other with **prob** < 0.01. The ratio of these two hadron samples is taken. The E/p distributions for p_T above 5 GeV/c are then estimated from the data with cuts identical to those described above, except with the **prob** cut reversed to **prob** < 0.01. These E/p distributions are then divided by the ratio of the hadron samples defined above to obtain an estimate of the E/p distributions of hadrons passing the **prob** > 0.01 cut. Between 8 and 9 GeV/c in p_T, we estimate a background of 20%, with an uncertainty of 10%. The eID efficiency of the tighter cuts is p_T independent. In $p + p$, it is determined to be 57% of that for $p_T < 5$ GeV/c by applying the same tighter cuts for $p_T < 5$ GeV/c.

F. Acceptance correction

The single electron acceptance correction in this analysis covers the following three components: the geometrical acceptance correction ($\epsilon^{\rm geo}$), the eID efficiency ($\epsilon^{\rm eID}$), and the reconstruction efficiency ($\epsilon^{\rm reco}$). $\epsilon^{\rm geo}$ accounts for the fraction of electrons that do not hit any detectors owing to the finite solid angle covered by the detectors. $\epsilon^{\rm eID}$ is the correction factor for signal loss by eID cuts. $\epsilon^{\rm reco}$ takes into account that the measured electron spectrum in the detector is different from the real spectrum owing to detector responses and the track reconstruction method. All the values are computed at once by the full detector simulation for single $e^{\pm}$ events. Single e^+ and e^- events are generated uniformly in phase space ($0 < p_T^e < 15$ GeV/c, $|y| < 0.5$, and $0 < \phi < 2\pi$). They are processed by the full GEANT simulation program of the PHENIX detector [49]. The output simulation data files are processed by the event reconstruction chain of PHENIX. The acceptance correction factor ($\epsilon_{\Delta y}^{\rm acc}$) is calculated as follows:

$$\epsilon_{\Delta y}^{\rm acc} \equiv \epsilon^{\rm geo} \cdot \epsilon^{\rm reco} \cdot \epsilon^{\rm eID} = \frac{dN_e^{\rm out}/dp_T^e}{dN_e^{\rm in}/dp_T^e}. \tag{2}$$

The p_T^e distributions of input and output electron yields are $dN_e^{\rm in}/dp_T^e$ and $dN_e^{\rm out}/dp_T^e$, respectively. The same eID cuts and fiducial cuts used in real data processing are applied to the output. Because the input electrons are generated flat in p_T^e, we must take into account that the smearing of the spectrum owing to imperfect momentum reconstruction affects a steeply falling spectrum differently than our simulated spectra. Each track reconstructed in the simulation is weighted properly as a function of the p_T^e of the corresponding input electron. Figure 7 shows $\epsilon_{\Delta y}^{\rm acc}$ for Au + Au as a function of p_T with eID cuts applied for $0.3 < p_T < 5.0$ GeV/c, $5.0 < p_T < 7.0$ GeV/c, and $7.0 < p_T < 9.0$ GeV/c, respectively. For the 2005 $p + p$ analysis, $\epsilon_{\Delta y}^{\rm acc}$ is approximately twice as large because much looser eID cuts are used and the active detector area was larger.

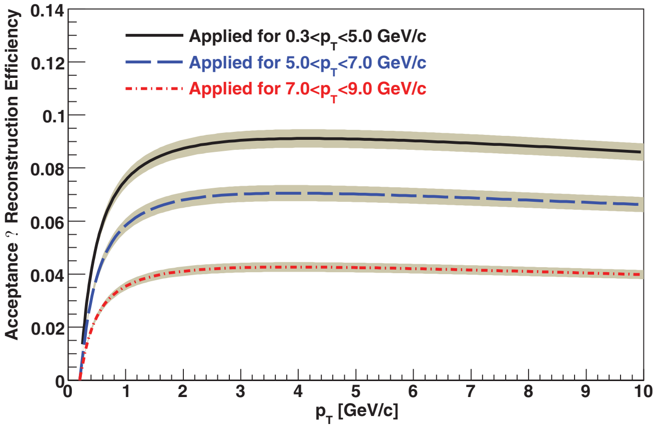

FIG. 7. (Color online) $\epsilon_{\Delta y}^{\rm acc}$ for $(N_{e^+} + N_{e^-})/2$ as a function of p_T in Au + Au. The top, middle, and bottom curves are calculated with eID cuts applied for $0.3 < p_T < 5.0, 5.0 < p_T < 7.0$, and $7.0 < p_T < 9.0$ GeV/c, respectively. The bands span the systematic error assigned for each correction.

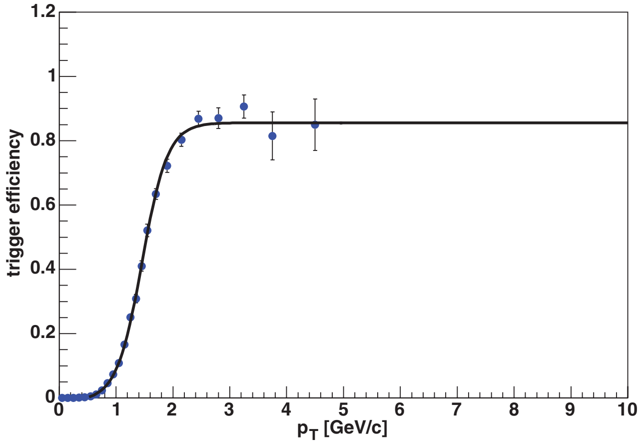

FIG. 8. (Color online) Efficiency of the PH trigger in $p + p$ determined from the MB data set.

G. Trigger efficiency ($p + p$)

The PH trigger efficiency in $p + p$ collisions is determined from the MB data set as the fraction of electrons that satisfies the PH trigger. Because the trigger condition determined by the online level-1 trigger processor was recorded, we can apply the same PH trigger to the events recorded in the MB trigger in the offline analysis. We require that the PH trigger bits of the event are set and that the trigger tile that fires the PH trigger is hit by the electron candidate track selected by the offline analysis.

Figure 8 shows the PH trigger efficiency versus p_T. The effective trigger threshold is about 1.4 GeV, and the efficiency saturates above 2 GeV. The trigger efficiency at the plateau is ≈86%, consistent with the fraction of active trigger tiles. The curve is a Fermi-like function that is fitted to the data. The fitted function is used as the trigger efficiency in the analysis.

H. Occupancy correction (Au + Au)

In addition to the efficiency to reconstruct and identify a single electron passing through the detector, there is also an efficiency loss owing to the presence of a high number of other particles in the detector. To get a quantitative understanding of the multiplicity-dependent efficiency loss, we embed simulated single electrons into data files containing detector hits from real collisions. The same simulated particles are used in this method as those used to estimate the single-particle efficiency. The simulated particles are embedded into events such that the z vertex of the simulated particle and the event match. The simulated $e^{\pm}$ are run through the GEANT simulation of PHENIX, and the hits are added to the data files containing hits from a real Au + Au event. Next, these new files containing the embedded $e^{\pm}$ are run through the entire reconstruction software to produce track candidates containing the variables upon which we make identification cuts. We then define the embedding efficiency as

$$\epsilon_{\text{embed}} = \frac{\text{No. reconstructed } e^{\pm} \text{ from embedded data}}{\text{No. reconstructed } e^{\pm} \text{ from single-track data}}, \tag{3}$$

where a reconstructed particle from embedded data has most of its detector hits associated with hits from the simulated particle.

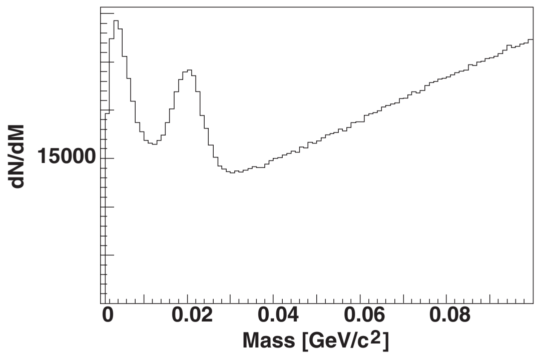

FIG. 9. Invariant mass distribution of $e^{\pm}$ pairs from MB Au + Au data with the minimum eID cuts used for the multiplicity-dependent efficiency loss estimate.

As a cross-check on this embedding method, a data-driven method was also employed. The general strategy of this data-driven method is to prepare a very pure sample of electrons by selecting electron pairs from two known sources, $e^{\pm}$ pairs from photon-conversions in the beam pipe and from π^0 Dalitz decays. We then assume that the multiplicity-dependent efficiency loss for these electrons is the same as for all electrons. Because for the momentum measurement in PHENIX it is assumed that tracks originate from the collision vertex, tracks that originate off vertex are reconstructed with an incorrect momentum. This leads to the reconstruction of conversion pairs with an apparent invariant mass $M_{ee} > 0$. Figure 9 shows the invariant mass distribution of $e^{\pm}$ pairs from the data with the minimum eID cuts. The peak at ∼20 MeV/c^2 corresponds to the reconstructed invariant mass of electrons from photon conversions in the beam pipe. The peak at ∼5 MeV/c^2 corresponds to $e^{\pm}$ from π^0 Dalitz decays. The combinatorial background, which rises linearly with mass, is subtracted by an event-mixing technique. The number of electron pairs below $M_{ee} < 30$ MeV/c^2, after combinatorial background subtraction, is used to determine the eID efficiency.

To have a clean sample of $e^{\pm}$ pairs, we apply tighter eID cuts to one of the tracks in the pair. We restrict ourselves to pairs with one track in the acceptance of the time of flight (TOF) detector [34] so that we can use the TOF for additional eID. Then, for the other track, as a function of collision centrality we measure the efficiency loss of the cuts actually used in the standard analysis (for $p_T < 5$ GeV/c) relative to that of a set of much looser cuts. At the end, we still need to simulate the multiplicity-dependent loss owing to the looser eID cuts, but simulation is more reliable when looser cuts are used.

As described in the previous section, for $p_T > 5$ GeV/c we obtain the efficiency by the relative electron yield between the samples with the cuts used for the two p_T ranges. This relative yield includes multiplicity-dependent effects, so we only explicitly calculate the multiplicity-dependent efficiency loss for the cuts used for $p_T < 5$ GeV/c. Some of the relative efficiency loss using the method just described is attributable

TABLE IV. Multiplicity-dependent efficiency loss calculated by two methods. $\epsilon^{\mathrm{embed},C}$ is the efficiency loss calculated from the embedding simulation. $\epsilon^{\mathrm{embed},C}_{\mathrm{loose}}$ is the same as above but with the loose cuts.

Centrality	$\epsilon^{\mathrm{embed},C}$	$\epsilon^{\mathrm{data},C}_{\mathrm{mult}} \times \epsilon^{\mathrm{embed},C}_{\mathrm{loose}}$
0%–92%	0.852	0.882
0%–10%	0.771	0.769
10%–20%	0.835	0.856
20%–40%	0.900	0.924
40%–60%	0.952	0.977
60%–92%	0.982	0.997

to the single-particle efficiency. To obtain an estimate of the multiplicity-dependent component of this relative loss, we divide the relative loss by the loss for peripheral collisions (60%–92% centrality), because the multiplicity-dependent loss in peripheral collisions is very low. So we have defined the multiplicity-dependent efficiency loss from the data-driven method for centrality C as

$$\epsilon^{\mathrm{data},C}_{\mathrm{mult}} = \frac{\epsilon^{\mathrm{data},C}_{\mathrm{eID}}}{\epsilon^{\mathrm{data},60-92\%}_{\mathrm{eID}}}, \tag{4}$$

with

$$\epsilon^{\mathrm{data},C}_{\mathrm{eID}} = \frac{\epsilon^{C}_{\mathrm{tight\ cuts}}}{\epsilon^{C}_{\mathrm{loose\ cuts}}}. \tag{5}$$

Finally, we correct the multiplicity-dependent efficiency loss by using the efficiency from the embedding simulation for the loose cuts, $\epsilon^{\mathrm{embed},C}_{\mathrm{loose}}$, to obtain the more accurate estimate of the multiplicity-dependent loss from the otherwise data-driven method.

Table IV displays the two embedding efficiencies described above. The difference between the left and right columns gives an idea of the systematic uncertainty involved in this estimation. The use of the sample of conversion and Dalitz $e^{\pm}$ pairs are discussed further in the section pertaining to the systematic uncertainty analysis.

I. Electron background cocktail

The inclusive electron spectra consist primarily of four components:

(i) heavy-flavor electrons (nonphotonic electrons from heavy-flavor decays),
(ii) photonic background from Dalitz decays of light neutral mesons and photon conversions (mainly in the beam pipe),
(iii) nonphotonic background from $K \rightarrow e\pi\nu$ (K_{e3}) and dielectron decays of light vector mesons, and
(iv) heavy quarkonia (J/ψ, Υ) and Drell-Yan background processes.

Of the three background sources, the "photonic" background is the largest. At high electron p_T, Drell-Yan processes also account for a small but non-negligible contribution to the electron spectrum. Also, heavy-quarkonia decays contribute at high electron p_T, which, although arguably can be included in electrons from "heavy-flavor" decays, should be distinguished from open heavy-flavor decays for the purpose of interpreting the measurement.

The signal of electrons from heavy-flavor D and B meson decays is small compared to the photonic background at low p_T ($S/B < 0.2$ for $p_T < 0.5$ GeV/c) but rises with increasing p_T ($S/B > 1$ for $p_T > 2$ GeV/c). To extract the heavy-flavor signal, the various background contributions have to be subtracted from the inclusive electron spectra. One technique to accomplish this task is the so-called "cocktail subtraction" method described in detail here. The second method, the so-called "converter subtraction method" is described in Sec. III J.

A cocktail of electron spectra from background sources is calculated using a Monte Carlo event generator of hadron decays and then subtracted from the inclusive electron spectra. This technique requires that the total yield and momentum distributions of the relevant background sources are well known. The PHENIX measurements of the relevant electron sources are precise enough to constrain the background within a systematic uncertainty better than 15% for all p_T.

The most important background source, except for the highest electron p_T where contributions from direct photons become dominant (see below), comes from the neutral pion. The contribution of π^0 decays to the photonic background is twofold. First, the Dalitz decay of neutral pions ($\pi^0 \rightarrow e^+e^-\gamma$) is a primary source of electrons from the collision vertex. Second, the conversion of photons from the decay $\pi^0 \rightarrow \gamma\gamma$ in material in the PHENIX central arm aperture (mainly in the beam pipe) gives rise to a secondary source of electrons originating away from the original collision vertex. It is crucial to note that the contribution from photon conversions is smaller than the contribution from Dalitz decays. This is attributable to the carefully minimized material budget in the PHENIX central arms. Apart from the beam pipe, which is made out of beryllium and contributes less than 0.3% of a radiation length to the material budget, helium bags constitute the only material between the beam pipe and the tracking and eID detectors in PHENIX. As was verified in a full GEANT simulation of π^0 decays, the ratio of electrons from the conversion of photons from $\pi^0 \rightarrow \gamma\gamma$ decays to electrons from π^0 Dalitz decays is 0.403 with a systematic uncertainty of about 10%. This ratio is independent of p_T for $p_T > 1$ GeV/c. For heavier mesons (η, η', etc.) this ratio is rescaled in the cocktail to properly account for the fact that the branching ratio for the Dalitz decay relative to the $\gamma\gamma$ decay grows slightly with increasing parent meson mass. Consequently, once the momentum distributions of π^0 and heavier mesons are available, one can determine both the Dalitz decay contribution to the background electron spectrum as well as the corresponding contribution from the conversion of photons from the same parent mesons.

The momentum distributions of π^0 are obtained via simultaneous fits to the charged and neutral pion spectra. This approach is only valid under the assumption that the invariant π^0 spectra and the averaged charged pion spectra $(\pi^+ + \pi^-)/2$ are the same. While this assumption in general is well justified, for $p_T < 1$ GeV/c, the decay of η mesons into three π^0's creates a tiny charge asymmetry. However,

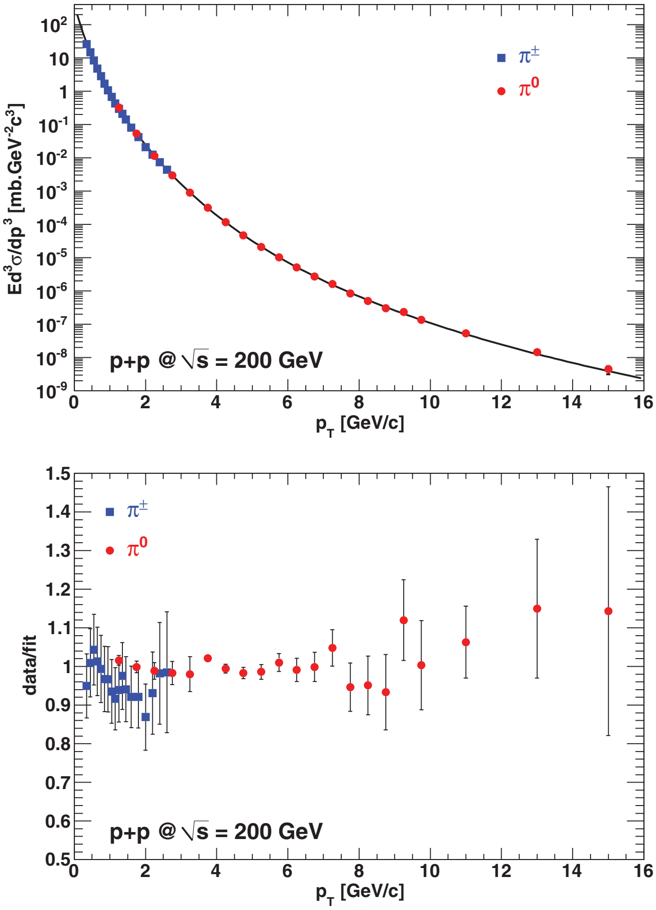

FIG. 10. (Color online) (Top) Invariant differential cross section of charged pions (blue squares) [50] and neutral pions (red circles) [51] for $p + p$ collisions at $\sqrt{s} = 200$ GeV, together with a fit to Eq. (6). The uncertainties shown are the quadrature sum of the statistical and systematic uncertainties. (Bottom) Ratio of the data to the fit.

according to a PYTHIA [52] calculation and consistent with data, this asymmetry is only about 2% and can be safely ignored in this context.

Figure 10 shows the comparison of the neutral [51] and charge-averaged [50] invariant differential cross sections of pions in $p + p$ collisions at $\sqrt{s} = 200$ GeV in comparison with a simultaneous fit to the data with a modified Hagedorn parametrization:

$$E\frac{d^3\sigma}{d^3p} = \frac{c}{[\exp(-ap_T - bp_T^2) + p_T/p_0]^n}, \qquad (6)$$

where a, b, c, p_0, and n are fit parameters. Both an absolute comparison as well as the ratio of the data to the fit are shown to demonstrate the good quality of the parametrization.

For Au + Au collisions the π^0 invariant differential multiplicity distributions are obtained by equivalent fits to the measured π^0 [6,53] and $\pi^{\pm}$ [54] spectra independently for various centrality selections. Figure 11 shows the comparison of data and parametrization on absolute and relative scales for MB Au + Au collisions as an example.

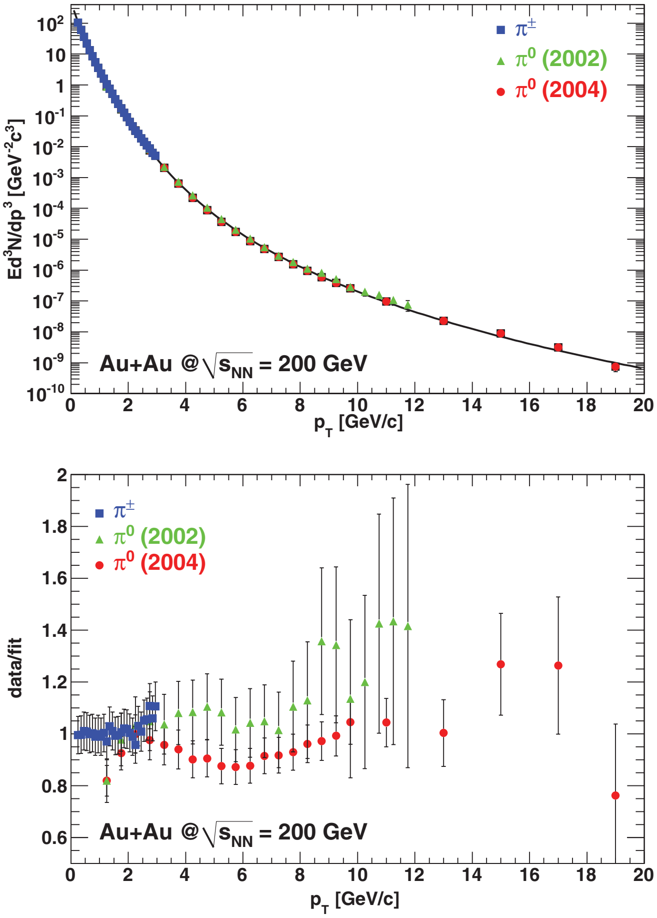

FIG. 11. (Color online) (Top) Invariant multiplicity of charged pions (blue squares) and neutral pions for minimum bias Au + Au collisions from 2002 (green triangles) and 2004 (red circles) together with a fit according to Eq. (6). The uncertainties shown are the quadrature sum of the statistical and systematic uncertainties. (Bottom) Ratio of the data to the fit to the 2004 data. There is also a point-to-point correlated systematic uncertainty of 7% which is not shown in the figure.

The neutral pion spectrum from 2004 is systematically different from the 2002 result. The difference between the parametrization and both sets of neutral pion spectra gives rise to an additional systematic uncertainty in the resulting electron cocktail. The difference between the parametrizations is assumed to be 1 standard deviation owing to this systematic difference. This systematic uncertainty reaches its maximum value for electrons in the p_T range between 3 and 5 GeV/c and is significantly less for lower as well as higher p_T. Figure 12 includes this systematic uncertainty as a function p_T.

Given that pion decays are the most important cocktail ingredient at low and intermediate p_T, it is obvious that the cocktail systematic uncertainty is largely dominated by the uncertainty in the pion spectra as well. To evaluate this uncertainty the full cocktail calculation is repeated with the pion cross section moved up and down by 1 standard deviation in the systematic uncertainty, propagating the uncertainty in the pion spectra to the electron cocktail. With a systematic uncertainty of ~10%, almost independent of p_T, some of

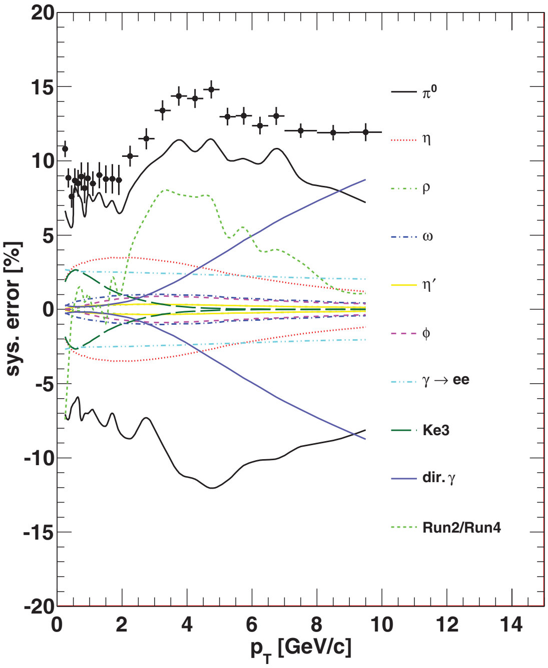

FIG. 12. (Color online) Systematic error assigned to each cocktail ingredient for MB Au + Au collisions. The points show the total systematic error for each p_T.

TABLE V. Ratios of mesons to neutral pions at $p_T = 5$ GeV/c in $p + p$ collisions at $\sqrt{s} = 200$ GeV.

Meson-to-pion ratios
$\eta/\pi^0 = 0.48 \pm 0.03$ [55]
$\rho/\pi^0 = 1.00 \pm 0.30$ [58]
$\omega/\pi^0 = 0.90 \pm 0.06$ [59]
$\eta'/\pi^0 = 0.25\ \pm 0.075$ [58]
$\phi/\pi^0 = 0.40 \pm 0.12$ [58]

which originates from the difference between the Run 2 and Run 4 π^0 measurements, the pion input represents the largest contributor to the electron cocktail uncertainty.

Other light mesons contributing to the electron cocktail are the η, ρ, ω, η', and ϕ mesons via their Dalitz and/or dielectron decays as well as via the conversion of photons from their decays. However, only the η meson is of any practical importance here.

For the cocktail calculation, the shape of the invariant p_T distributions and the relative normalizations to the π^0 are required as input parameters. The p_T spectra are derived from the pion spectrum by m_T scaling; that is, the same modified Hagedorn parametrizations are used [Eq. (6)], but with p_T replaced with $\sqrt{{p_T}^2 + m^2_{\text{meson}} - m^2_{\pi^0}}$. The resulting η/π^0 ratios agree with corresponding PHENIX data for $p + p$ and Au + Au collisions [55–57].

Because the chosen approach of m_T scaling ensures that at high p_T the spectral shapes of all meson distributions are the same, the normalization of the meson spectra relative to the pion spectrum can be given by the ratios of mesons to pions at high p_T (5 GeV/c is used here). The values used for $p + p$ collisions are shown in Table V.

For Au + Au collisions the same central values are used, but the uncertainties of the ratio η/π^0 and ω/π^0 are, conservatively, increased to 0.10 and 0.27, respectively, because precision measurements are not available in Au + Au collisions at all centralities.

The contribution from the K_{e3} decay and the semileptonic decay of K^0_S can only be determined via a full GEANT simulation, taking into account the exact eID cuts. The electron cocktail includes parametrizations based on such GEANT simulations using the charged kaon spectra measured in $p + p$ and Au + Au collisions as input [54]. Systematic uncertainties are fully propagated from the kaon spectra to the spectra of reconstructed electrons from K_{e3} decays. The contribution from kaon decays is only relevant (i.e., larger than 10%) for electrons with $p_T < 1$ GeV/c.

Contributions to the electron cocktail from direct photons are twofold. First, real photons produced in initial hard scattering processes, that is, so-called direct photons, convert in material in the PHENIX aperture exactly as photons from light neutral meson decays. Second, every source of real photons also presents a source of virtual photons. Consequently, direct real photon production is accompanied by direct virtual photon production, that is, the emission of e^+e^- pairs. In the case of the neutral pion these two sources are the $\gamma\gamma$ decay of the π^0 and the corresponding Dalitz decays, which are also called internal conversions. The measured real direct photon spectra are parametrized and the conversion electron spectra of these are added to the electron cocktail.

Figure 13 shows comparisons of the measured direct photon spectrum with the cocktail parametrization for (upper) $p + p$ [60] and (lower) MB Au + Au collisions [61]. In accordance with direct photon measurements in Au + Au collisions, the direct photon yield is assumed to scale with the number of binary collisions as a function of the centrality in the Au + Au electron cocktail.

PHENIX observed enhanced production of direct photons relative to the binary scaling for $p_T < 3$ GeV/c in Au + Au collisions [62,63]. The cocktail calculation does not take into account this enhancement and therefore the parameterization used in the cocktail underestimate the direct photon contribution below 3 GeV/c. However, the contribution of direct photon in this p_T range is small, $\simeq$15% in Au + Au and much smaller in $p + p$. In addition, in the low-p_T region where we observe enhanced direct photon production, we use the converter method, which is not affected by the enhanced direct photon yield. See Sec. III J for details.

The ratio of virtual direct photons to real direct photons depends on p_T because the phase space for dielectron emission increases with increasing p_T [63]. The same effect is seen in the Dalitz decays of light neutral mesons. For instance, the Dalitz decay branching ratio relative to the two-photon decay branching ratio is larger for the η meson than for the π^0. Consequently, the ratio of virtual to real direct photon emission increases with p_T.

Figure 14 shows the resulting electron cocktails for $p + p$ and Au + Au collisions at 200 GeV. Systematic uncertainties are estimated for all cocktail ingredients, propagated to the

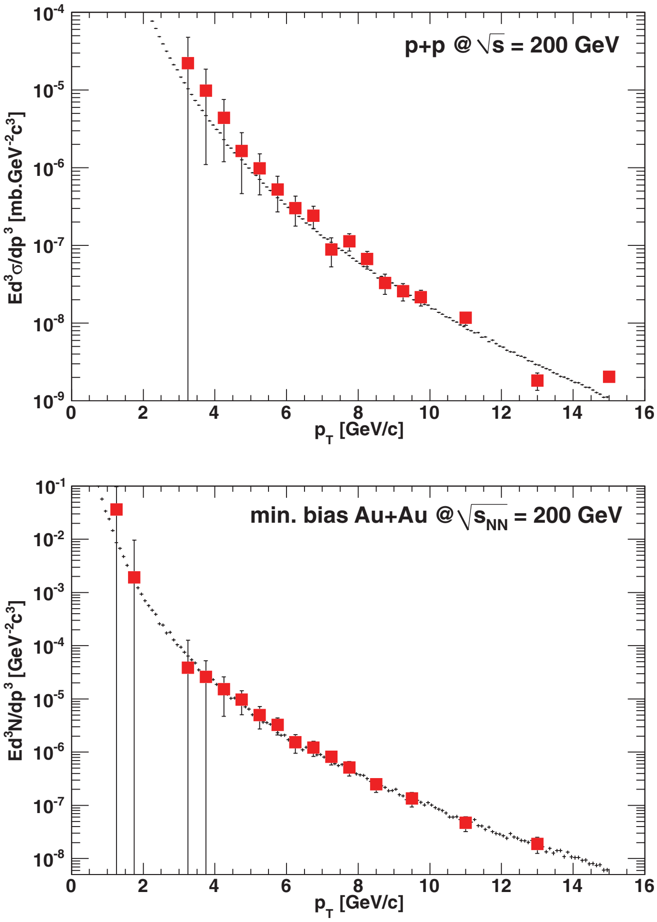

FIG. 13. (Color online) Measured direct photon spectrum (red squares) compared with the cocktail parametrization (histogram) for (upper) $p + p$ and (lower) MB Au + Au collisions. The uncertainties shown are the quadrature sum of the statistical and systematic uncertainties. There is also a point-to-point correlated systematic uncertainty of 7% which is not shown in the figure.

corresponding electron spectra, and then added in quadrature to determine the total cocktail systematic uncertainty as shown in Fig. 12 for MB Au + Au collisions. The following systematic uncertainties are assigned to the various inputs.

(i) Pion spectra. Obtained via full cocktail calculations using pion spectra moved up (down) by the systematic uncertainty of the pion spectra as input (almost no p_T dependence). This is the dominant systematic uncertainty for $p_T < 5$ GeV/c.

(ii) Meson-to-pion ratios. The systematic uncertainties are listed in Table V. Because the contributions from all other mesons are much smaller than the contribution from η decay only the η meson is of any practical relevance.

(iii) Conversion material in the aperture. The contribution from photon conversions depends on the material present in the aperture. A careful analysis of fully reconstructed dielectrons from photon conversions results in an uncertainty of less than 10%.

(iv) K_{e3} decay. This contribution is estimated via a full GEANT simulation. This is a relatively small contribution, though owing to simulation statistics a 50% systematic uncertainty is assigned.

(v) Direct photon. This contribution is directly propagated from the systematic uncertainty quoted for the direct photon measurement. It is relevant only at high p_T in central Au + Au collisions.

In previous analyses, the single-electron background cocktail has not included contributions originating from quarkonia decay (J/ψ and Υ) or Drell-Yan processes. Each of these processes has a small total cross section relative to the electron cocktail background. However, with increasing p_T these processes begin to contribute significantly and are included in the cocktail here.

PHENIX has measured the J/ψ p_T spectrum from 0 to 9 GeV/c in $p + p$ collisions [64,65]. The STAR experiment has measured the J/ψ p_T spectrum from 5 to 13 GeV/c [66]. Although the experimental uncertainties are non-negligible, the two measurements appear to disagree where they overlap in p_T, with the STAR results giving a smaller yield [65]. For consistency and cancellation of systematic uncertainties, we have chosen to parametrize only the PHENIX result in this analysis. As we show below, this J/ψ contribution to the background electrons is significant for $p_T > 5$ GeV/c. However, the signal to background is much greater than one in this p_T range and so the impact on the final heavy-flavor electron distribution is only ∼10%. Utilizing the STAR data would make this correction even smaller.

Two functional fits to the PHENIX J/ψ data are performed. The first uses the so-called Kaplan function $p_0\left[1 + (p_T/p_1)^2\right]^{-n}$, and the second assumes the m_T scaling function used in Ref. [67]. Because both functions may provide valid representations of the true J/ψ spectral shape, the average of these two functional fits to the data determines the central values used in the cocktail. The upper (lower) systematic uncertainties of the spectral shape are determined by normalizing each of the functional forms up (down) by 10% and using the largest (smallest) result for the systematic uncertainty. In practice, the lower bound of the spectral shape is determined by the smaller Kaplan function normalized down a further 10%, while the upper bound is set by the larger m_T scaling function normalized up 10%.

The Υ p_T spectra have not been measured at RHIC. Because the overall production cross section for Υ is estimated to be roughly 1% of that of the J/ψ, contributions from Υ decay contribute much less to the single-electron cocktail. A NLO pQCD calculation for Υ production in the color evaporation model provides the input to the Monte Carlo calculation of the central value estimates [68]. We apply the same relative systematic uncertainties derived from the J/ψ data to the Υ cocktail estimate. Compared to the quoted uncertainties in the NLO pQCD calculation, the use of data-driven systematic uncertainties for the Υ provides a more conservative estimate.

A leading-order (LO) Drell-Yan calculation [69] of the single-inclusive lepton p_T spectrum, $p + p \rightarrow (e^+ + e^-)/2 + X$, is also included in the updated electron cocktail. The calculation is for $|y| < 0.5$ and uses the CTEQ6M parton

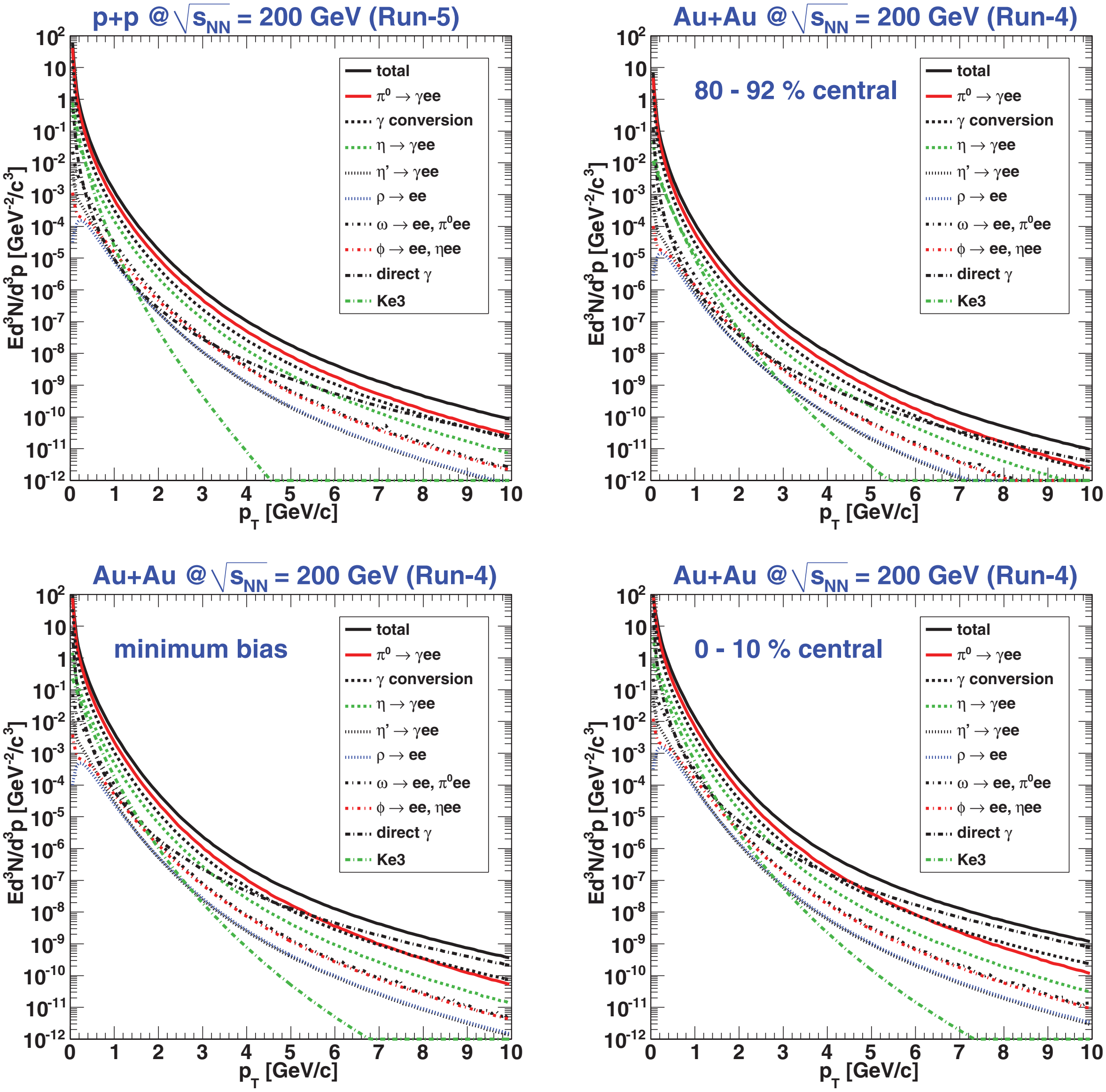

FIG. 14. (Color online) Invariant differential cross sections and multiplicities of cocktail electrons in $p + p$ and Au + Au collisions at 200 GeV for the indicated centrality ranges.

distributions [70]. The scale used is p_T, no cut is placed on the lepton pair mass, and a K factor of 1.5 is applied.

Figure 15 shows the cocktail for $p + p$ collisions with the quarkonium and Drell-Yan contributions. The bottom section of the plot shows the ratio of the cocktail with the quarkonium and Drell-Yan to that without.

PHENIX has measured the J/ψ p_T spectrum out to 5 GeV/c in Au + Au collisions at 200 GeV [71]. To extrapolate to higher p_T, the measured J/ψ spectrum from $p + p$ collisions is scaled by R_{AA} and N_{coll}. Above 5 GeV/c, two extreme scenarios are considered, and the difference in the two resulting estimates for the extrapolation is assumed as a systematic uncertainty. In the first scenario, the R_{AA} is kept constant from its value at 5 GeV/c. In the second scenario, the R_{AA} is assumed to increase linearly from its value at 5 GeV/c up to a value of 1 at 10 GeV/c, above which it is assumed to be constant. Figure 16 shows the cocktail with quarkonium and Drell-Yan contributions for 0%–20% centrality Au + Au collisions. The J/ψ spectrum in Au + Au collisions has not been measured separately for 0%–10% and 10%–20% centralities. To estimate the electron background in these centralities separately, we assume that the R_{AA} of J/ψ is the same in 0%–10% and 10%–20% centrality collisions.

Thus, we have a complete set of estimates and systematic uncertainties for the cocktail method to determine the heavy-flavor electron signal. In this analysis, the systematic uncertainty is of the same order as the signal-to-background ratio at the lowest p_T and, therefore, it is not sufficiently small to extract the heavy-flavor signal via the cocktail subtraction over the full p_T range. Hence, at low p_T, a complementary technique to subtract the background, the so-called "converter subtraction" method, is used to extend the heavy-flavor measurement to the lowest p_T with good precision. Consequently, the converter subtraction is the key

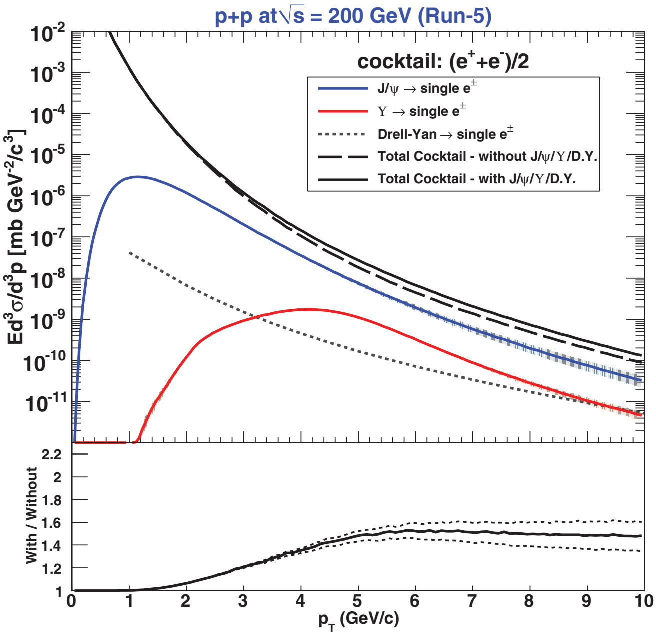

FIG. 15. (Color online) Electron background cocktail with quarkonium and Drell-Yan contributions for $p + p$ collisions. The shaded band (top panel) and dashed lines (bottom panel), respectively, reflect the uncertainty of the J/ψ contribution.

to extracting the total heavy-flavor yield or cross section because most of the electrons from heavy-flavor decays have low p_T. However, toward high p_T, for example, for $p_T > 2\ \text{GeV}/c$, where the converter subtraction starts to suffer from limited statistical precision, it is beneficial to apply the cocktail subtraction because the signal-to-background ratio is large, statistics is irrelevant owing to the Monte Carlo nature of the cocktail subtraction, and the cocktail input is known with small systematic uncertainties.

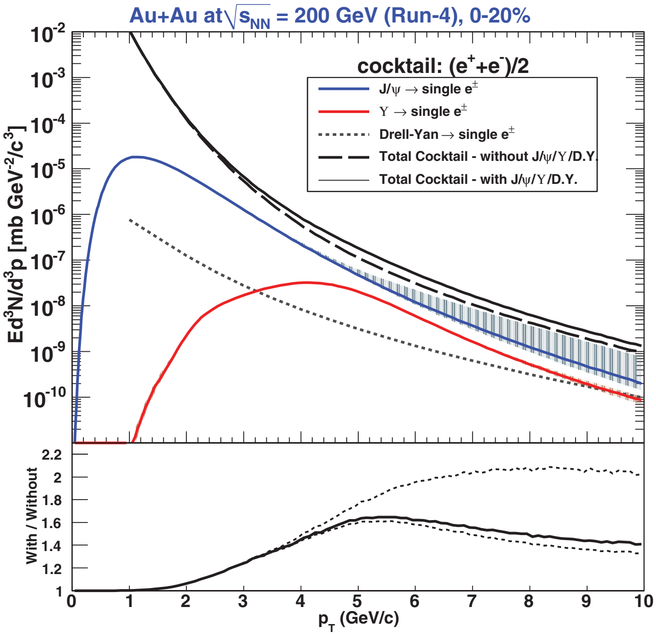

FIG. 16. (Color online) Electron background cocktail with quarkonium and Drell-Yan contributions for 0%–20% centrality Au + Au collisions. The shaded band (top panel) and dashed lines (bottom panel), respectively, reflect the uncertainty of the J/ψ contribution.

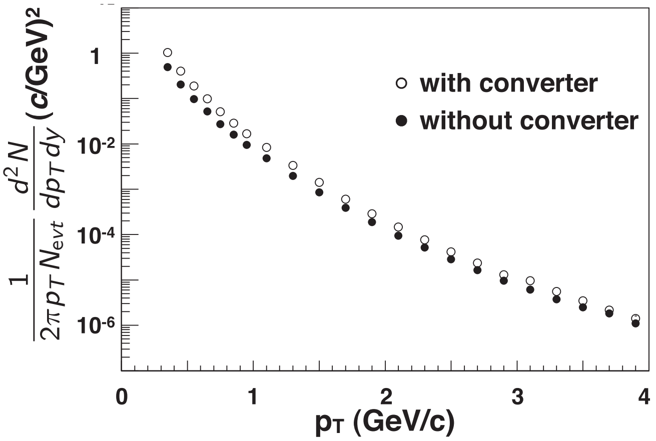

FIG. 17. Invariant yields of inclusive electrons with (open circles) and without (solid circles) the photon converter for Au + Au MB events.

J. Converter subtraction method

The yields of photonic and nonphotonic electrons are obtained by measuring the difference between inclusive electron yields with and without a photon converter of precisely known thickness: a brass sheet of 1.680% radiation length (X_0). Figure 17 shows the corresponding p_T^e spectra for Au + Au MB events.

These yields can be expressed as the following relations:

$$N_e^{\text{Conv-out}} = N_e^{\gamma} + N_e^{\text{Non-}\gamma}, \tag{7}$$

$$N_e^{\text{Conv-in}} = R_\gamma N_e^{\gamma} + (1-\epsilon) N_e^{\text{Non-}\gamma}. \tag{8}$$

Here $N_e^{\text{Conv-in}}$ ($N_e^{\text{Conv-out}}$) is the measured electron yield with (without) the converter. N_e^{γ} ($N_e^{\text{Non-}\gamma}$) is the photonic (nonphotonic) electron yield. ϵ represents a small loss of $N_e^{\text{Non-}\gamma}$ owing to the converter. This factor has been evaluated already in a previous measurement ($\epsilon \sim 2.1\%$) [26]. The main issue in this calculation is to determine R_γ, that is, to understand how much the photonic electron yield is increased by the converter. The main source of photonic electrons is a mixture of mesons (π^0, η, η', ω, and ϕ) decaying into real or virtual photons.

To calculate R_γ, it is necessary to know exactly the material amounts near the interaction point. Table VI shows a list of each material thickness in units of radiation length. The converter sheet was rolled just around the beam pipe in converter runs. The conversion probability (P^{Conv}) in Table VI is calculated for the case of electrons emitted at $p_T^e = 1.0\ \text{GeV}/c$. The equivalent conversion probability of a virtual photon in π^0 Dalitz decay (P^{Dalitz}) is 0.598% [72]. R_γ can be estimated with these values at $p_T^e = 1.0\ \text{GeV}/c$:

$$R_\gamma = \frac{P^{\text{Conv}} + P^{\text{Dalitz}}\ (\text{with converter})}{P^{\text{Conv}} + P^{\text{Dalitz}}\ (\text{without converter})} \sim 2.41. \tag{9}$$

TABLE VI. Radiation length (L) of material near the interaction point. The conversion probability ($P^{\rm Conv}$) is calculated for the case of electrons emitted at $p_T^e = 1.0$ GeV/c.

Material	L (X_0)	$P^{\rm Conv}$
Beam pipe (Be)	0.288%	0.201%
Air (r < 30 cm)	0.099%	0.069%
Total	0.387%	0.270%
Converter (brass)	1.680%	1.226%

To obtain a more realistic value of R_γ considering geometrical effects, GEANT-based Monte Carlo simulations [49] for photon conversions were performed with and without the converter. R_γ is determined for π^0 and η separately. We use the π^0 spectrum measured by PHENIX as the input for the π^0 simulation and assume m_T scaling, normalized at high p_T to $\eta/\pi^0 = 0.48 \pm 0.03$ to obtain the input for the η simulation. Because the η mass is larger than the π^0 mass, the phase space of η Dalitz decay is slightly larger than that of π^0 Dalitz decay. The relative branching ratio (Dalitz decay)/(two γ decay) is 1.2% for π^0 and 1.5% for η [73]. This difference makes R_γ^η smaller than $R_\gamma^{\pi^0}$. Contributions from other mesons which undergo Dalitz decay (η', ω, and ϕ) are small (6% at $p_T = 3$ GeV/c, and smaller at lower p_T). The particle ratios at high p_T (see Table V) are used to determine R_γ. The uncertainties in the particle ratios are included in the systematic uncertainties of R_γ. For this method, it is essential that the amount of material is accurately modeled in the simulation. We compared the yield of identified photon conversion pairs in the data and in the simulation, and concluded that the simulation reproduces R_γ within ±2.7%. This uncertainty is included in the overall systematic uncertainty.

In the top plot in Fig. 18, R_γ is indicated as a solid curve, which is compared with the ratio of the inclusive electron yield with/without the photon converter ($R_{\rm CN}$):

$$R_{\rm CN} \equiv \frac{N_e^{\rm Conv-in}}{N_e^{\rm Conv-out}} = \frac{R_\gamma + (1-\epsilon)R_{\rm NP}}{1 + R_{\rm NP}}. \tag{10}$$

Here $R_{\rm NP}$ is the ratio of nonphotonic/photonic electron yields ($N_e^{{\rm Non}-\gamma}/N_e^\gamma$). If there were no nonphotonic contributions ($R_{\rm NP} = 0$), then we would have $R_{\rm CN} = R_\gamma$. The top plot in Fig. 18 shows that $R_{\rm CN}$ gradually decreases with increasing p_T^e, while R_γ slightly increases with p_T^e. The difference between $R_{\rm CN}$ and R_γ proves the existence of nonphotonic electrons.

The converter method is applied for $0.3 \leqslant p_T^e < 1.6$ GeV/c, and the cocktail method is applied for $p_T^e \geqslant 1.6$ GeV/c. Boxes in the bottom plot in Fig. 18 are systematic uncertainties of $R_{\rm NP}$ from each method. $R_{\rm NP}$ increases with p_T^e and is more than 1.0 in $p_T^e \gtrsim 1.6$ GeV/c. This plot gives an important demonstration that the amount of conversion material is relatively small in PHENIX.

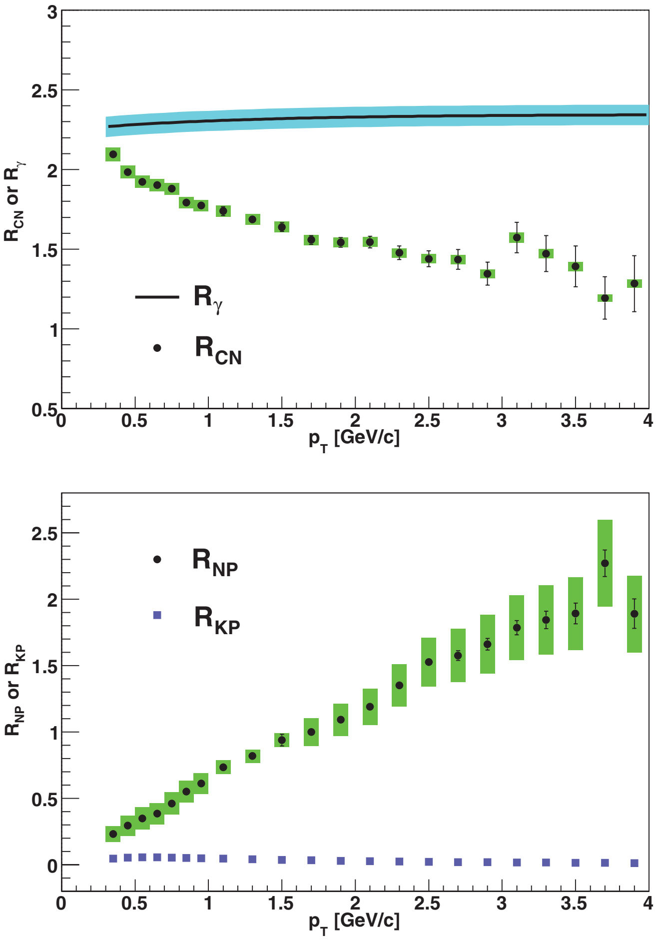

FIG. 18. (Color online) (Top) Ratio of inclusive electrons with/without the converter ($R_{\rm CN}$, points with systematic uncertainty boxes) and ratio of photonic electrons with/without the converter (R_γ, solid line with a systematic uncertainty band). (Bottom) The ratio of nonphotonic yield to photonic electron yield ($R_{\rm NP}$, solid circles) and the ratio of electron yield from kaon decays to photonic electron yield ($R_{\rm KP}$, solid squares) as a function of p_T^e for MB. Filled circles with statistical uncertainty bars indicate $R_{\rm NP}$ produced by both the converter and cocktail methods.

To tune the normalization of the photonic electron spectra in the cocktail, the converter/cocktail ratio of photonic electrons is calculated for all centrality classes in Au + Au collisions. The ratio in MB collisions is fitted by a constant (converter/cocktail = 1.182). The constant is applied to correct the cocktail spectra of photonic electrons for all centrality classes in Au + Au collisions.

PHENIX observed a large enhancement of direct photon production at low p_T ($p_T < 3$ GeV/c) in Au + Au collisions [62,63]. The fraction of direct photons in MB Au + Au events for $p_T < 5$ GeV/c is approximately 15%. This enhancement is not included in the present cocktail calculation. The relatively large renormalization factor, 1.182, is consistent with the enhanced direct photon production in Au + Au collisions. However, the systematic uncertainties in the cocktail are not sufficiently small to provide independent confirmation of the enhancement of low-p_T direct photons in Au + Au collisions.

It should be noted that the converter method is not affected by the enhancement of low-p_T direct photons. This is because the yield of photonic electrons measured by the converter method includes those from direct photons. Therefore, the

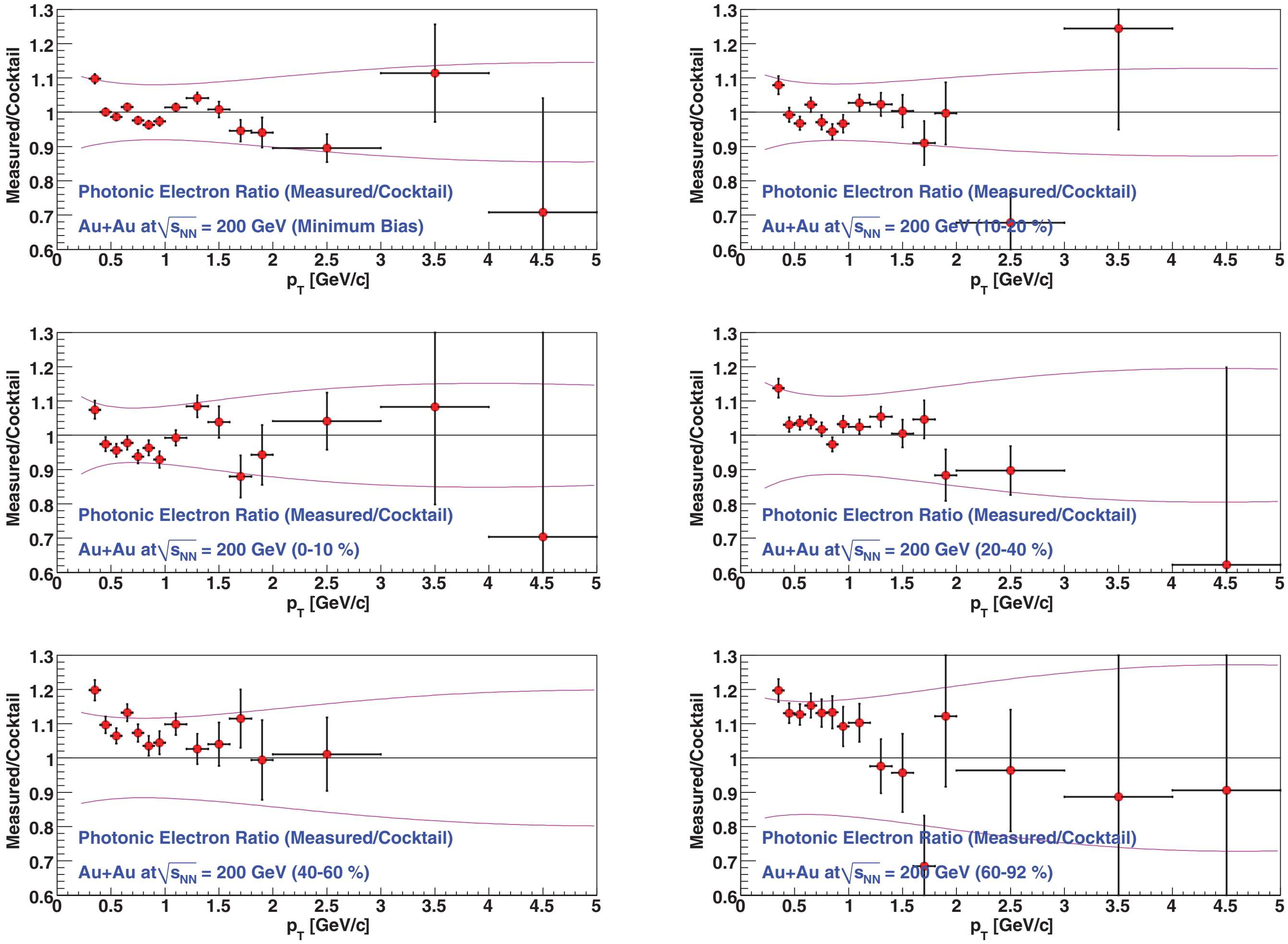

FIG. 19. (Color online) The ratio of photonic electrons measured by the converter method to the cocktail calculation in Au + Au collisions (after renormalizing the cocktail yields up by 18%) for the indicated centralities. The upper and lower curves show the systematic uncertainty of the cocktail. Uncertainty bars are statistical only.

photonic electron background from the enhanced direct photon yield is automatically subtracted in the converter method. This provides another reason for relying on the converter method to measure heavy-flavor electrons in the low-p_T region.

The ratios of the photonic electron yields from the converter method to those from the corrected cocktail method for all centrality classes in Au + Au collisions are shown in Fig. 19. The curves in each plot indicate the systematic uncertainties of the cocktail method.

In the $p + p$ data, the renormalization factor required to match the cocktail method with the converter measurement was found to be 0.94, well within the systematic uncertainty of the cocktail. Figure 20 shows the converter/cocktail ratio (after scaling by 0.94) of photonic electrons for $p + p$ collisions [29].

In the "converter subtraction" case, after removing the photonic electron background, almost all of the remaining background is from kaon decays. Kaons contribute to the nonphotonic electron spectra via K_{e3} decay and are only substantial for $p_T^e < 1$ GeV/c. From simulation, we compare kaon contributions with photonic and nonphotonic electrons. The ratio of the electron yield from kaon decays over the photonic electron yield (R_{KP}) is shown as solid squares in the bottom panel of Fig. 18. The background from kaons is less than 10% at low p_T and falls quickly above 1 GeV/c.

Figure 21 shows the ratio of nonphotonic electrons (including charmonium, bottomonium, and Drell-Yan) to the photonic background in $p + p$ collisions [29]. This confirms the excellent agreement between the cocktail and converter methods where they overlap in p_T and also indicates the large signal-to-background ratio at higher p_T.

K. Invariant spectra

The invariant cross section for single electrons from heavy-flavor decay in $p + p$ collisions is calculated using the following formula:

$$E\frac{d^3\sigma^{\mathrm{HF}}}{dp^3} = \frac{1}{\mathcal{L}}\frac{1}{2\pi p_{\mathrm{T}}}\frac{N_e^{\mathrm{HF}}}{\Delta p_T \Delta y}\frac{1}{A\epsilon_{\Delta y}^{\mathrm{acc}}}\frac{1}{\epsilon_{\mathrm{bias}}}, \tag{11}$$

where $\mathcal{L}$ is the integrated luminosity; N_e^{HF} is the electron yield from heavy-flavor decay after subtraction of photonic and nonphotonic background contributions; $A\epsilon_{\Delta y}^{\mathrm{acc}}$ is the product

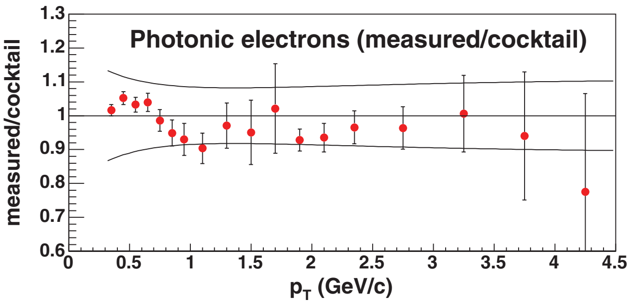

FIG. 20. (Color online) The ratio of photonic electrons measured by the converter method to the cocktail calculation in $p + p$ collisions [29]. The data from the MB (PH) data set are shown below (above) 1.8 GeV/c. The upper and lower curves show the systematic uncertainty of the cocktail. Uncertainty bars are statistical only.

of the geometrical acceptance and reconstruction efficiency described in Sec. III F; $\epsilon_{\rm bias} = 0.79 \pm 0.02$ is the BBC trigger bias described in Sec. III B. For the PH data set, $A\epsilon_{\Delta y}^{\rm acc}$ also includes the PH trigger efficiency described in Sec. III G. The cross sections from the MB and the PH data sets are consistent with each other in the overlapping p_T region.

In the Au + Au case, we quote the differential invariant yield spectra as a function of p_T^e calculated as in Eq. (12). $N_i^{\rm evt}$ is the number of events in a centrality class i (i = 0%–10%, 10%–20%, 20%–40%, 40%–60%, and 60%–92%). $\epsilon^{\rm hadron}(p_T^e)$ is the hadron contamination factor that is mentioned in Sec. III E. $\epsilon_{\Delta y}^{\rm acc}(p_T^e)$ is the acceptance correction from Sec. III F. $\epsilon_i^{\rm embed}$ is the embedding efficiency from Sec. III H. Δp_T^e is the p_T^e bin width. Δy is the rapidity range ($|y| < 0.5$) where the input $e^{\pm}$ are distributed at the first stage of single-particle simulation for the acceptance calculation (see Sec. III F). $N_i^{\rm HF}(p_T^e, e^-)$ and $N_i^{\rm HF}(p_T^e, e^+)$ are the resulting counts of signal electrons and positrons from heavy-flavor decays by the converter method or cocktail method:

$$\frac{1}{2\pi p_T^e}\frac{d^2N_i^{\rm HF}}{dp_T^e\,dy} \equiv \frac{1}{2\pi p_T^e N_i^{\rm evt}} \times \frac{1-\epsilon^{\rm hadron}(p_T^e)}{\epsilon_{\Delta y}^{\rm acc}(p_T^e)\cdot\epsilon_i^{\rm embed}} \times \frac{1}{\Delta p_T^e\,\Delta y} \times \frac{N_i^{\rm HF}(p_T^e, e^-) + N_i^{\rm HF}(p_T^e, e^+)}{2}. \qquad (12)$$

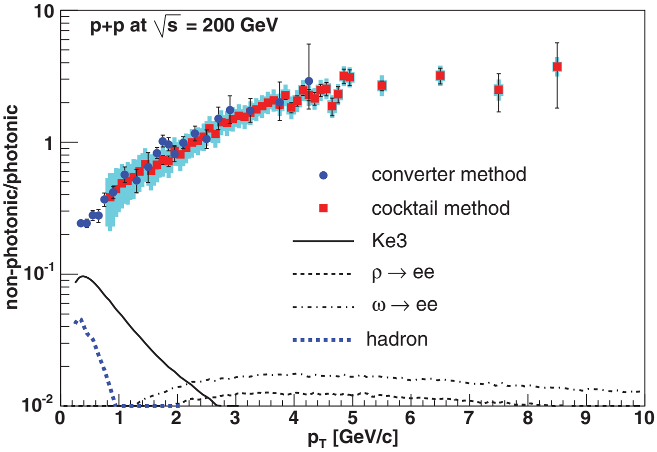

FIG. 21. (Color online) Ratio of nonphotonic electrons to photonic background in $p + p$ collisions [29]. Uncertainty bars are statistical uncertainties and the uncertainty band shows the cocktail systematic uncertainties. The solid, dashed, dot-dashed, and dotted curves are the remaining nonphotonic background from K_{e3}, $\rho \to e^+e^-$, $\omega \to e^+e^-$, and hadron contamination, respectively.

L. Systematic uncertainties in invariant spectra

In the $p + p$ analysis, systematic uncertainties are categorized into (a) inclusive electron spectra, (b) cocktail subtraction, and (c) converter subtraction. Category (a) is common to both the converter and the cocktail methods and includes the uncertainties in luminosity (9.6%), geometrical acceptance (4%), eID efficiency (3%) (from comparing to conversion electrons and simulation), and the PH trigger efficiency (3% at the plateau). Uncertainties in the cocktail subtraction [category (b)] include the normalization (8%) and p_T-dependent shape uncertainty (2% at $p_T \simeq 2$ GeV/c, increasing to 6% at 9 GeV/c). In the converter analysis [category(c)] the dominant uncertainties are in R_γ (2.7%) and in the relative acceptance between the converter and normal runs (1.0%).

In the Au + Au analysis there is no trigger efficiency correction, but there is additional uncertainty from the correction owing to multiplicity-dependent efficiency loss. A conservative systematic uncertainty of 4% is determined from the differences between the two columns in Table IV.

These uncertainties are propagated into the uncertainties in the heavy-flavor electron yields and added in quadrature. At low (high) p_T the uncertainties are amplified (reduced) to large (small) uncertainties in the heavy-flavor electron signal by approximately a factor of $1/(S/B)$, where S/B is the ratio of the heavy-flavor electron yield to the background (photonic and nonphotonic) electron yield.

M. Inclusive electron v_2

The value of the inclusive electron v_2 was measured with the reaction plane method which can be written as

$$\frac{dN}{d\phi} = N_0\,\{1 + 2v_2\cos[2(\phi - \Psi)]\}\,, \qquad (13)$$

where N_0 is a normalization constant, ϕ is the azimuthal angle of electrons, and Ψ is the reaction plane angle. The reaction plane was determined from the multiplicity in each segment of the BBCs. As the measurement of the reaction plane is sensitive to nonflow effects such as jets, resonance decays, and HBT correlations, the reaction plane was measured in two well-separated rapidity intervals. Because each BBC is roughly three units of pseudorapidity away from the central arms, nonflow effects in the reaction plane measurement are expected to be small. Figure 22 shows the azimuthal distribution of inclusive electrons for various centrality and p_T ranges, fit to the form of Eq. (13). One can see from the agreement between the curves and data points that higher-order Fourier coefficients do not contribute much to the measured azimuthal electron distribution. Using the reaction plane measured with the BBCs, the inclusive electron v_2 was

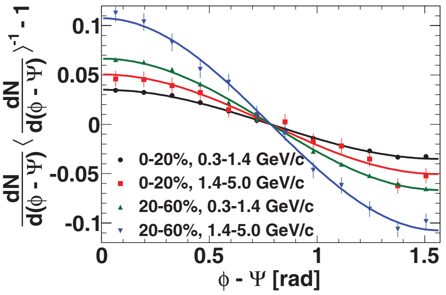

FIG. 22. (Color online) Azimuthal distributions relative to the reaction plane for various centrality and transverse momenta. The distributions have been normalized to their average value and centered around 0.

calculated as $v_2^{\text{meas}} = \langle \cos[2(\phi - \Psi_{\text{meas}})] \rangle$. The true v_2 with respect to the true reaction plane can be expressed in terms of the observed v_2 with respect to the measured reaction plane as [74,75]

$$v_2 = \frac{v_2^{\text{meas}}}{\langle \cos[2(\Psi_{\text{meas}} - \Psi_{\text{true}})] \rangle}. \tag{14}$$

Two methods were used to extract the correction for the reaction plane resolution $\langle \cos[2(\Psi_{\text{meas}} - \Psi_{\text{true}})] \rangle$. The first is an analytical calculation [74,75],

$$\begin{aligned} &\langle \cos[2(\Psi_{\text{meas}} - \Psi_{\text{true}})] \rangle \\ &\quad = \frac{\sqrt{\pi}}{2\sqrt{2}} \chi \exp\left(\frac{-\chi^2}{4}\right) \left[I_0\left(\frac{\chi^2}{4}\right) + I_1\left(\frac{\chi^2}{4}\right) \right], \end{aligned} \tag{15}$$

where χ is equal to $v_2^{\text{meas}} \sqrt{2N}$ and N is the BBC multiplicity. This method was verified to be well approximated by [75]

$$\langle \cos[2(\Psi_{\text{meas}} - \Psi_{\text{true}})] \rangle \sim \sqrt{2 \langle \cos[2(\Psi^N_{\text{meas}} - \Psi^S_{\text{meas}})] \rangle}, \tag{16}$$

where $\Psi^{N(S)}_{\text{meas}}$ is the measured reaction plane using only the north (south) BBC. Figure 23 shows the correction for the reaction plane resolution determined from Eq. (16).

The sample of identified electrons contains less than 10% background predominantly from accidental RICH hit associations with charged hadrons. These background contributions were subtracted as

$$\frac{dN}{d(\phi - \Psi)} = \frac{dN^e_{\text{cand}}}{d(\phi - \Psi)} - \frac{dN^e_{\text{back}}}{d(\phi - \Psi)}, \tag{17}$$

where N^e_{cand} is the number of electrons identified by the RICH and N^e_{back} is the number of the background particles. The number of random associations are obtained by replacing the north and the south sides of the RICH in the software, as described previously. The v_2 for a given centrality bin $[a, b]$ can be expressed as

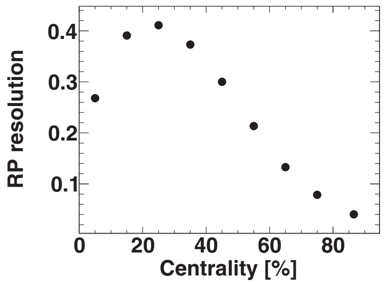

FIG. 23. Reaction plane resolution as a function of centrality.

$$v_2^{\text{bin}} = \frac{\int_a^b \frac{v_2^{\text{meas}}(C) \frac{dN_{e^+,e^-}}{dC}}{\text{res}(C)} dC}{\int_a^b \frac{dN_{e^+,e^-}}{dC} dC}, \tag{18}$$

where res(C) is the correction for reaction plane resolution for a given centrality C. Owing to limited statistics, Eq. (18) was approximated by a numerical sum over 10% centrality bins. It was verified that v_2 is not sensitive to changing the bins for the sum. This is because the integrand in the numerator of Eq. (18) is quite flat with centrality, as the resolution improves with both the measured v_2 and the particle multiplicity. Figure 24 shows the transverse momentum and centrality dependence of the inclusive electron v_2. The MB v_2 is shown in Fig. 25.

N. Background v_2 cocktail

The azimuthal distribution of inclusive electrons ($dN^e/d\phi$) is given as the sum of the azimuthal distributions of photonic electrons ($dN^\gamma/d\phi$) and nonphotonic electrons ($dN^{\text{non}-\gamma}/d\phi$):

$$\frac{dN_e}{d\phi} = \frac{dN_e^\gamma}{d\phi} + \frac{dN_e^{\text{non}-\gamma}}{d\phi}. \tag{19}$$

From the Fourier expansion of Eq. (19) the nonphotonic electron v_2 can be expressed as

$$v_{2_e}^{\text{non}-\gamma} = \frac{(1 + R_{\text{NP}}) v_{2_e} - v_{2_e}^\gamma}{R_{\text{NP}}}, \tag{20}$$

where v_{2_e} is the v_2 of inclusive electrons, $v_{2_e}^\gamma$ is the v_2 of the photonic electrons, and R_{NP} is the ratio of nonphotonic to photonic electron yields, which was defined in Sec. III J. The photonic electron v_2 can be estimated from the v_2 of electrons from various photonic sources as

$$v_2^\gamma = \sum R_i v_{2_e}^i, \tag{21}$$

where R_i is the relative contribution of electron source i to the background and v_2^i is the electron v_2 from the electron source.

The dominant sources of photonic electrons are photon conversions and Dalitz decays from π^0, with additional contributions from η mesons. The relative contributions of electrons from these sources are shown in Fig. 26. Other sources, owing to their small contribution, were ignored when calculating the photonic electron v_2. The measured v_2 for $\pi^\pm$ and π^0 was used as input for a simulation of $\pi^0 \to e^\pm$ v_2, and transverse kinetic energy scaling [76] was assumed for the η. The direct photon v_2 was assumed to be zero. The simulated π^0 and η v_2 and the resulting decay electron v_2 as a function

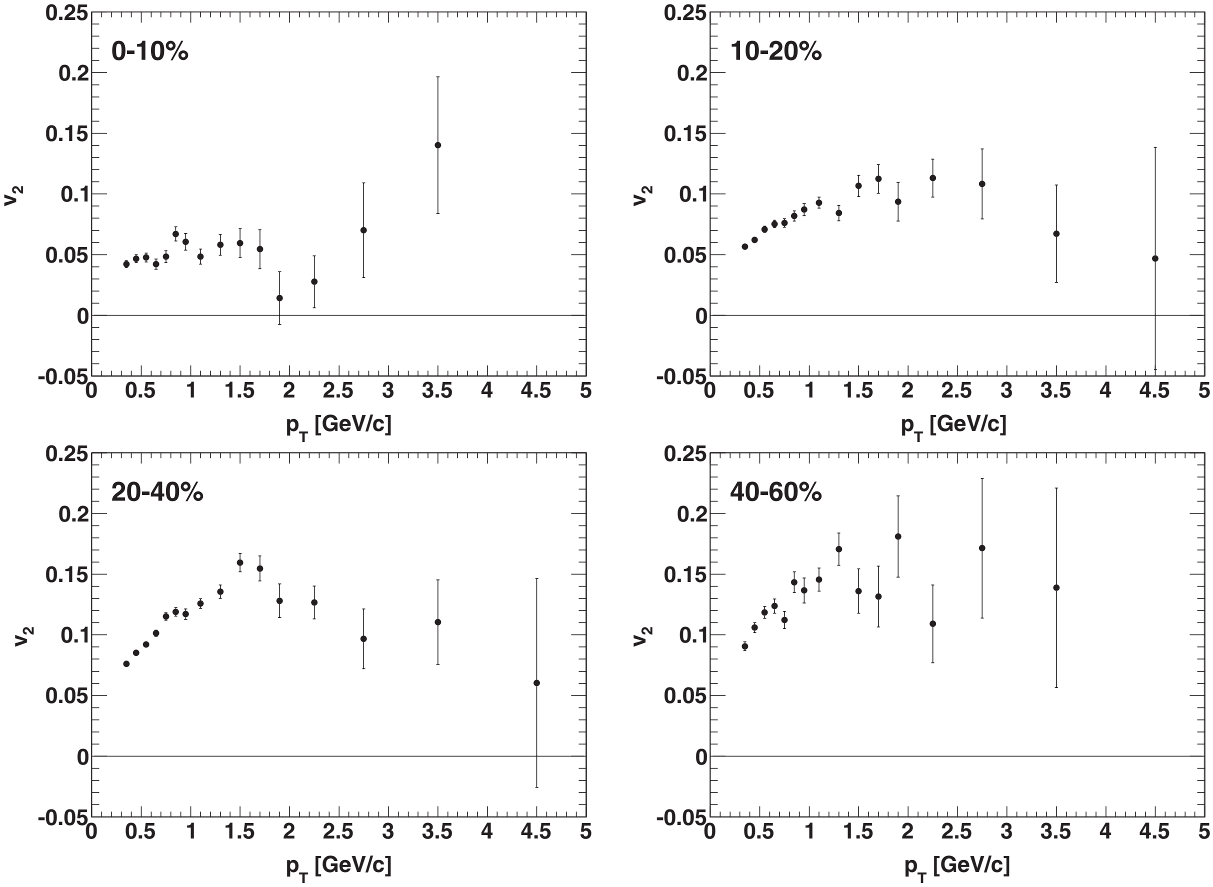

FIG. 24. p_T dependence of inclusive electron v_2, for different centrality bins. A 5% systematic scale uncertainty is not shown.

of p_T are shown in Figs. 27 and 28. The total v_2 from photonic sources for various centralities is shown in Fig. 29.

O. Photonic v_2 converter method

The photonic electron v_2 can be also determined by the converter method. Nonphotonic and photonic electron v_2 can be separated by using the inclusive electron v_2 measured with ($v_{2_e}^{\text{conv-in}}$) and without ($v_{2_e}^{\text{conv-out}}$) the converter as

$$v_{2_e}^{\text{non}-\gamma} = \frac{R_\gamma(1+R_{\text{NP}})v_{2_e}^{\text{conv-out}} - (R_\gamma+R_{\text{NP}})v_{2_e}^{\text{conv-in}}}{R_{\text{NP}}(R_\gamma-1)}, \tag{22}$$

$$v_{2_e}^{\gamma} = \frac{(1+R_{\text{NP}})v_{2_e}^{\text{conv-out}} - (R_\gamma+R_{\text{NP}})v_{2_e}^{\text{conv-in}}}{(1-R_\gamma)}. \tag{23}$$

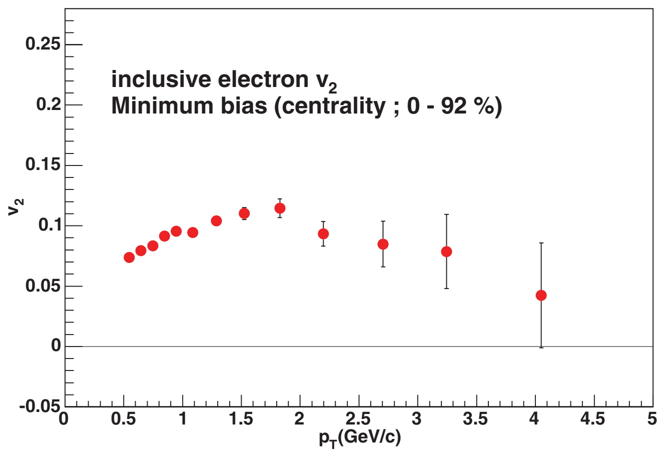

FIG. 25. (Color online) Inclusive electron v_2 for MB events as a function of p_T measured in Au + Au collisions at $\sqrt{s_{\text{NN}}} = 200$ GeV.

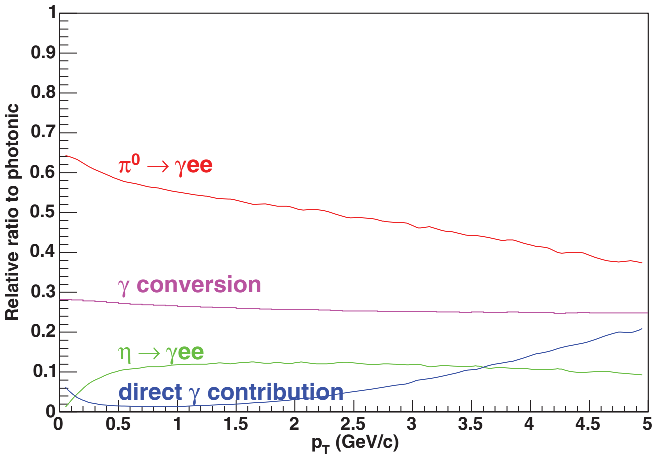

FIG. 26. (Color online) Relative contributions of electrons from π^0, η, and direct γ to the background.

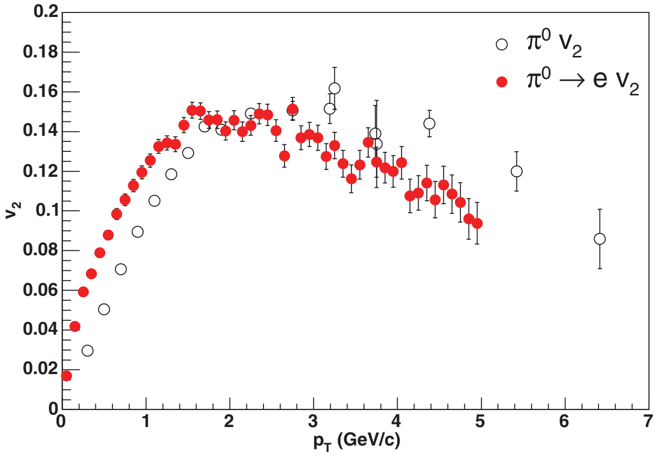

FIG. 27. (Color online) Electron v_2 from π^0 decay as a function of p_T, from a simulation.

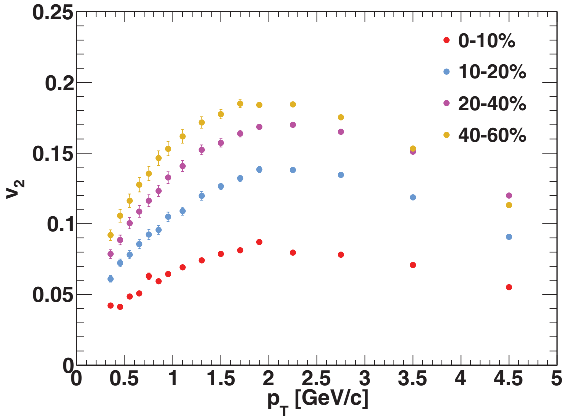

FIG. 29. (Color online) Electron v_2 from photonic sources as a function of p_T and centrality.

Figure 30 shows the inclusive electron v_2 with and without the converter. If the photonic electrons and nonphotonic electrons have the same v_2, the v_2 measured with and without the converter would be the same. Owing to the small statistics of the converter runs, v_2 measured with the converter has a large statistical uncertainty. The photonic electron v_2 obtained by the converter method is shown as open squares in Fig. 31. The result is consistent with the photonic electron v_2 determined by the cocktail method within statistical uncertainties.

P. Heavy-flavor v_2 and systematic uncertainties

The remaining background after subtracting the photonic background is dominated by kaon decay as described previously. The electron v_2 from kaon decays was also calculated by a Monte Carlo simulation assuming transverse kinetic energy scaling and it was removed from the nonphotonic electron v_2 as

$$v_{2_e}^{\text{heavy}} = \frac{v_{2_e}^{\text{non}-\gamma} - R_{\text{KNP}} v_{2_e}^{K}}{1 - R_{\text{KNP}}}. \tag{24}$$

Here R_{KNP} is the ratio of the yield of electrons from kaon decays and from all other nonphotonic sources ($R_{\text{KNP}} = N_e^K/N_e^{\text{non}-\gamma}$), and $v_{2_e}^{\text{heavy}}$ is the v_2 of electrons from heavy-flavor decays. After subtracting kaon decays, the main source of nonphotonic electrons remaining is heavy-flavor decays.

Systematic uncertainties of the heavy-flavor electron v_2 are summarized below.

(i) Reaction plane determination: The systematic uncertainty in the reaction plane determination was estimated by measuring the inclusive electron v_2 separately with the north BBC, the south BBC, and both the north and the south BBCs combined. The maximum difference is ~5%, and we apply it as the uncertainty owing to the reaction plane determination.

(ii) Electron identification: The systematic uncertainty from eID was estimated by measuring the inclusive electron v_2 while changing the eID cuts from the standard cuts, which were described previously. In this analysis we changed the cut parameters of **E/p**, **n0**, and χ^2/**npe0**. The relative change in v_2 from varying the cuts on **E/p** is about 2%, while for **n0** it is about 2%, and for χ^2/**npe0** it is 1%. The total systematic uncertainty assigned from eID is 3%.

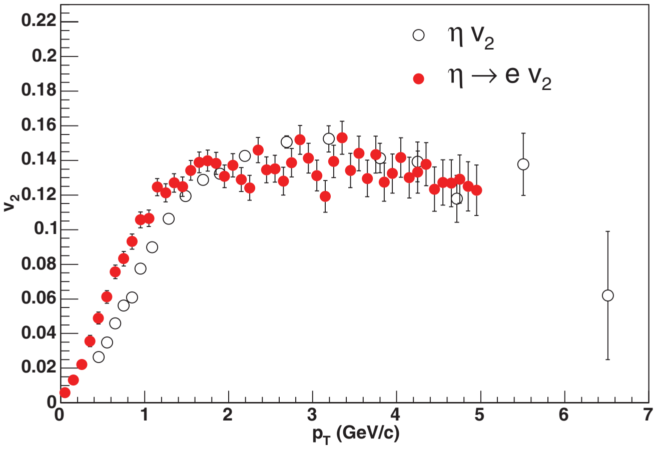

FIG. 28. (Color online) Electron v_2 from η decay as a function of p_T, from a simulation.

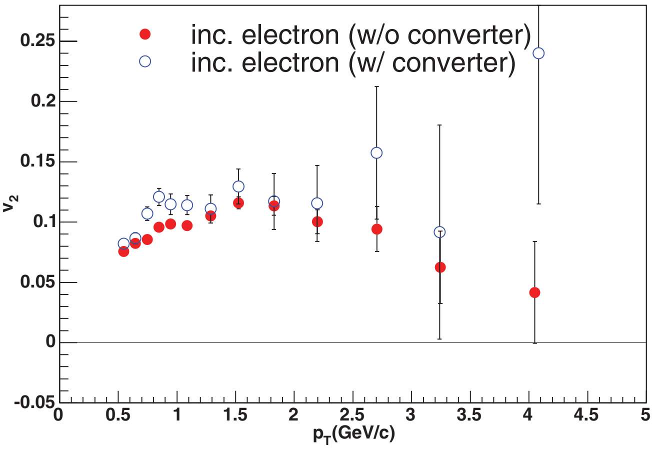

FIG. 30. (Color online) Inclusive electron v_2 with and without the converter installed.

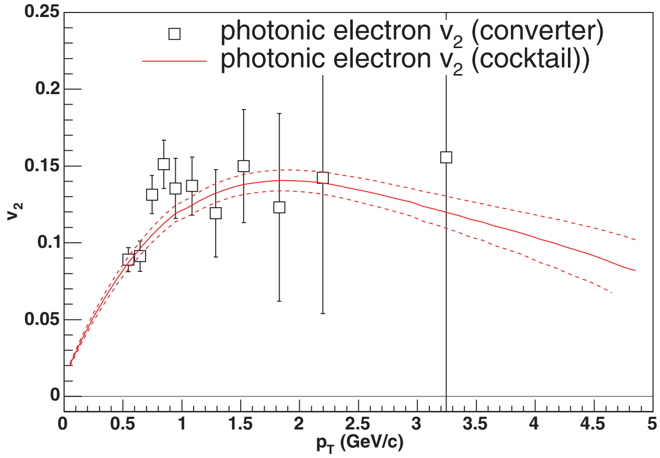

FIG. 31. (Color online) Photonic electron v_2 from MB Au + Au collisions determined by two independent methods, the cocktail and the converter method. The lines are determined by the cocktail method and the data points shown with square symbols are obtained by the converter method.

(iii) Background v_2: As described in the previous section, the uncertainties from the photonic electron v_2 arise from the π^0 v_2 and η v_2, which have about 5% uncertainties. We applied these values to the uncertainty of the photonic electron v_2. We also applied 5% for the v_2 from three-body kaon decays.

(iv) R_{NP}: The systematic uncertainty on R_{NP} is attributable to the uncertainties of inclusive electron spectra and the subtracted background spectra. The systematic uncertainty on the inclusive electron spectra includes the uncertainties in the geometrical acceptance, the reconstruction efficiency, and the occupancy correction, as described previously.

The total systematic uncertainty was obtained by a quadratic sum of the above uncertainties.

IV. RESULTS

A. Heavy-flavor electron cross section ($p + p$)

After applying all corrections and systematic uncertainties, we combine the final heavy-flavor electron spectrum from the two analysis methods (cocktail and converter). At low p_T ($p_T < 1.6$ GeV/c) the converter subtraction method is applied to the MB data set. At intermediate p_T ($1.6 < p_T < 2.6$ GeV/c) the converter method is applied to the PH triggered data set. At high p_T ($p_T > 2.6$ GeV/c) the cocktail method is applied to the PH triggered data set. Figure 32(a) shows the final invariant differential cross section for heavy-flavor electrons in $p + p$ collisions at $\sqrt{s} = 200$ GeV [29]. The uncertainty bars represent statistical point-to-point uncorrelated uncertainties and the boxes represent systematic point-to-point correlated uncertainties. Also shown is a fixed order next-to-leading log (FONLL) pQCD calculation for the heavy-flavor contributions to the electron spectrum [77]. Figure 32(b) shows the experimental data divided by the FONLL calculation. Also shown in Fig. 32 are curves for the scale uncertainties in the theoretical calculation, but an additional 10% global scale uncertainty is not shown in either panel. Within the experimental and theoretical uncertainties, there is agreement on the combined charm and bottom contributions to the measured electron spectrum. Recently, the STAR experiment measured the heavy-flavor electron cross section in $p + p$ at 200 GeV [78]. Their data are in good agreement with the PHENIX data [29] presented in Fig. 32.

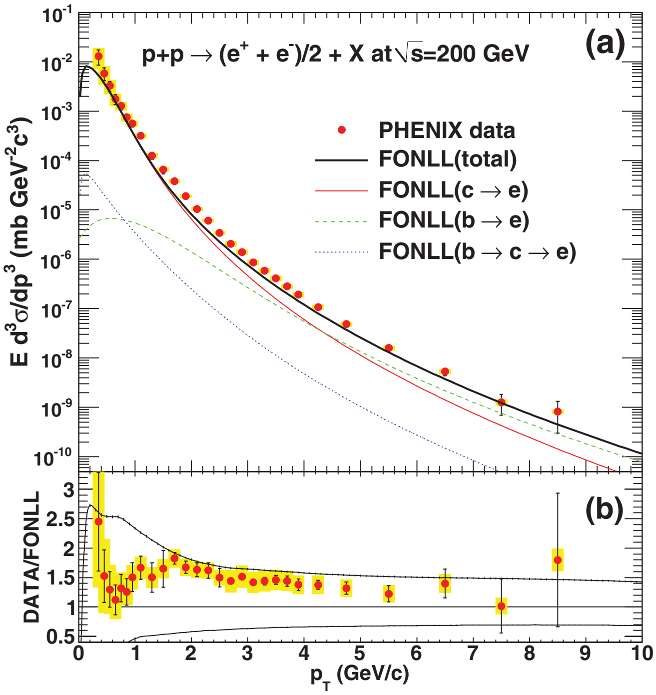

FIG. 32. (Color online) (a) Invariant differential cross sections of single electrons as a function of p_T in $p + p$ collisions at $\sqrt{s} = 200$ GeV [29]. The uncertainty bars (bands) represent the statistical (systematic) uncertainties. The curves are the FONLL calculations [77]. (b) The ratio of Data/FONLL as a function of p_T. The upper (lower) curve shows the theoretical upper (lower) limit of the FONLL calculation. In both panels, a 10% normalization uncertainty is not shown.

B. Heavy-flavor electron invariant yield (Au + Au)

Figure 33 shows the final invariant yield of inclusive (left panel) and heavy-flavor electrons (right panel) in Au + Au collisions for various ranges in centrality. From top to bottom the spectra correspond to data in MB events, the five centrality classes, and the $p + p$ data (converted from invariant cross section to invariant yield). The Au + Au spectra are produced by the converter method for $0.3 < p_T < 1.6$ GeV/c and by the cocktail method for $1.6 < p_T < 9.0$ GeV/c. The boxes and bars are systematic and statistical uncertainties for each data point, respectively.

The heavy-flavor electron spectrum in $p + p$ collisions is fit to a spectral shape taken from the FONLL calculation [77]. Then this fit function is scaled up by the average number of binary collisions and drawn for comparison with each Au + Au centrality selected invariant yield. The Au + Au data agree with the scaled curves for peripheral events and at low p_T, but fall increasingly below the curves at high p_T and

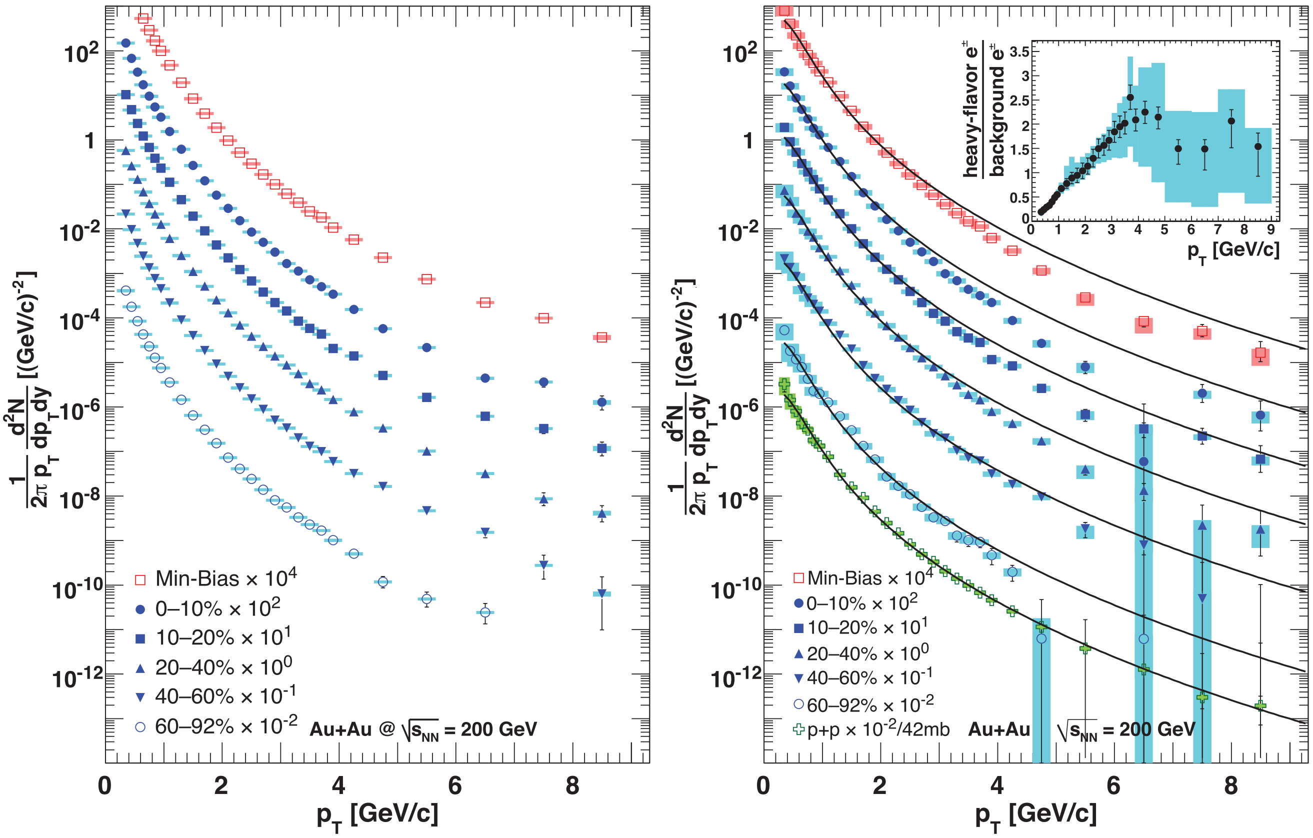

FIG. 33. (Color online) Invariant yields of (left) inclusive electrons and (right) open heavy-flavor electrons for different Au + Au centrality classes, scaled by powers of 10 for clarity. Uncertainty bars (boxes) depict statistical (systematic) uncertainties. The insert shows the ratio of these electrons to those from background sources in MB events. The curves are scaled fits to the $p + p$ spectrum.

for more central collisions. To quantify the suppression, the nuclear modification factor is calculated in the next section. The inset in the right panel of Fig. 33 shows the ratio of signal to background as a function of p_T for MB events. This signal-to-background ratio (R_{SB}) is calculated as

$$R^{\mathrm{SB}} = \frac{N_e^{\mathrm{HF}}}{N_e^{\gamma} + N_e^{\mathrm{KV}}} = \frac{N_e^{\mathrm{Non-}\gamma} - N_e^{\mathrm{KV}}}{N_e^{\gamma} + N_e^{\mathrm{KV}}}. \tag{25}$$

Here $N_e^{\mathrm{Non-}\gamma}$ is the measured nonphotonic electron yield, N_e^{γ} is the yield of photonic electron background, and N_e^{KV} is the yield of electron backgrounds from kaons, vector mesons, quarkonia, and Drell-Yan. Solid circles with statistical uncertainty bars show R^{SB} produced by both the converter and the cocktail methods. Boxes are systematic uncertainties of R_{SB}. The signal-to-background ratio increases rapidly with p_T, reaching one for $p_T \approx 1.5$ GeV/c, reflecting the prominent heavy-flavor signal and the small amount of conversion material in the detector acceptance.

C. Nuclear modification factor $R_{\mathrm{AA}}(p_T)$

The nuclear modification factor is defined as follows:

$$R_{\mathrm{AA}}(p_T^e) = \frac{dN_{\mathrm{AuAu}}^e/dp_T^e}{\langle N_{\mathrm{coll}}\rangle \times dN_{pp}^e/dp_T^e} \tag{26}$$

$$= \frac{dN_{\mathrm{AuAu}}^e/dp_T^e}{\langle T_{\mathrm{AuAu}}\rangle \times d\sigma_{pp}^e/dp_T^e}, \tag{27}$$

where $dN_{\mathrm{AuAu}}^e/dp_T^e$ is the differential invariant yield in Au + Au collisions and dN_{pp}^e/dp_T^e ($d\sigma_{pp}^e/dp_T^e$) is the differential invariant yield (cross section) in $p + p$ collisions at a given p_T^e bin. For $p_T^e < 1.6$ GeV/c, dN_{pp}^e/dp_T ($d\sigma_{pp}^e/dp_T^e$) is taken point by point from the $p + p$ data. At higher p_T, the fits shown in Fig. 33 are used to remove statistical fluctuations, and the statistical uncertainty is moved to a systematic uncertainty in the shape of R_{AA}. $T_{\mathrm{AuAu}}(b)$ is the nuclear thickness function as previously defined.

$R_{\mathrm{AA}}(p_T^e)$ for each centrality class is shown in Fig. 34. Systematic uncertainties comprise contributions from T_{AuAu} [a rectangular box drawn around $R_{\mathrm{AA}}(p_T^e) = 1.0$] and from $p + p$ and Au + Au data (boxes for each data point). The statistical uncertainties are shown as vertical bars for each data point. Data points and uncertainties for each centrality class are tabulated in the Appendix.

If no nuclear modification exists and binary scaling is correct, R_{AA} should be unity. In all centrality classes, R_{AA} is consistent within uncertainties with unity for $p_T < 2$ GeV/c. However, we can see very clear suppression for 0%–10%, 10%–20%, 20%–40%, and MB events in the high-p_T region.

D. Integrated $R_{\mathrm{AA}}(N_{\mathrm{part}})$

It is also interesting to ask if the total number of charm quarks produced scales with the number of binary collisions, and thus R_{AA} reflects the medium modifying their momentum distribution only. Therefore, we calculate the p_T^e-integrated

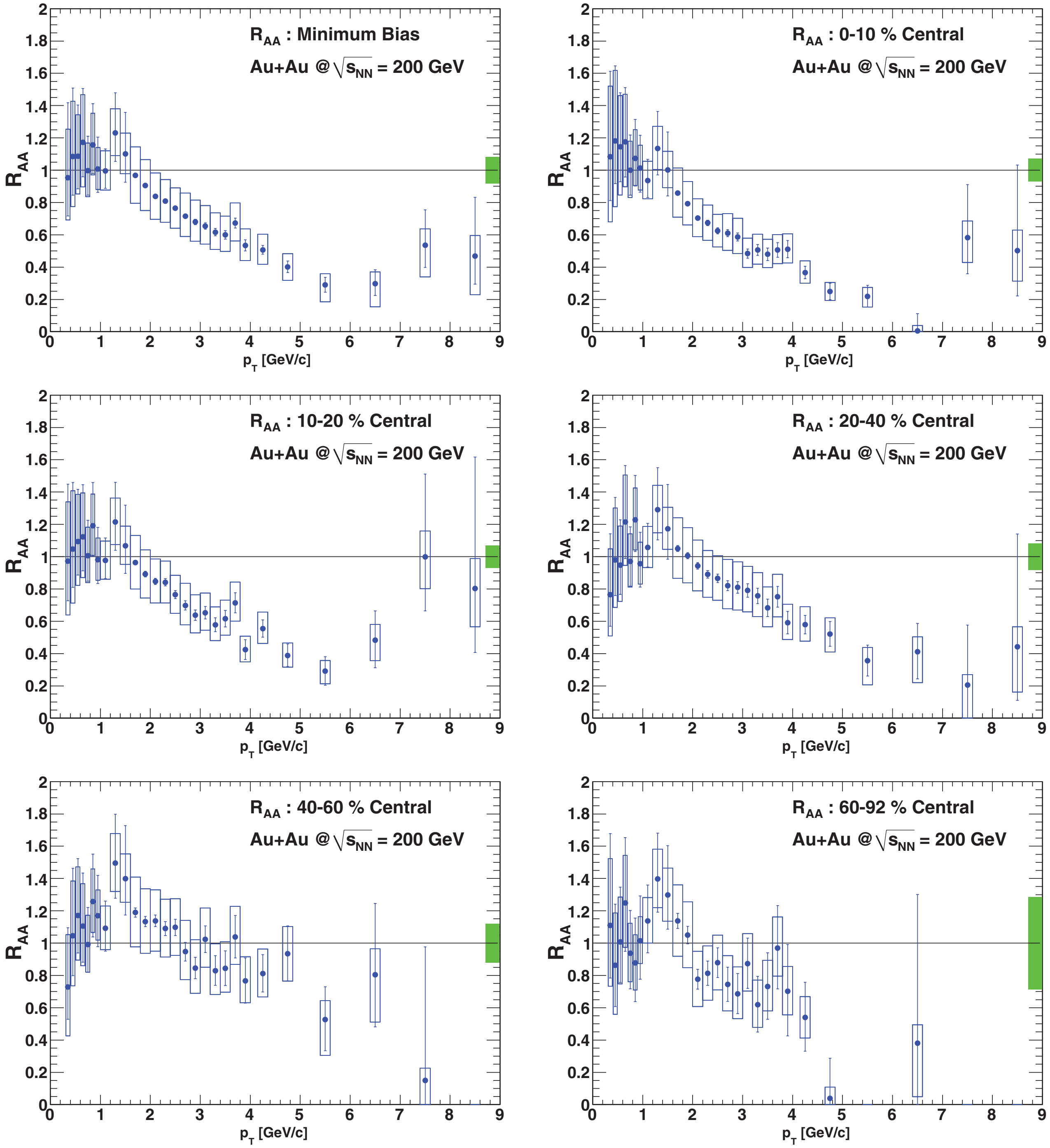

FIG. 34. (Color online) Open heavy-flavor electron R_{AA} for the indicated centralities. The boxes show the point-to-point correlated systematic uncertainty.

R_{AA} as a function of N_{part} as

$$R_{\mathrm{AA}}^{p_T^e}(N_{\mathrm{part}}) = \frac{N^e_{\mathrm{AuAu}}(p_T)}{\langle T_{\mathrm{AuAu}}\rangle \times \sigma^e_{\mathrm{pp}}(p_T)} = \frac{N^e_{\mathrm{AuAu}}(p_T)}{\langle N_{\mathrm{coll}}\rangle \times N^e_{\mathrm{pp}}(p_T)}, \tag{28}$$

where $N^e_{\mathrm{AuAu}}(p_T)$ is the total electron yield above a transverse momentum of p_T. Figure 35 shows $R_{\mathrm{AA}}^{p_T^e}(N_{\mathrm{part}})$ for electrons from heavy-flavor decays for six different integrated p_T^e ranges as a function of the number of participant nucleons, N_{part}. When the lower limit of integration is reduced to $p_T^e = 0.3$ GeV/c, which includes more than half of the heavy-flavor decay electrons predicted by the FONLL calculation in $p + p$ collisions, R_{AA} is close to unity for all N_{part}. This behavior suggests that the total yield of electrons from heavy-flavor decays in Au + Au collisions is the same as the binary-scaled yield in $p + p$ collisions. The observed strong suppression

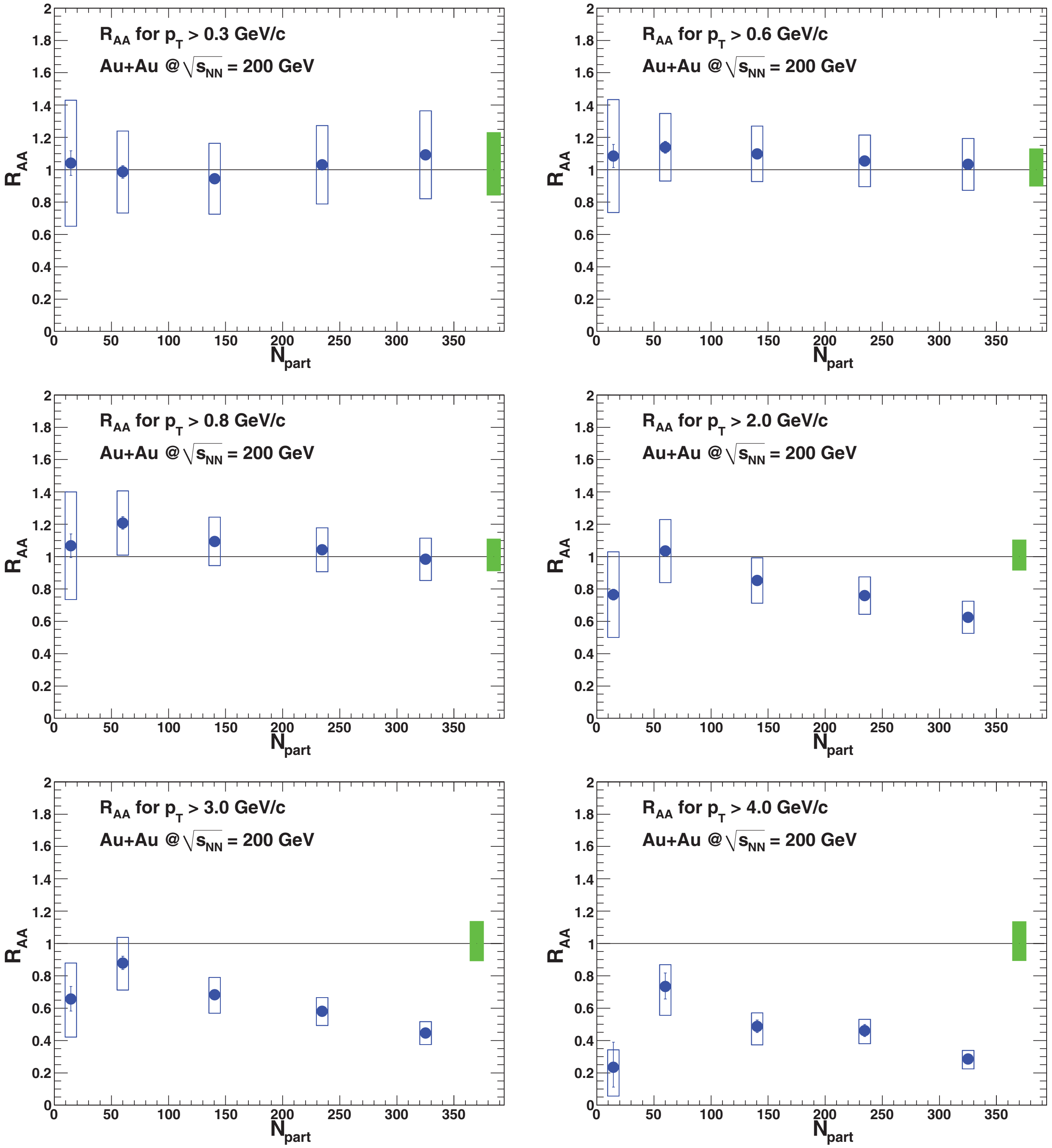

FIG. 35. (Color online) Nuclear modification factors R_{AA} for open heavy-flavor electrons vs centrality, integrated above the indicated p_T^e ranges.

phenomenon can be interpreted as softening of the heavy-quark momentum spectrum. For $p_T^e > 0.6$, 0.8, 2.0, 3.0, and 4.0 GeV/c, R_{AA} decreases systematically with centrality. The behavior seems to be similar to the observed suppression for π^0 and η mesons [6,55]. However, quantitative comparison with the suppression of the light mesons requires an understanding of the decay kinematics of open charm and bottom mesons.

E. Total charm cross section

We now determine the total charm cross section in $p + p$ from the heavy-flavor electron invariant cross sections shown in Fig. 32. The heavy-flavor electron cross section at low p_T is dominated by charm, while the bottom contribution is small, of order 1%.

We use the following prescription to determine the total charm cross section.

(i) The invariant cross section is extrapolated to $p_T = 0$ to obtain the integrated cross section $d\sigma^e/dy$ at $y = 0$ over all p_T.

(ii) The cross section is converted to a charm cross section at $y = 0$ ($d\sigma_{c\bar{c}}/dy|_{y=0}$) using

$$\frac{d\sigma_{c\bar{c}}}{dy} = \frac{1}{BR(c \to e)} \frac{1}{C_{e/D}} \frac{d\sigma^e}{dy}. \qquad (29)$$

Here $BR(c \to e)$ is the total charm to electron branching ratio, and $C_{e/D} = 0.935$ is a kinematic correction factor to account for the difference between the rapidity distribution of electrons and D mesons.

(iii) Finally, the cross section is extrapolated to the entire rapidity range to obtain the total charm production cross section $\sigma_{c\bar{c}}$.

We use two methods for step 1. In the first method, the total charm cross section in $p + p$ collisions is derived by numerically integrating the heavy-flavor electron cross section for $p_T > 0.4$ GeV/c: $d\sigma_e(p_T > 0.4)/dy = 5.79 \pm 0.59 \pm 1.64$ μb. Here the systematic uncertainty is obtained by integrating the upper and the lower systematic uncertainty limits of the differential cross section. We do not include the lowest p_T point, at $p_T = 0.35$ GeV/c, because this point's large individual uncertainty would make the uncertainty in the numerical integral much larger. The cross section is then extrapolated for the $p_T =$ 0–0.4 GeV/c bin using the spectral shape predicted by the FONLL calculation. This results in $d\sigma_e(p_T > 0)/dy = 10.6 \pm 1.1 \pm 3.2$ μb. Here we have assigned an additional 10% systematic uncertainty, representing a 25% uncertainty on the extrapolated contribution on the cross section for $p_T < 0.4$ GeV/c. We have also subtracted the small contributions from $b \to e$ and $b \to c \to e$ cascade decays (0.1 μb).

In the second method for step 1, we use PYTHIA to calculate the spectral shape from charm decay electrons. We have studied the PYTHIA results with a range of $\langle k_T \rangle$ values from 1.5 to 3.5 GeV/c and show the resulting electron spectra in comparison with the experimental data in Fig. 36. Note that the curves are fit to the experimental data with a single normalization parameter, and thus the PYTHIA shape is preserved. The PYTHIA curves reasonably describe the experimental data below $p_T \approx 1.6$ GeV/c, which is the p_T range that is important for the total cross section.

The five PYTHIA curves are very similar in the low-p_T region, because the electron spectra there are mainly determined by the D-meson decay kinematics. Because the solid black curve ($\langle k_T \rangle = 2.5$ GeV/c) describes the data well, we use it as the central value. We note that similar values of $\langle k_T \rangle$ are found in our two hadron correlation analyses in $p + p$ [79].

Using this second method, we obtained $d\sigma^e/dy$ ($p_T > 0) = 10.9 \pm 0.6 \pm 2.8$ μb. We have included an additional systematic uncertainty of ± 1.4 μb for this extrapolation procedure. This systematic uncertainty is estimated as 50% of the difference of the cross section with $\langle k_T \rangle = 3.5$ GeV/c (minimum cross section) and with $\langle k_T \rangle = 1.5$ GeV/c (maximum cross section). Because the second method gives a value of $d\sigma^e/dy$ very close to that of the first method, we use the value obtained from the first method in the charm cross section calculation.

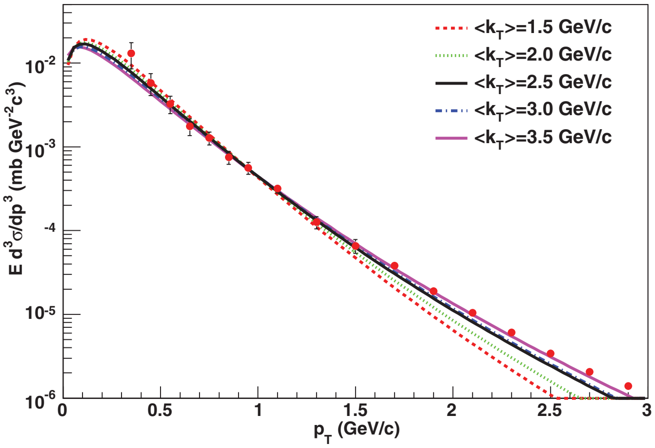

FIG. 36. (Color online) Comparison of electron p_T distributions calculated by PYTHIA and the data (solid circles). The five curves are electron p_T distributions from charm decay calculated using PYTHIA with different $\langle k_T \rangle$ values shown in the legend. All five curves are normalized to the data for $0.3 < p_T < 1.6$ GeV/c.

For step 2, we determine the charm production cross section, $d\sigma_{c\bar{c}}/dy = 119 \pm 12 \pm 38$ μb using Eq. (29). The branching ratio, $BR(c \to e) = 9.5 \pm 1.0\%$, is calculated using the following charmed hadron ratios: $D^+/D^0 = 0.45 \pm 0.10$, $D_s/D^0 = 0.25 \pm 0.10$, and $\Lambda_c/D^0 = 0.1 \pm 0.05$. In step 3, we calculate the rapidity distribution of charm quarks using NLO pQCD [80] with parton-distribution functions from coordinated theoretical/experimental project on QCD (CTEQ5) [81]. The total charm cross section is determined to be $\sigma_{c\bar{c}} = 551 \pm 57^{\text{stat}} \pm 195^{\text{sys}}$ μb. Here we have assigned a systematic uncertainty of 15% to the extrapolation to the full rapidity.

The charm cross section obtained here is slightly smaller than that published in Ref. [29] ($567 \pm 57^{\text{stat}} \pm 193^{\text{sys}}$ μb), but agrees well within the systematic uncertainties. The difference comes mainly from the fact that we now subtract the contributions from K_s^0 and J/ψ from the electron spectrum. The cross section is compatible with our previous measurement in the 2002 run [25] ($920 \pm 150^{\text{stat}} \pm 540^{\text{sys}}$ μb) and agrees well with the value derived from the yield of the dielectron continuum [67] ($544 \pm 39^{\text{stat}} \pm 142^{\text{sys}} \pm 200^{\text{model}}$ μb).

The pQCD FONLL calculated cross section (256^{+400}_{-146} μb) is compatible with the data within its uncertainty. Although the data extend to high p_T where the bottom contribution is expected to be dominant, the present analysis does not separate charm and bottom contributions. The bottom cross section predicted by FONLL is $1.87^{+.99}_{-.67}$ μb, which is consistent with previous PHENIX $p + p$ collision results from electron-hadron charge correlations [82] ($3.2^{+1.2+1.4}_{-1.1-1.3}$ μb) and from dielectron-continuum mass distributions [67] ($3.9 \pm 2.5^{+3}_{-2}$ μb).

Total charm yields in Au + Au in various centrality bins are evaluated in a similar procedure. For each centrality bin, the heavy-flavor electron spectrum is integrated for $p_T > 0.4$ GeV/c to obtain $dN^e/dy|_{p_T>0.4}$. The electron cross section

TABLE VII. Charm cross section per $N + N$ collision in centrality bins [0%–10%, 10%–20%, 20%–40%, 40%–60%, 60%–92%, and Min Bias (MB)] in Au + Au and $p + p$.

Centrality	$\frac{d\sigma^e}{dy}\|_{p_T>0.4}$ (μb)	$\frac{d\sigma^e_{c\bar{c}}}{dy}$ (μb)	$\frac{d\sigma_{c\bar{c}}}{dy}$ (μb)	$\sigma_{c\bar{c}}$ (μb)
0%–10%	$6.50 \pm 0.12 \pm 0.92$	$11.9 \pm 0.2 \pm 2.0$	$134 \pm 2 \pm 27$	$620 \pm 11 \pm 156$
10%–20%	$6.30 \pm 0.13 \pm 0.96$	$11.6 \pm 0.2 \pm 2.1$	$130 \pm 3 \pm 27$	$600 \pm 12 \pm 155$
20%–40%	$6.15 \pm 0.13 \pm 1.07$	$11.3 \pm 0.2 \pm 2.2$	$127 \pm 3 \pm 29$	$586 \pm 12 \pm 159$
40%–60%	$6.64 \pm 0.22 \pm 1.28$	$12.2 \pm 0.4 \pm 2.6$	$137 \pm 5 \pm 33$	$633 \pm 21 \pm 180$
60%–92%	$5.98 \pm 0.42 \pm 1.68$	$11.0 \pm 0.8 \pm 2.4$	$123 \pm 9 \pm 39$	$570 \pm 40 \pm 201$
0%–92% (MB)	$5.96 \pm 0.08 \pm 0.96$	$10.9 \pm 0.2 \pm 2.1$	$123 \pm 2 \pm 27$	$568 \pm 8 \pm 150$
$p + p$	$5.79 \pm 0.59 \pm 1.64$	$10.6 \pm 1.1 \pm 3.2$	$119 \pm 12 \pm 38$	$551 \pm 57 \pm 195$

per $N + N$ collision, $d\sigma^e/dy|_{p_T>0.4}$, is then obtained as

$$\frac{d\sigma^e}{dy}|_{p_T>0.4} = \frac{1}{T_{\mathrm{AA}}} \frac{dN^e}{dy}|_{p_T>0.4}. \tag{30}$$

The cross section is then extrapolated to $p_T = 0$, and the contribution from bottom decays and bottom cascade decays are then subtracted to obtain the electron cross section from charm decay per $N + N$ collision $d\sigma^e_{c\bar{c}}/dy$. Here we assume that $R_{\mathrm{AA}} = 1.0$ for p_T-integrated bottom production. The cross section $d\sigma_{c\bar{c}}/dy$ is obtained using Eq. (29). Finally, the cross section is extrapolated to the full rapidity range using the rapidity distribution of charm from HVQMNR to obtain the total charm cross section $\sigma_{c\bar{c}}$ per binary collision. We use the same correction factors $BR(c \to e)$, $C_{e/D}$, and rapidity distribution as in $p + p$ collisions. Table VII summarizes the charm cross section per binary collision in each Au + Au centrality bin. The charm cross sections per binary collision in Au + Au thus obtained agree well with the $p + p$ cross section for all centrality bins. The data are consistent with the results from our previous measurement in Au + Au collisions in the 2002 run [26] ($622 \pm 57^{\mathrm{stat}} \pm 160^{\mathrm{sys}}$ μb per $N + N$ collision in MB Au + Au collisions).

Figure 37 shows $d\sigma^e_{c\bar{c}}/dy|_{p_T>0.4}$ per binary collision in Au + Au and $p + p$ as a function of N_{coll}. The cross section is more than half ($\simeq$54%) of the total electron cross section from charm decay $d\sigma^e_{c\bar{c}}/dy$. Figure 34 shows that R_{AA} is consistent with unity for $p_T < 1.4$ GeV/c. Thus, the shape of the electron spectrum in Au + Au and $p + p$ is almost independent of N_{coll} in the low-p_T region. This indicates that the fraction of the electron cross section below $p_T < 0.4$ GeV/c is almost independent of N_{coll}.

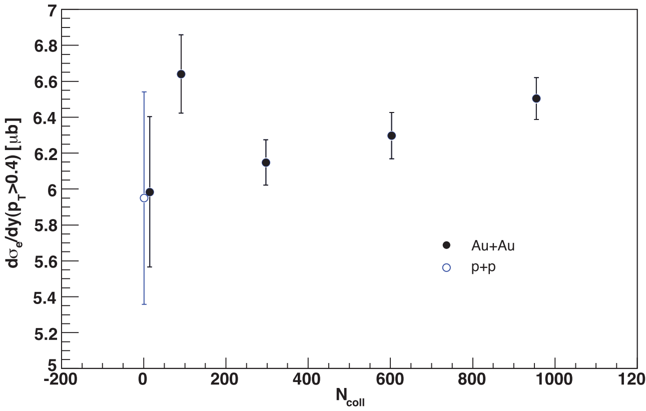

FIG. 37. (Color online) N_{coll} dependence of the charm cross section per binary collision in Au + Au and $p + p$ collisions. The uncertainty bars show the statistical uncertainties only.

F. Heavy-flavor electron $v_2(p_T)$

The heavy-flavor electron v_2 for MB Au + Au collisions is shown in Fig. 38. The vertical lines are the statistical uncertainties and the systematic uncertainties are shown as brackets. The electron v_2 increases up to $p_T \approx 1.5$ GeV/c and then saturates or perhaps decreases. This trend is similar to that of the meson v_2 (π and K). In this p_T range, the dominant contribution to these electrons is from D-meson decay. Therefore, the nonzero electron v_2 indicates that the D meson also has a nonzero v_2.

Figure 39 shows the v_2 for various centrality ranges. The p_T binning used is coarser than that shown in the MB v_2 owing to limited statistics. The v_2 for 60%–92% collisions is not shown because the pion v_2 was not measured by PHENIX separately for that centrality range. At high p_T, the inclusive electron v_2 in the 60%–92% centrality range was measured to be negative by between 2 and 3 standard deviations in the statistical uncertainty, and this accounts for the difference between the MB v_2 and the 0%–60% v_2.

V. DISCUSSION

We have presented measurements of two independent observables, R_{AA} and v_2, which can each be used to discriminate between different mechanisms of heavy-quark interactions in the medium. There are four models which predict both observables simultaneously.

Before the advent of PHENIX single-electron data, it was generally expected that the dominant mechanism for the suppression of heavy quarks in the medium would be gluon radiation, and thus the heavy quarks would not be suppressed as much as the light quarks owing to the dead-cone effect [17]. Predictions from the BDMPS model for radiative energy loss [83] are shown in Fig. 40. In this model the effect of heavy-quark energy loss for $p_T > 2$ GeV/c is considered without any collective effect in the lower p_T region, which gives a lower limit on v_2 at high p_T given by the energy loss and the geometry of the initial almond shape of

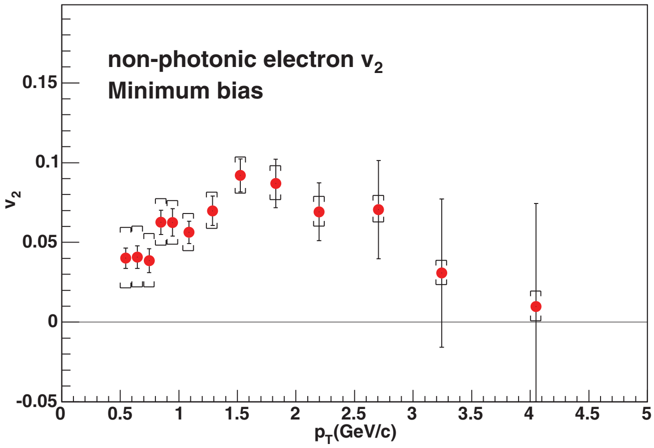

FIG. 38. (Color online) Heavy-flavor electron v_2 as a function of p_T in minimum bias Au + Au collisions at $\sqrt{s_{\rm NN}} = 200$ GeV.

the collision volume. The value of the transport coefficient $\hat{q}$ used to produce the curves in the figure is equal to 14 GeV^2/fm. It is difficult to understand the $R_{\rm AA}$ at high p_T if there is a significant bottom contribution, and the v_2 values are underestimated close to $p_T = 2$ GeV$/c$.

In Ref. [84], it was shown that a Langevin-based heavy-quark transport model can qualitatively explain the large suppression (and azimuthal anisotropy) of electrons from heavy-flavor decays in Au + Au collisions. The model places a heavy quark into a thermal medium, and assumes that the interaction of the heavy quark with the medium can be described by uncorrelated momentum kicks. The interaction in the Langevin model is given exclusively by elastic collisions, which is a good approximation for quarks that are not ultrarelativistic in the center-of-mass frame of the collision. The parameter that is tuned in this model is the heavy-quark diffusion coefficient. The $R_{\rm AA}$ and v_2 calculated from this model are shown in Fig. 41.

While the above Langevin model fails to simultaneously describe $R_{\rm AA}$ and v_2 for a single value of the diffusion coefficient, another Langevin-based model [85,86] is in good agreement with both the suppression and the anisotropy. In this model, the elastic scattering is mediated by resonance excitation of D- and B-meson-like states in the medium. The theoretical evidence for the existence of such resonance states comes from lattice computations. Figure 42 shows the calculation from this model for two different values for the resonance widths.

Gossiaux and Aichelin [87–89] calculated $R_{\rm AA}$ from collisional energy loss in pQCD using a running coupling constant $\alpha_{\rm eff}(t)$ and replacing the Debye mass m_D with a hard thermal loop calculation (with infrared regulator $\mu = \kappa m_D$). Figure 43 shows $R_{\rm AA}$ and v_2 from this model. With a K factor of 1.8, the model finds a value close to the experimental $R_{\rm AA}$

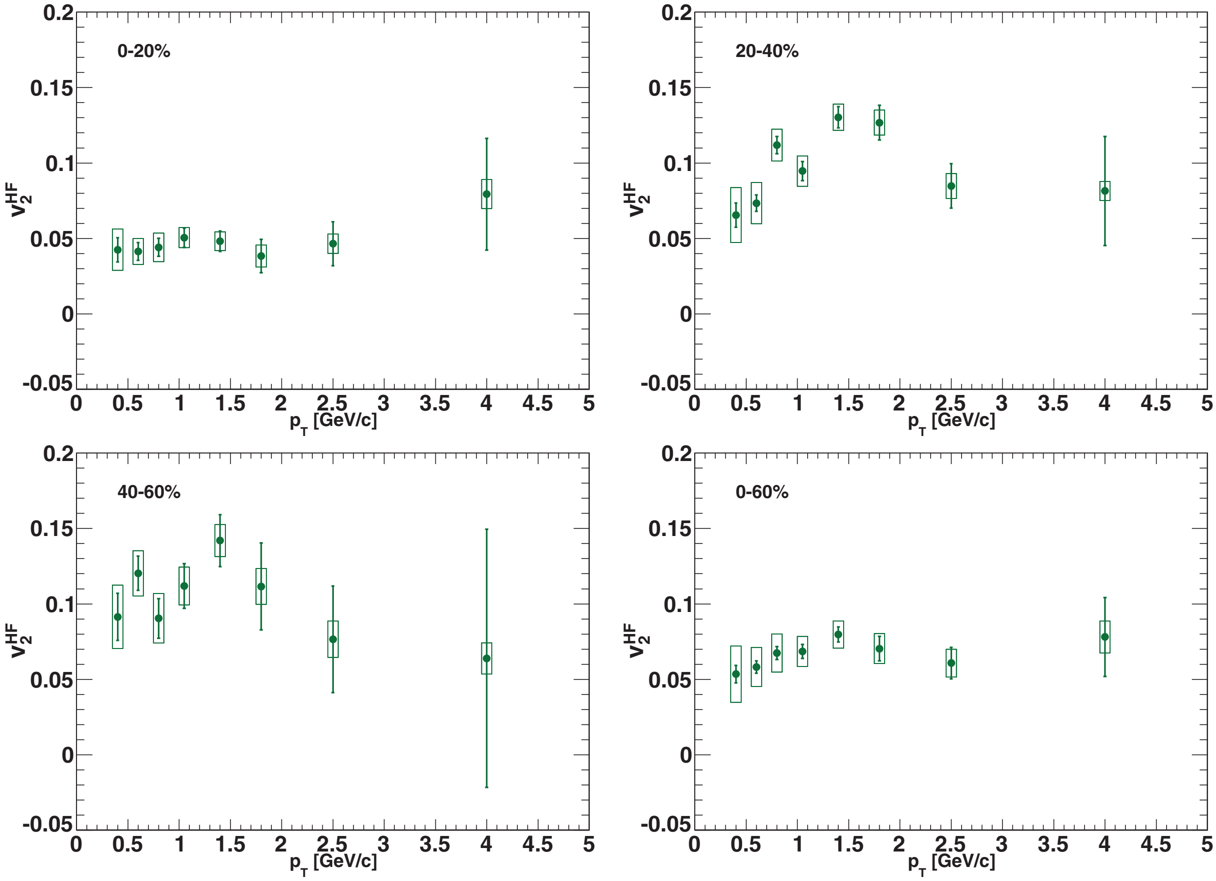

FIG. 39. (Color online) $v_2^{\rm HF}$ for the indicated centralities.

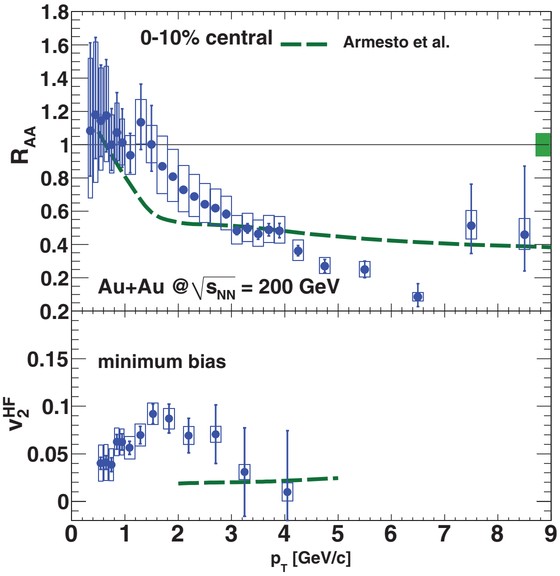

FIG. 40. (Color online) R_{AA} and v_2 from a BDMPS-based calculation from Armesto *et al.* [83].

for all centralities, while leaving room for a possible radiative contribution as well. The v_2 is very sensitive to the interaction time, and a later freeze-out can produce a larger v_2. The curves shown in Fig. 43 reflect the case where heavy flavor hadronizes at the end of the mixed phase.

R_{AA} and v_2 of D mesons have been studied in the framework of the hadron-string-dynamics (HSD) transport model [92]. While at low p_T ($p_T < 4$ GeV/c) the calculated D-meson R_{AA} is consistent with the measured heavy-flavor electron R_{AA}, toward high p_T the (pre)hadronic interactions considered in this model are not sufficient to explain the observed strong suppression of heavy-flavor electrons. Furthermore, the calculated D-meson v_2 is too small compared to the heavy-flavor electron data, which points to strong partonic interactions in the early phase of the collision beyond the (pre)hadronic interactions in HSD.

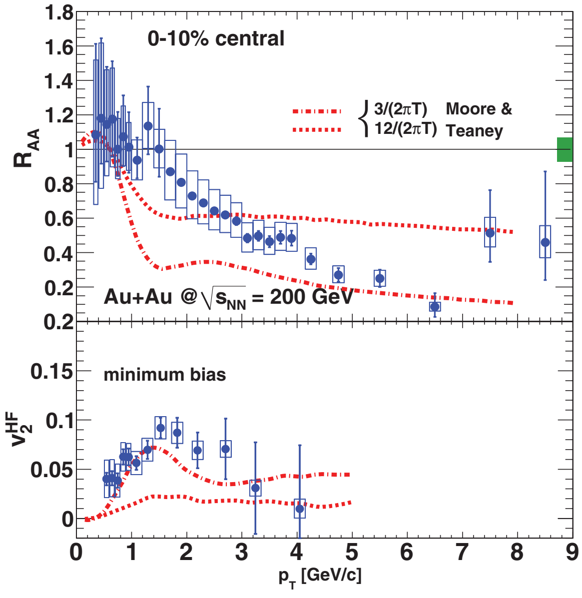

FIG. 41. (Color online) R_{AA} and v_2 from Moore and Teaney for two different values for the diffusion coefficient [84].

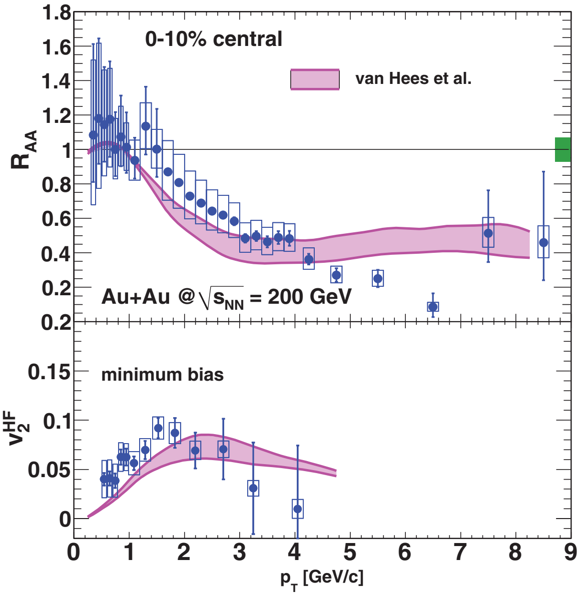

FIG. 42. (Color online) R_{AA} and v_2 from Refs. [85,86] for two different values for the resonance widths used in the calculation.

In addition to the above models which calculate both R_{AA} and v_2 other models calculate only R_{AA} or v_2. For example, Mustafa [93] found that radiative and elastic scattering energy loss for heavy quarks are comparable over a very wide kinematic range accessible at RHIC. Contrary to what was previously thought, collisional energy loss should be taken into account in the calculation of suppression of heavy-flavor mesons in Au + Au collisions. Figure 44 shows the DGLV prediction for suppression when collisional energy loss is taken into account in addition to radiative energy loss [90].

Recently, it has been suggested that collisional dissociation of heavy quarkonia in the quark-gluon plasma [94] may be a possible explanation for suppression of J/ψ production in heavy-ion collisions. Adil and Vitev investigated the pQCD dynamics of open charm and bottom production and, in the framework of the GLV approach extended to composite $q\bar{q}$ systems, derived the medium induced dissociation probability for D and B mesons traveling through dense nuclear matter [91]. They showed that the effective energy loss, which arises from the sequential fragmentation and dissociation of heavy quarks and mesons, is sensitive to the interplay between the formation times of the hadrons and the QGP and the detailed expansion dynamics of hot nuclear matter. Figure 44 shows their result as the lowest band. It will be interesting to see what these calculations predict for v_2 with the same parameters.

Most of the models calculate the heavy-flavor electron production assuming the same chemical composition of charm and bottom hadrons in $p + p$ and Au + Au collisions. As it has been observed for light hadrons [95], one could expect a modification of the charm hadron chemical composition in the most central Au + Au collisions. In particular, an enhancement

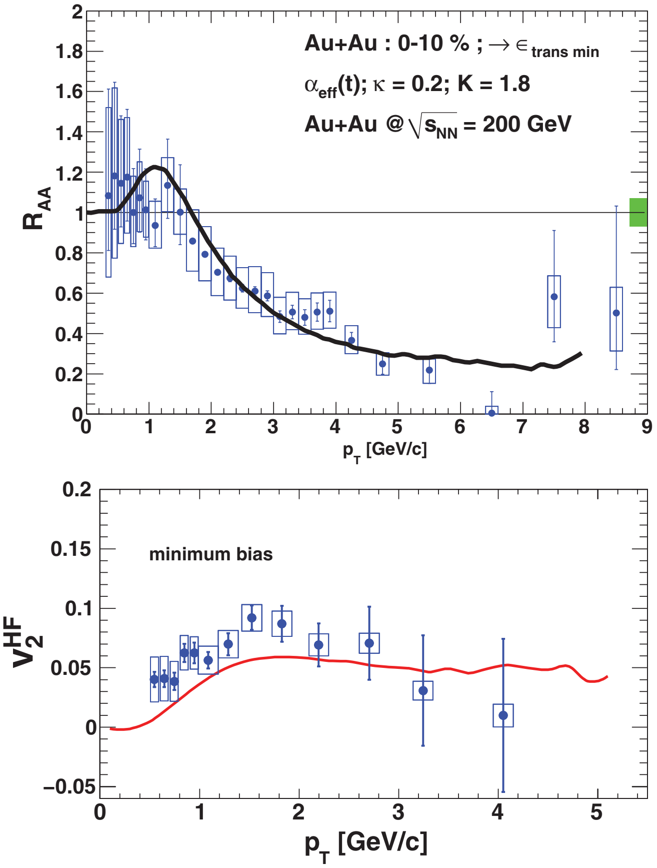

FIG. 43. (Color online) R_{AA} and v_2 from Gossiaux and Aichelin [87–89].

of Λ_c production has been predicted [96]. A Λ_c enhancement leads naturally to a heavy-flavor electron R_{AA} smaller than one owing to a smaller semileptonic decay branching ratio of charm baryons compared to charm mesons and also owing to a softer spectrum of the electrons from the charm baryon decay [97]. A R_{AA} of about 0.65 for electrons from charm hadron decay is predicted when a charm baryon to charm meson ratio in central Au + Au collisions close to one is assumed [98].

Figure 45 shows a set of comparisons of three model calculations with the experimental data on heavy-flavor electron v_2. The model of Greco *et al.* [99] is based on the quark coalescence model with light and charm quark v_2, where the light quark v_2 is estimated from the measured meson v_2 and the same amount of radial flow is assumed for all quark species with the same saturating v_2 for the charm quark as for the light quark. The calculated electron v_2 from the D meson is labeled "Greco *et al.* c flow." However, the line labeled "Greco *et al.* no c flow" assumes zero v_2 for the charm quark, and the predicted v_2 is given only by the light quark v_2 via the quark coalescence mechanism. The model of Zhang *et al.* [100] is a hybrid model starting with HIJING [101] as initial condition, followed by a parton cascade and then a hadron cascade after hadronization using a quark coalescence model. This is based on a multiphase transport model including rescattering of charm quarks with other partons. The line labeled "Zhang *et al.* 10 mb" is the resulting electron v_2 from D-meson decay with the charm quark parton scattering cross section of $\sigma_p = 10$ mb, while the line labeled "Zhang *et al.* 3 mb" corresponds to $\sigma_p = 3$ mb.

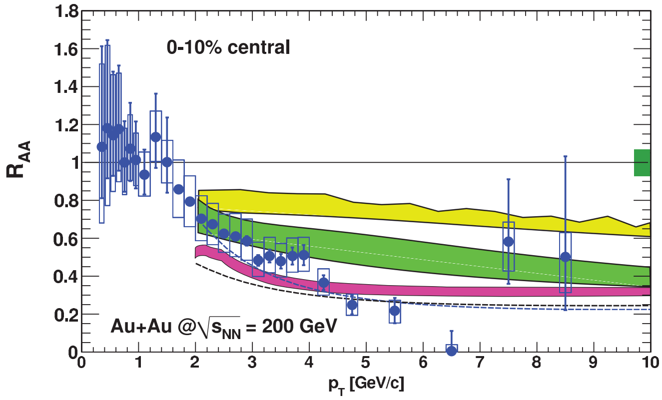

FIG. 44. (Color online) R_{AA} in the 0%–10% centrality class compared with various models. The upper two bands are DGLV [90] calculations for electrons from D and B decays. While the uppermost band considers radiative energy loss only, the middle band takes into account collisional energy loss in addition. The thin dashed curves are DGLV calculations for electrons from D decays only. The lower band is from a collisional dissociation model [91].

In two of the models described above, those of van Hees *et al.* [85,86] and of Moore and Teaney [84], the relevant parameter can be interpreted as a diffusion constant. Because one of the goals of this analysis is to extract information about the bulk properties of the medium, it makes sense to relate this diffusion constant to the viscosity of the medium.

The ratio of shear viscosity η to entropy density s is a key parameter that determines the damping rate in a relativistic system. At temperature T, characteristic damping times τ are of order η/sT [102].

While the apparent success of ideal hydrodynamics in describing particle spectra and elliptic flow patterns at RHIC would imply a vanishing value of η/s, straightforward arguments based on the uncertainty principle suggest that the viscosity for any thermal system must be nonzero [103].

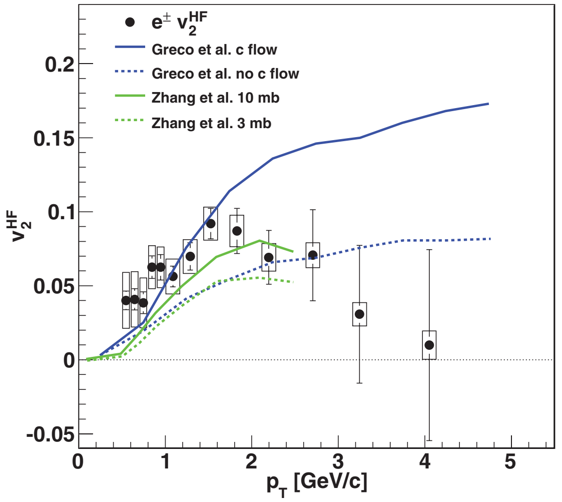

FIG. 45. (Color online) Theory comparison of experimental v_2 data with the models of Greco *et al.* [99] and Zhang *et al.* [100].

This observation was extended by Kovtun, Son, and Starinets (KSS) [14], who demonstrated that conformal field theories with gravity duals have a ratio of viscosity η to entropy density s of $1/4\pi$ (in natural units). KSS conjectured that this value is a bound for any relativistic thermal field theory, that is, $\eta/s \geqslant 1/4\pi$.

The results presented in Sec. IV for $R_{AA}(p_T^e)$ and $v_2(p_T^e)$ show that heavy quarks lose energy in the medium, while acquiring a substantial component of the medium's collective flow. Both of these effects may be regarded as the damping of the initial nonequilibrium dynamics of the "external" heavy quark by the medium. The simultaneous description of these phenomena by the model of van Hees *et al.* provides a straightforward, albeit indirect, method to infer the ratio of viscosity to entropy density.

The resonance model employed in Ref. [85] leads to an estimate for the heavy-quark spatial diffusion constant $D_s \sim (4\text{–}6)/2\pi T$ for temperatures T in the range $0.2\ \text{GeV} < T < 0.4\ \text{GeV}$ (see also Fig. 23 of Ref. [104]). Moore and Teaney [84] perform a perturbative calculation of this quantity and find that for a medium with three light flavors the ratio of D_s to the hydrodynamic diffusion constant $\eta/(\epsilon + p)$ for the bulk (ϵ is the energy density and p the pressure of the medium) has a value of ~6 roughly independent of the coupling strength $\sim m_D/T$, where m_D is the Debye mass. They argue that the weak variation with coupling strength is to be expected in this *ratio* of transport coefficients, making it plausible that it remains near 6 in the strongly coupled regime. In this case, and approximating the thermodynamic identity $\epsilon + p = Ts + \mu_B n_B \approx Ts$ appropriate for the baryon-free central region, one readily finds $\eta/s \sim (1.33\text{–}2)/4\pi$, that is, a value near the KSS bound and consistent with other estimates for the RHIC plasma based on flow [105,106], fluctuations [107], entropy production [108], and detailed hydrodynamic calculations [109,110].

It should be noted that these various estimates are based on observables of the "bulk" medium, in flavor channels dominated by u, d, and s quarks, while the result presented here relies explicitly on the coupling of heavy flavor to the medium. The consistency of the derived value of η/s supports both the strong coupling of heavy flavor to the medium and the low value of η/s for the RHIC plasma.

VI. SUMMARY AND CONCLUSIONS

This article has detailed the measurement of the yield of single electrons from semileptonic decays of heavy-flavor mesons at midrapidity in $p + p$ and Au + Au collisions at $\sqrt{s_{NN}} = 200$ GeV, as well as the azimuthal anisotropy parameter v_2 of such electrons in Au + Au collisions. The unexpectedly large suppression of heavy-flavor electrons in Au + Au collisions relative to those from $p + p$ collisions and the large v_2 of heavy-flavor electrons has generated much theoretical work. In a system as complicated as this medium, confidence from any given model depends on its ability to describe multiple observables simultaneously. In the coming years, PHENIX will measure the yields and flow of bottom and charm mesons separately, which will further constrain the interpretation of the data. If indeed even the bottom quarks exhibit strong collective motion, then our understanding of the underlying mechanism of heavy-quark interaction in the medium will need to be significantly revised.

ACKNOWLEDGMENTS

We thank the staff of the Collider-Accelerator and Physics Departments at Brookhaven National Laboratory and the staff of the other PHENIX participating institutions for their vital contributions. We acknowledge support from the Office of Nuclear Physics in the Office of Science of the Department of Energy, the National Science Foundation, a sponsored research grant from Renaissance Technologies LLC, Abilene Christian University Research Council, Research Foundation of SUNY, and Dean of the College of Arts and Sciences, Vanderbilt University (USA); Ministry of Education, Culture, Sports, Science, and Technology and the Japan Society for the Promotion of Science (Japan); Conselho Nacional de Desenvolvimento Científico e Tecnológico and Fundação de Amparo à Pesquisa do Estado de São Paulo (Brazil); Natural Science Foundation of China (People's Republic of China); Ministry of Education, Youth and Sports (Czech Republic); Centre National de la Recherche Scientifique, Commissariat à l'Énergie Atomique, and Institut National de Physique Nucléaire et de Physique des Particules (France); Ministry of Industry, Science and Tekhnologies, Bundesministerium für Bildung und Forschung, Deutscher Akademischer Austausch Dienst, and Alexander von Humboldt Stiftung (Germany); Hungarian National Science Fund, OTKA (Hungary); Department of Atomic Energy (India); Israel Science Foundation (Israel); Korea Research Foundation and Korea Science and Engineering Foundation (Korea); Ministry of Education and Science, Russia Academy of Sciences, Federal Agency of Atomic Energy (Russia); VR and the Wallenberg Foundation (Sweden); the USA Civilian Research and Development Foundation for the Independent States of the Former Soviet Union; the US-Hungarian Fulbright Foundation for Educational Exchange; and the US-Israel Binational Science Foundation.

APPENDIX: DATA TABLES

Data are presented in this Appendix for MB events (0%–92%) and for each centrality class (0%–10%, 10%–20%, 20%–40%, 40%–60%, and 60%–92%) for Au + Au collisions at $\sqrt{s_{NN}} = 200$ GeV at midrapidity. Tables VIII–X tabulate the differential invariant yield of heavy-flavor electrons. Tables XI–XIII give the nuclear modification factor R_{AA} of heavy-flavor electrons. Table XIV gives the p_T^e-integrated nuclear modification factors R_{AA}. Table XV shows v_2 for heavy-flavor electrons. Table XVI gives the differential invariant cross section of heavy-flavor electrons for $p + p$ collisions at $\sqrt{s} = 200$ GeV.

TABLE VIII. Differential invariant yield of electrons $[(N_{e^+} + N_{e^-})/2]$ from heavy-flavor decays for (upper, minimum bias) 0%–92% and (lower) 0%–10% centrality classes. The p_T^e is in units of GeV/c. The yield and corresponding uncertainties are in units of (GeV/c)$^{-2}$.

Centrality	p_T^e	Invariant yield	Stat. error (+)	Stat. error (−)	Sys. error (+)	Sys. error (−)
0%–92%	0.35	7.96×10^{-2}	2.51×10^{-3}	2.47×10^{-3}	2.03×10^{-2}	2.01×10^{-2}
	0.45	4.03×10^{-2}	1.09×10^{-3}	1.08×10^{-3}	8.13×10^{-3}	8.03×10^{-3}
	0.55	2.24×10^{-2}	5.66×10^{-4}	5.59×10^{-4}	3.86×10^{-3}	3.81×10^{-3}
	0.65	1.30×10^{-2}	3.44×10^{-4}	3.41×10^{-4}	2.05×10^{-3}	2.03×10^{-3}
	0.75	7.96×10^{-3}	2.12×10^{-4}	2.10×10^{-4}	1.10×10^{-3}	1.09×10^{-3}
	0.85	5.33×10^{-3}	1.42×10^{-4}	1.41×10^{-4}	6.44×10^{-4}	6.38×10^{-4}
	0.95	3.47×10^{-3}	1.00×10^{-4}	9.93×10^{-5}	3.93×10^{-4}	3.90×10^{-4}
	1.1	1.95×10^{-3}	4.56×10^{-5}	4.43×10^{-5}	2.07×10^{-4}	2.01×10^{-4}
	1.3	9.51×10^{-4}	1.14×10^{-5}	1.12×10^{-5}	1.11×10^{-4}	1.08×10^{-4}
	1.5	4.45×10^{-4}	5.08×10^{-6}	4.96×10^{-6}	5.29×10^{-5}	5.17×10^{-5}
	1.7	1.98×10^{-4}	1.77×10^{-6}	1.77×10^{-6}	2.98×10^{-5}	2.99×10^{-5}
	1.9	1.00×10^{-4}	1.00×10^{-6}	1.00×10^{-6}	1.46×10^{-5}	1.45×10^{-5}
	2.1	5.21×10^{-5}	6.16×10^{-7}	6.16×10^{-7}	7.42×10^{-6}	7.42×10^{-6}
	2.3	2.93×10^{-5}	4.08×10^{-7}	4.08×10^{-7}	4.03×10^{-6}	4.03×10^{-6}
	2.5	1.66×10^{-5}	2.78×10^{-7}	2.78×10^{-7}	2.25×10^{-6}	2.25×10^{-6}
	2.7	9.63×10^{-6}	1.97×10^{-7}	1.97×10^{-7}	1.30×10^{-6}	1.30×10^{-6}
	2.9	5.79×10^{-6}	1.44×10^{-7}	1.43×10^{-7}	7.73×10^{-7}	7.73×10^{-7}
	3.1	3.61×10^{-6}	1.08×10^{-7}	1.08×10^{-7}	4.76×10^{-7}	4.77×10^{-7}
	3.3	2.25×10^{-6}	8.23×10^{-8}	8.14×10^{-8}	3.00×10^{-7}	3.00×10^{-7}
	3.5	1.47×10^{-6}	6.42×10^{-8}	6.33×10^{-8}	1.95×10^{-7}	1.95×10^{-7}
	3.7	1.13×10^{-6}	5.28×10^{-8}	5.20×10^{-8}	1.40×10^{-7}	1.40×10^{-7}
	3.9	6.24×10^{-7}	4.01×10^{-8}	3.93×10^{-8}	8.54×10^{-8}	8.64×10^{-8}
	4.2	3.24×10^{-7}	1.75×10^{-8}	1.72×10^{-8}	4.48×10^{-8}	4.61×10^{-8}
	4.8	1.16×10^{-7}	1.05×10^{-8}	1.03×10^{-8}	1.80×10^{-8}	2.09×10^{-8}
	5.5	2.87×10^{-8}	4.62×10^{-9}	4.42×10^{-9}	5.80×10^{-9}	9.98×10^{-9}
	6.5	8.40×10^{-9}	2.42×10^{-9}	2.07×10^{-9}	1.69×10^{-9}	3.92×10^{-9}
	7.5	5.04×10^{-9}	2.07×10^{-9}	1.29×10^{-9}	7.60×10^{-10}	1.78×10^{-9}
	8.5	1.66×10^{-9}	1.29×10^{-9}	6.17×10^{-10}	3.67×10^{-10}	8.22×10^{-10}
0%–10%	0.35	3.35×10^{-1}	1.64×10^{-2}	1.61×10^{-2}	6.70×10^{-2}	6.60×10^{-2}
	0.45	1.62×10^{-1}	7.05×10^{-3}	6.95×10^{-3}	2.73×10^{-2}	2.69×10^{-2}
	0.55	8.75×10^{-2}	3.59×10^{-3}	3.55×10^{-3}	1.30×10^{-2}	1.28×10^{-2}
	0.65	4.83×10^{-2}	2.15×10^{-3}	2.12×10^{-3}	6.87×10^{-3}	6.79×10^{-3}
	0.75	2.96×10^{-2}	1.31×10^{-3}	1.30×10^{-3}	3.74×10^{-3}	3.70×10^{-3}
	0.85	1.83×10^{-2}	8.65×10^{-4}	8.57×10^{-4}	2.17×10^{-3}	2.14×10^{-3}
	0.95	1.29×10^{-2}	6.13×10^{-4}	6.07×10^{-4}	1.37×10^{-3}	1.36×10^{-3}
	1.1	6.78×10^{-3}	2.74×10^{-4}	2.66×10^{-4}	7.05×10^{-4}	6.83×10^{-4}
	1.3	3.25×10^{-3}	7.08×10^{-5}	6.89×10^{-5}	4.01×10^{-4}	3.90×10^{-4}
	1.5	1.50×10^{-3}	3.09×10^{-5}	3.02×10^{-5}	1.91×10^{-4}	1.86×10^{-4}
	1.7	6.51×10^{-4}	1.05×10^{-5}	1.05×10^{-5}	9.80×10^{-5}	9.80×10^{-5}
	1.9	3.25×10^{-4}	5.84×10^{-6}	5.84×10^{-6}	4.70×10^{-5}	4.69×10^{-5}
	2.1	1.62×10^{-4}	3.51×10^{-6}	3.51×10^{-6}	2.34×10^{-5}	2.34×10^{-5}
	2.3	9.04×10^{-5}	2.30×10^{-6}	2.30×10^{-6}	1.25×10^{-5}	1.26×10^{-5}
	2.5	5.04×10^{-5}	1.55×10^{-6}	1.55×10^{-6}	6.91×10^{-6}	6.89×10^{-6}
	2.7	3.04×10^{-5}	1.11×10^{-6}	1.11×10^{-6}	4.06×10^{-6}	4.06×10^{-6}
	2.9	1.85×10^{-5}	8.02×10^{-7}	8.02×10^{-7}	2.43×10^{-6}	2.43×10^{-6}
	3.1	9.89×10^{-6}	5.84×10^{-7}	5.79×10^{-7}	1.38×10^{-6}	1.38×10^{-6}
	3.3	6.84×10^{-6}	4.53×10^{-7}	4.48×10^{-7}	9.14×10^{-7}	9.16×10^{-7}
	3.5	4.36×10^{-6}	3.52×10^{-7}	3.48×10^{-7}	5.87×10^{-7}	5.89×10^{-7}
	3.7	3.15×10^{-6}	2.82×10^{-7}	2.78×10^{-7}	4.08×10^{-7}	4.09×10^{-7}
	3.9	2.21×10^{-6}	2.32×10^{-7}	2.28×10^{-7}	2.84×10^{-7}	2.85×10^{-7}
	4.2	8.70×10^{-7}	9.32×10^{-8}	9.19×10^{-8}	1.28×10^{-7}	1.30×10^{-7}
	4.8	2.67×10^{-7}	5.51×10^{-8}	5.39×10^{-8}	4.91×10^{-8}	5.23×10^{-8}
	5.5	8.01×10^{-8}	2.50×10^{-8}	2.41×10^{-8}	1.74×10^{-8}	2.26×10^{-8}
	6.5	5.97×10^{-10}	1.11×10^{-8}	8.26×10^{-9}	3.49×10^{-9}	9.12×10^{-9}
	7.5	2.03×10^{-8}	1.15×10^{-8}	7.78×10^{-9}	2.72×10^{-9}	5.02×10^{-9}
	8.5	6.60×10^{-9}	6.97×10^{-9}	3.70×10^{-9}	1.28×10^{-9}	2.35×10^{-9}

TABLE IX. Differential invariant yield of electrons $[(N_{e^+} + N_{e^-})/2]$ from heavy-flavor decays for (upper) 10%–20% and (lower) 20%–40% centrality classes. The p_T^e is in units of GeV$/c$. The yield and corresponding uncertainties are in units of (GeV$/c)^{-2}$.

Centrality	p_T^e	Invariant yield	Stat. error (+)	Stat. error (−)	Sys. error (+)	Sys. error (−)
10%–20%	0.35	1.90×10^{-1}	1.11×10^{-2}	1.09×10^{-2}	4.48×10^{-2}	4.42×10^{-2}
	0.45	9.11×10^{-2}	4.81×10^{-3}	4.75×10^{-3}	1.79×10^{-2}	1.77×10^{-2}
	0.55	5.29×10^{-2}	2.52×10^{-3}	2.49×10^{-3}	8.57×10^{-3}	8.48×10^{-3}
	0.65	2.92×10^{-2}	1.53×10^{-3}	1.51×10^{-3}	4.55×10^{-3}	4.50×10^{-3}
	0.75	1.88×10^{-2}	9.51×10^{-4}	9.42×10^{-4}	2.47×10^{-3}	2.45×10^{-3}
	0.85	1.29×10^{-2}	6.42×10^{-4}	6.36×10^{-4}	1.47×10^{-3}	1.46×10^{-3}
	0.95	7.93×10^{-3}	4.50×10^{-4}	4.46×10^{-4}	8.77×10^{-4}	8.70×10^{-4}
	1.1	4.47×10^{-3}	2.07×10^{-4}	2.01×10^{-4}	4.69×10^{-4}	4.55×10^{-4}
	1.3	2.20×10^{-3}	5.02×10^{-5}	4.90×10^{-5}	2.50×10^{-4}	2.44×10^{-4}
	1.5	1.01×10^{-3}	2.24×10^{-5}	2.19×10^{-5}	1.16×10^{-4}	1.13×10^{-4}
	1.7	4.62×10^{-4}	7.98×10^{-6}	7.98×10^{-6}	6.73×10^{-5}	6.75×10^{-5}
	1.9	2.31×10^{-4}	4.54×10^{-6}	4.54×10^{-6}	3.27×10^{-5}	3.27×10^{-5}
	2.1	1.24×10^{-4}	2.81×10^{-6}	2.81×10^{-6}	1.68×10^{-5}	1.68×10^{-5}
	2.3	7.15×10^{-5}	1.89×10^{-6}	1.89×10^{-6}	9.25×10^{-6}	9.24×10^{-6}
	2.5	3.91×10^{-5}	1.27×10^{-6}	1.27×10^{-6}	5.04×10^{-6}	5.04×10^{-6}
	2.7	2.20×10^{-5}	8.92×10^{-7}	8.92×10^{-7}	2.86×10^{-6}	2.86×10^{-6}
	2.9	1.27×10^{-5}	6.44×10^{-7}	6.44×10^{-7}	1.67×10^{-6}	1.67×10^{-6}
	3.1	8.45×10^{-6}	4.96×10^{-7}	4.91×10^{-7}	1.07×10^{-6}	1.06×10^{-6}
	3.3	4.94×10^{-6}	3.69×10^{-7}	3.65×10^{-7}	6.41×10^{-7}	6.41×10^{-7}
	3.5	3.55×10^{-6}	2.94×10^{-7}	2.90×10^{-7}	4.39×10^{-7}	4.40×10^{-7}
	3.7	2.82×10^{-6}	2.48×10^{-7}	2.44×10^{-7}	3.25×10^{-7}	3.25×10^{-7}
	3.9	1.16×10^{-6}	1.71×10^{-7}	1.68×10^{-7}	1.68×10^{-7}	1.68×10^{-7}
	4.2	8.33×10^{-7}	8.13×10^{-8}	8.01×10^{-8}	1.05×10^{-7}	1.07×10^{-7}
	4.8	2.63×10^{-7}	4.81×10^{-8}	4.70×10^{-8}	3.94×10^{-8}	4.05×10^{-8}
	5.5	6.75×10^{-8}	2.10×10^{-8}	2.02×10^{-8}	1.28×10^{-8}	1.66×10^{-8}
	6.5	3.20×10^{-8}	1.20×10^{-8}	1.13×10^{-8}	4.59×10^{-9}	7.61×10^{-9}
	7.5	2.21×10^{-8}	1.13×10^{-8}	7.40×10^{-9}	2.42×10^{-9}	3.84×10^{-9}
	8.5	6.68×10^{-9}	6.78×10^{-9}	3.30×10^{-9}	1.09×10^{-9}	1.79×10^{-9}
20%–40%	0.35	7.35×10^{-2}	5.15×10^{-3}	5.09×10^{-3}	2.48×10^{-2}	2.45×10^{-2}
	0.45	4.19×10^{-2}	2.30×10^{-3}	2.28×10^{-3}	9.85×10^{-3}	9.74×10^{-3}
	0.55	2.25×10^{-2}	1.20×10^{-3}	1.19×10^{-3}	4.66×10^{-3}	4.61×10^{-3}
	0.65	1.55×10^{-2}	7.55×10^{-4}	7.47×10^{-4}	2.50×10^{-3}	2.48×10^{-3}
	0.75	8.93×10^{-3}	4.63×10^{-4}	4.59×10^{-4}	1.33×10^{-3}	1.31×10^{-3}
	0.85	6.50×10^{-3}	3.16×10^{-4}	3.13×10^{-4}	7.83×10^{-4}	7.76×10^{-4}
	0.95	3.79×10^{-3}	2.21×10^{-4}	2.19×10^{-4}	4.66×10^{-4}	4.63×10^{-4}
	1.1	2.38×10^{-3}	1.03×10^{-4}	9.98×10^{-5}	2.51×10^{-4}	2.44×10^{-4}
	1.3	1.15×10^{-3}	2.77×10^{-5}	2.70×10^{-5}	1.26×10^{-4}	1.23×10^{-4}
	1.5	5.45×10^{-4}	1.24×10^{-5}	1.21×10^{-5}	6.07×10^{-5}	5.94×10^{-5}
	1.7	2.47×10^{-4}	4.27×10^{-6}	4.27×10^{-6}	3.76×10^{-5}	3.76×10^{-5}
	1.9	1.28×10^{-4}	2.42×10^{-6}	2.42×10^{-6}	1.87×10^{-5}	1.85×10^{-5}
	2.1	6.75×10^{-5}	1.49×10^{-6}	1.49×10^{-6}	9.60×10^{-6}	9.61×10^{-6}
	2.3	3.72×10^{-5}	9.78×10^{-7}	9.78×10^{-7}	5.15×10^{-6}	5.15×10^{-6}
	2.5	2.17×10^{-5}	6.70×10^{-7}	6.70×10^{-7}	2.93×10^{-6}	2.93×10^{-6}
	2.7	1.27×10^{-5}	4.73×10^{-7}	4.73×10^{-7}	1.70×10^{-6}	1.70×10^{-6}
	2.9	7.94×10^{-6}	3.50×10^{-7}	3.50×10^{-7}	1.04×10^{-6}	1.03×10^{-6}
	3.1	5.02×10^{-6}	2.64×10^{-7}	2.64×10^{-7}	6.43×10^{-7}	6.44×10^{-7}
	3.3	3.18×10^{-6}	2.02×10^{-7}	2.00×10^{-7}	4.10×10^{-7}	4.10×10^{-7}
	3.5	1.93×10^{-6}	1.54×10^{-7}	1.52×10^{-7}	2.54×10^{-7}	2.55×10^{-7}
	3.7	1.45×10^{-6}	1.26×10^{-7}	1.25×10^{-7}	1.80×10^{-7}	1.81×10^{-7}
	3.9	7.96×10^{-7}	9.42×10^{-8}	9.26×10^{-8}	1.10×10^{-7}	1.12×10^{-7}
	4.2	4.27×10^{-7}	4.21×10^{-8}	4.15×10^{-8}	5.91×10^{-8}	6.08×10^{-8}
	4.8	1.73×10^{-7}	2.57×10^{-8}	2.52×10^{-8}	2.48×10^{-8}	3.21×10^{-8}
	5.5	4.05×10^{-8}	1.11×10^{-8}	1.07×10^{-8}	7.73×10^{-9}	1.64×10^{-8}
	6.5	1.34×10^{-8}	5.75×10^{-9}	5.45×10^{-9}	2.34×10^{-9}	6.04×10^{-9}
	7.5	2.23×10^{-9}	4.02×10^{-9}	2.32×10^{-9}	6.45×10^{-10}	2.41×10^{-9}
	8.5	1.81×10^{-9}	2.85×10^{-9}	1.36×10^{-9}	4.12×10^{-10}	1.13×10^{-9}

TABLE X. Differential invariant yield of electrons $[(N_{e^+} + N_{e^-})/2]$ from heavy-flavor decays for (upper) 40%–60% and (lower) 60%–92% centrality classes. The p_T^e is in units of GeV/c. The yield and corresponding uncertainties are in units of (GeV/c)$^{-2}$

Centrality	p_T^e	Invariant yield	Stat. error (+)	Stat. error (−)	Sys. error (+)	Sys. error (−)
40%–60%	0.35	2.14×10^{-2}	2.67×10^{-3}	2.63×10^{-3}	9.42×10^{-3}	9.31×10^{-3}
	0.45	1.36×10^{-2}	1.19×10^{-3}	1.18×10^{-3}	3.69×10^{-3}	3.65×10^{-3}
	0.55	8.48×10^{-3}	6.44×10^{-4}	6.38×10^{-4}	1.72×10^{-3}	1.70×10^{-3}
	0.65	4.30×10^{-3}	4.00×10^{-4}	3.96×10^{-4}	9.02×10^{-4}	8.94×10^{-4}
	0.75	2.78×10^{-3}	2.51×10^{-4}	2.49×10^{-4}	4.73×10^{-4}	4.69×10^{-4}
	0.85	2.03×10^{-3}	1.71×10^{-4}	1.70×10^{-4}	2.74×10^{-4}	2.72×10^{-4}
	0.95	1.41×10^{-3}	1.23×10^{-4}	1.22×10^{-4}	1.68×10^{-4}	1.67×10^{-4}
	1.1	7.48×10^{-4}	5.70×10^{-5}	5.55×10^{-5}	8.65×10^{-5}	8.42×10^{-5}
	1.3	4.05×10^{-4}	1.05×10^{-5}	1.03×10^{-5}	4.23×10^{-5}	4.13×10^{-5}
	1.5	1.98×10^{-4}	5.00×10^{-6}	4.90×10^{-6}	2.10×10^{-5}	2.06×10^{-5}
	1.7	8.54×10^{-5}	2.01×10^{-6}	2.01×10^{-6}	1.33×10^{-5}	1.33×10^{-5}
	1.9	4.40×10^{-5}	1.22×10^{-6}	1.22×10^{-6}	6.67×10^{-6}	6.67×10^{-6}
	2.1	2.48×10^{-5}	7.91×10^{-7}	7.91×10^{-7}	3.56×10^{-6}	3.55×10^{-6}
	2.3	1.39×10^{-5}	5.45×10^{-7}	5.45×10^{-7}	1.96×10^{-6}	1.96×10^{-6}
	2.5	8.39×10^{-6}	3.85×10^{-7}	3.85×10^{-7}	1.13×10^{-6}	1.14×10^{-6}
	2.7	4.47×10^{-6}	2.72×10^{-7}	2.72×10^{-7}	6.38×10^{-7}	6.40×10^{-7}
	2.9	2.53×10^{-6}	1.98×10^{-7}	1.96×10^{-7}	3.70×10^{-7}	3.71×10^{-7}
	3.1	1.98×10^{-6}	1.60×10^{-7}	1.58×10^{-7}	2.55×10^{-7}	2.56×10^{-7}
	3.3	1.06×10^{-6}	1.18×10^{-7}	1.16×10^{-7}	1.50×10^{-7}	1.50×10^{-7}
	3.5	7.27×10^{-7}	9.34×10^{-8}	9.17×10^{-8}	9.95×10^{-8}	9.95×10^{-8}
	3.7	6.12×10^{-7}	7.86×10^{-8}	7.70×10^{-8}	7.46×10^{-8}	7.47×10^{-8}
	3.9	3.15×10^{-7}	5.82×10^{-8}	5.67×10^{-8}	4.40×10^{-8}	4.47×10^{-8}
	4.2	1.82×10^{-7}	2.62×10^{-8}	2.57×10^{-8}	2.42×10^{-8}	2.63×10^{-8}
	4.8	9.48×10^{-8}	1.76×10^{-8}	1.71×10^{-8}	1.18×10^{-8}	1.41×10^{-8}
	5.5	1.83×10^{-8}	7.04×10^{-9}	6.71×10^{-9}	3.25×10^{-9}	7.51×10^{-9}
	6.5	7.98×10^{-9}	4.37×10^{-9}	3.21×10^{-9}	1.11×10^{-9}	2.78×10^{-9}
	7.5	4.97×10^{-10}	2.74×10^{-9}	1.13×10^{-9}	2.42×10^{-10}	1.04×10^{-9}
60%–92%	0.35	5.28×10^{-3}	8.56×10^{-4}	8.47×10^{-4}	2.16×10^{-3}	2.14×10^{-3}
	0.45	1.82×10^{-3}	3.68×10^{-4}	3.65×10^{-4}	8.06×10^{-4}	7.97×10^{-4}
	0.55	1.18×10^{-3}	2.01×10^{-4}	1.99×10^{-4}	3.72×10^{-4}	3.69×10^{-4}
	0.65	7.89×10^{-4}	1.26×10^{-4}	1.25×10^{-4}	1.93×10^{-4}	1.91×10^{-4}
	0.75	4.27×10^{-4}	7.87×10^{-5}	7.81×10^{-5}	9.85×10^{-5}	9.77×10^{-5}
	0.85	2.30×10^{-4}	5.28×10^{-5}	5.24×10^{-5}	5.38×10^{-5}	5.34×10^{-5}
	0.95	1.99×10^{-4}	3.81×10^{-5}	3.78×10^{-5}	3.29×10^{-5}	3.27×10^{-5}
	1.1	1.27×10^{-4}	1.78×10^{-5}	1.74×10^{-5}	1.74×10^{-5}	1.69×10^{-5}
	1.3	6.15×10^{-5}	2.08×10^{-6}	2.03×10^{-6}	1.04×10^{-5}	1.01×10^{-5}
	1.5	2.99×10^{-5}	1.08×10^{-6}	1.06×10^{-6}	5.21×10^{-6}	5.10×10^{-6}
	1.7	1.33×10^{-5}	5.43×10^{-7}	5.43×10^{-7}	2.27×10^{-6}	2.27×10^{-6}
	1.9	6.62×10^{-6}	3.44×10^{-7}	3.44×10^{-7}	1.14×10^{-6}	1.14×10^{-6}
	2.1	2.75×10^{-6}	2.18×10^{-7}	2.18×10^{-7}	5.54×10^{-7}	5.54×10^{-7}
	2.3	1.68×10^{-6}	1.57×10^{-7}	1.56×10^{-7}	3.16×10^{-7}	3.16×10^{-7}
	2.5	1.09×10^{-6}	1.15×10^{-7}	1.14×10^{-7}	1.89×10^{-7}	1.89×10^{-7}
	2.7	5.71×10^{-7}	8.19×10^{-8}	8.06×10^{-8}	1.08×10^{-7}	1.08×10^{-7}
	2.9	3.33×10^{-7}	6.08×10^{-8}	5.97×10^{-8}	6.46×10^{-8}	6.46×10^{-8}
	3.1	2.75×10^{-7}	4.95×10^{-8}	4.84×10^{-8}	4.40×10^{-8}	4.42×10^{-8}
	3.3	1.29×10^{-7}	3.62×10^{-8}	3.52×10^{-8}	2.58×10^{-8}	2.58×10^{-8}
	3.5	1.02×10^{-7}	2.94×10^{-8}	2.84×10^{-8}	1.78×10^{-8}	1.79×10^{-8}
	3.7	9.29×10^{-8}	2.52×10^{-8}	2.43×10^{-8}	1.33×10^{-8}	1.34×10^{-8}
	3.9	4.68×10^{-8}	1.92×10^{-8}	1.84×10^{-8}	8.09×10^{-9}	8.41×10^{-9}
	4.2	1.97×10^{-8}	7.93×10^{-9}	7.63×10^{-9}	3.85×10^{-9}	4.17×10^{-9}
	4.8	6.30×10^{-10}	4.10×10^{-9}	3.84×10^{-9}	1.17×10^{-9}	2.14×10^{-9}
	6.5	6.14×10^{-10}	1.48×10^{-9}	7.82×10^{-10}	1.60×10^{-10}	5.31×10^{-10}

TABLE XI. $R_{\mathrm{AA}}(p_T^e)$ for (upper, minimum bias) 0%–92% and (lower) 0%–10% centrality classes. The p_T^e is in units of GeV/c. The yield and corresponding uncertainties are in units of (GeV/c)$^{-2}$.

Centrality	p_T^e	R_{AA}	Stat. error (+)	Stat. error (−)	Sys. error (+)	Sys. error (−)
0%–92%	0.35	9.53×10^{-1}	4.65×10^{-1}	2.37×10^{-1}	3.01×10^{-1}	2.62×10^{-1}
	0.45	1.08×10^{0}	4.25×10^{-1}	2.40×10^{-1}	3.42×10^{-1}	3.09×10^{-1}
	0.55	1.09×10^{0}	3.17×10^{-1}	2.01×10^{-1}	2.57×10^{-1}	2.34×10^{-1}
	0.65	1.17×10^{0}	3.33×10^{-1}	2.14×10^{-1}	2.95×10^{-1}	2.77×10^{-1}
	0.75	9.97×10^{-1}	2.13×10^{-1}	1.51×10^{-1}	1.71×10^{-1}	1.61×10^{-1}
	0.85	1.16×10^{0}	2.55×10^{-1}	1.79×10^{-1}	1.95×10^{-1}	1.85×10^{-1}
	0.95	1.01×10^{0}	1.98×10^{-1}	1.44×10^{-1}	1.34×10^{-1}	1.27×10^{-1}
	1.1	9.96×10^{-1}	1.36×10^{-1}	1.08×10^{-1}	1.24×10^{-1}	1.19×10^{-1}
	1.3	1.23×10^{0}	2.47×10^{-1}	1.77×10^{-1}	1.48×10^{-1}	1.41×10^{-1}
	1.5	1.10×10^{0}	2.58×10^{-1}	1.76×10^{-1}	1.28×10^{-1}	1.23×10^{-1}
	1.7	9.68×10^{-1}	8.67×10^{-3}	8.67×10^{-3}	1.77×10^{-1}	1.72×10^{-1}
	1.9	9.06×10^{-1}	9.08×10^{-3}	9.08×10^{-3}	1.60×10^{-1}	1.56×10^{-1}
	2.1	8.37×10^{-1}	9.90×10^{-3}	9.90×10^{-3}	1.45×10^{-1}	1.41×10^{-1}
	2.3	8.08×10^{-1}	1.13×10^{-2}	1.13×10^{-2}	1.34×10^{-1}	1.30×10^{-1}
	2.5	7.64×10^{-1}	1.28×10^{-2}	1.28×10^{-2}	1.27×10^{-1}	1.23×10^{-1}
	2.7	7.16×10^{-1}	1.46×10^{-2}	1.46×10^{-2}	1.43×10^{-1}	1.26×10^{-1}
	2.9	6.80×10^{-1}	1.69×10^{-2}	1.68×10^{-2}	1.34×10^{-1}	1.19×10^{-1}
	3.1	6.54×10^{-1}	1.96×10^{-2}	1.95×10^{-2}	1.26×10^{-1}	1.12×10^{-1}
	3.3	6.16×10^{-1}	2.26×10^{-2}	2.23×10^{-2}	1.19×10^{-1}	1.06×10^{-1}
	3.5	6.00×10^{-1}	2.62×10^{-2}	2.58×10^{-2}	1.15×10^{-1}	1.03×10^{-1}
	3.7	6.72×10^{-1}	3.14×10^{-2}	3.09×10^{-2}	1.24×10^{-1}	1.10×10^{-1}
	3.9	5.34×10^{-1}	3.43×10^{-2}	3.36×10^{-2}	1.02×10^{-1}	9.30×10^{-2}
	4.2	5.07×10^{-1}	2.73×10^{-2}	2.68×10^{-2}	9.70×10^{-2}	8.95×10^{-2}
	4.8	4.01×10^{-1}	3.64×10^{-2}	3.56×10^{-2}	8.13×10^{-2}	8.33×10^{-2}
	5.5	2.89×10^{-1}	4.66×10^{-2}	4.46×10^{-2}	6.96×10^{-2}	1.05×10^{-1}
	6.5	2.97×10^{-1}	8.57×10^{-2}	7.32×10^{-2}	7.30×10^{-2}	1.43×10^{-1}
	7.5	5.35×10^{-1}	2.19×10^{-1}	1.37×10^{-1}	1.02×10^{-1}	1.96×10^{-1}
	8.5	4.68×10^{-1}	3.64×10^{-1}	1.74×10^{-1}	1.28×10^{-1}	2.39×10^{-1}
0%–10%	0.35	1.08×10^{0}	5.29×10^{-1}	2.72×10^{-1}	4.37×10^{-1}	4.03×10^{-1}
	0.45	1.18×10^{0}	4.65×10^{-1}	2.64×10^{-1}	4.37×10^{-1}	4.07×10^{-1}
	0.55	1.14×10^{0}	3.36×10^{-1}	2.15×10^{-1}	3.18×10^{-1}	2.98×10^{-1}
	0.65	1.18×10^{0}	3.36×10^{-1}	2.18×10^{-1}	2.96×10^{-1}	2.77×10^{-1}
	0.75	1.00×10^{0}	2.17×10^{-1}	1.55×10^{-1}	1.80×10^{-1}	1.70×10^{-1}
	0.85	1.07×10^{0}	2.40×10^{-1}	1.71×10^{-1}	1.78×10^{-1}	1.69×10^{-1}
	0.95	1.01×10^{0}	2.03×10^{-1}	1.50×10^{-1}	1.42×10^{-1}	1.35×10^{-1}
	1.1	9.36×10^{-1}	1.32×10^{-1}	1.06×10^{-1}	1.19×10^{-1}	1.14×10^{-1}
	1.3	1.13×10^{0}	2.29×10^{-1}	1.64×10^{-1}	1.36×10^{-1}	1.30×10^{-1}
	1.5	1.00×10^{0}	2.35×10^{-1}	1.61×10^{-1}	1.15×10^{-1}	1.10×10^{-1}
	1.7	8.59×10^{-1}	1.39×10^{-2}	1.39×10^{-2}	1.54×10^{-1}	1.49×10^{-1}
	1.9	7.93×10^{-1}	1.43×10^{-2}	1.43×10^{-2}	1.36×10^{-1}	1.32×10^{-1}
	2.1	7.04×10^{-1}	1.52×10^{-2}	1.52×10^{-2}	1.20×10^{-1}	1.17×10^{-1}
	2.3	6.74×10^{-1}	1.71×10^{-2}	1.71×10^{-2}	1.11×10^{-1}	1.07×10^{-1}
	2.5	6.25×10^{-1}	1.92×10^{-2}	1.92×10^{-2}	1.02×10^{-1}	9.90×10^{-2}
	2.7	6.10×10^{-1}	2.22×10^{-2}	2.22×10^{-2}	1.21×10^{-1}	1.07×10^{-1}
	2.9	5.87×10^{-1}	2.54×10^{-2}	2.54×10^{-2}	1.15×10^{-1}	1.02×10^{-1}
	3.1	4.84×10^{-1}	2.86×10^{-2}	2.83×10^{-2}	9.55×10^{-2}	8.58×10^{-2}
	3.3	5.06×10^{-1}	3.35×10^{-2}	3.32×10^{-2}	9.81×10^{-2}	8.76×10^{-2}
	3.5	4.79×10^{-1}	3.87×10^{-2}	3.82×10^{-2}	9.28×10^{-2}	8.31×10^{-2}
	3.7	5.06×10^{-1}	4.53×10^{-2}	4.46×10^{-2}	9.55×10^{-2}	8.53×10^{-2}
	3.9	5.11×10^{-1}	5.36×10^{-2}	5.27×10^{-2}	9.47×10^{-2}	8.51×10^{-2}
	4.2	3.67×10^{-1}	3.93×10^{-2}	3.87×10^{-2}	7.27×10^{-2}	6.69×10^{-2}
	4.8	2.49×10^{-1}	5.14×10^{-2}	5.02×10^{-2}	5.62×10^{-2}	5.52×10^{-2}
	5.5	2.18×10^{-1}	6.82×10^{-2}	6.58×10^{-2}	5.52×10^{-2}	6.55×10^{-2}
	6.5	5.70×10^{-3}	1.06×10^{-1}	7.89×10^{-2}	3.33×10^{-2}	8.70×10^{-2}
	7.5	5.82×10^{-1}	3.30×10^{-1}	2.23×10^{-1}	1.03×10^{-1}	1.54×10^{-1}
	8.5	5.02×10^{-1}	5.30×10^{-1}	2.81×10^{-1}	1.27×10^{-1}	1.89×10^{-1}

TABLE XII. $R_{AA}(p_T^e)$ for (upper) 10%–20% and (lower) 20%–40% centrality classes. The p_T^e is in units of GeV/c. The yield and corresponding uncertainties are in units of (GeV/c)$^{-2}$.

Centrality	p_T^e	R_{AA}	Stat. error (+)	Stat. error (−)	Sys. error (+)	Sys. error (−)
10%–20%	0.35	9.72×10^{-1}	4.76×10^{-1}	2.46×10^{-1}	3.66×10^{-1}	3.34×10^{-1}
	0.45	1.05×10^{0}	4.13×10^{-1}	2.36×10^{-1}	3.62×10^{-1}	3.33×10^{-1}
	0.55	1.09×10^{0}	3.22×10^{-1}	2.08×10^{-1}	2.92×10^{-1}	2.72×10^{-1}
	0.65	1.12×10^{0}	3.22×10^{-1}	2.11×10^{-1}	2.71×10^{-1}	2.53×10^{-1}
	0.75	1.01×10^{0}	2.20×10^{-1}	1.58×10^{-1}	1.77×10^{-1}	1.67×10^{-1}
	0.85	1.19×10^{0}	2.68×10^{-1}	1.91×10^{-1}	1.95×10^{-1}	1.85×10^{-1}
	0.95	9.82×10^{-1}	1.99×10^{-1}	1.48×10^{-1}	1.34×10^{-1}	1.28×10^{-1}
	1.1	9.76×10^{-1}	1.39×10^{-1}	1.12×10^{-1}	1.21×10^{-1}	1.16×10^{-1}
	1.3	1.22×10^{0}	2.45×10^{-1}	1.76×10^{-1}	1.48×10^{-1}	1.41×10^{-1}
	1.5	1.07×10^{0}	2.50×10^{-1}	1.72×10^{-1}	1.21×10^{-1}	1.16×10^{-1}
	1.7	9.63×10^{-1}	1.66×10^{-2}	1.66×10^{-2}	1.69×10^{-1}	1.64×10^{-1}
	1.9	8.92×10^{-1}	1.75×10^{-2}	1.75×10^{-2}	1.51×10^{-1}	1.47×10^{-1}
	2.1	8.47×10^{-1}	1.93×10^{-2}	1.93×10^{-2}	1.38×10^{-1}	1.34×10^{-1}
	2.3	8.41×10^{-1}	2.22×10^{-2}	2.22×10^{-2}	1.32×10^{-1}	1.27×10^{-1}
	2.5	7.65×10^{-1}	2.49×10^{-2}	2.49×10^{-2}	1.20×10^{-1}	1.16×10^{-1}
	2.7	6.98×10^{-1}	2.83×10^{-2}	2.83×10^{-2}	1.37×10^{-1}	1.20×10^{-1}
	2.9	6.38×10^{-1}	3.22×10^{-2}	3.22×10^{-2}	1.25×10^{-1}	1.10×10^{-1}
	3.1	6.53×10^{-1}	3.83×10^{-2}	3.80×10^{-2}	1.23×10^{-1}	1.09×10^{-1}
	3.3	5.78×10^{-1}	4.31×10^{-2}	4.26×10^{-2}	1.10×10^{-1}	9.82×10^{-2}
	3.5	6.16×10^{-1}	5.11×10^{-2}	5.04×10^{-2}	1.15×10^{-1}	1.02×10^{-1}
	3.7	7.14×10^{-1}	6.28×10^{-2}	6.19×10^{-2}	1.28×10^{-1}	1.13×10^{-1}
	3.9	4.24×10^{-1}	6.25×10^{-2}	6.12×10^{-2}	8.34×10^{-2}	7.60×10^{-2}
	4.2	5.55×10^{-1}	5.41×10^{-2}	5.33×10^{-2}	1.01×10^{-1}	9.19×10^{-2}
	4.8	3.88×10^{-1}	7.09×10^{-2}	6.93×10^{-2}	7.71×10^{-2}	7.19×10^{-2}
	5.5	2.91×10^{-1}	9.03×10^{-2}	8.70×10^{-2}	6.69×10^{-2}	7.76×10^{-2}
	6.5	4.83×10^{-1}	1.80×10^{-1}	1.71×10^{-1}	9.74×10^{-2}	1.27×10^{-1}
	7.5	9.99×10^{-1}	5.13×10^{-1}	3.35×10^{-1}	1.60×10^{-1}	1.97×10^{-1}
	8.5	8.03×10^{-1}	8.14×10^{-1}	3.96×10^{-1}	1.85×10^{-1}	2.37×10^{-1}
20%–40%	0.35	7.66×10^{-1}	3.76×10^{-1}	1.96×10^{-1}	2.82×10^{-1}	2.56×10^{-1}
	0.45	9.80×10^{-1}	3.87×10^{-1}	2.22×10^{-1}	3.22×10^{-1}	2.93×10^{-1}
	0.55	9.48×10^{-1}	2.80×10^{-1}	1.81×10^{-1}	2.43×10^{-1}	2.24×10^{-1}
	0.65	1.22×10^{0}	3.48×10^{-1}	2.27×10^{-1}	2.90×10^{-1}	2.70×10^{-1}
	0.75	9.71×10^{-1}	2.12×10^{-1}	1.53×10^{-1}	1.70×10^{-1}	1.60×10^{-1}
	0.85	1.23×10^{0}	2.75×10^{-1}	1.96×10^{-1}	1.97×10^{-1}	1.86×10^{-1}
	0.95	9.56×10^{-1}	1.94×10^{-1}	1.45×10^{-1}	1.32×10^{-1}	1.26×10^{-1}
	1.1	1.06×10^{0}	1.49×10^{-1}	1.21×10^{-1}	1.29×10^{-1}	1.24×10^{-1}
	1.3	1.29×10^{0}	2.61×10^{-1}	1.87×10^{-1}	1.51×10^{-1}	1.43×10^{-1}
	1.5	1.17×10^{0}	2.75×10^{-1}	1.88×10^{-1}	1.33×10^{-1}	1.27×10^{-1}
	1.7	1.05×10^{0}	1.81×10^{-2}	1.81×10^{-2}	1.90×10^{-1}	1.84×10^{-1}
	1.9	1.01×10^{0}	1.90×10^{-2}	1.90×10^{-2}	1.74×10^{-1}	1.68×10^{-1}
	2.1	9.43×10^{-1}	2.08×10^{-2}	2.08×10^{-2}	1.59×10^{-1}	1.55×10^{-1}
	2.3	8.91×10^{-1}	2.35×10^{-2}	2.35×10^{-2}	1.47×10^{-1}	1.42×10^{-1}
	2.5	8.66×10^{-1}	2.67×10^{-2}	2.67×10^{-2}	1.40×10^{-1}	1.36×10^{-1}
	2.7	8.20×10^{-1}	3.05×10^{-2}	3.05×10^{-2}	1.63×10^{-1}	1.44×10^{-1}
	2.9	8.10×10^{-1}	3.57×10^{-2}	3.57×10^{-2}	1.59×10^{-1}	1.40×10^{-1}
	3.1	7.91×10^{-1}	4.15×10^{-2}	4.15×10^{-2}	1.50×10^{-1}	1.33×10^{-1}
	3.3	7.57×10^{-1}	4.81×10^{-2}	4.77×10^{-2}	1.44×10^{-1}	1.28×10^{-1}
	3.5	6.83×10^{-1}	5.45×10^{-2}	5.38×10^{-2}	1.31×10^{-1}	1.17×10^{-1}
	3.7	7.51×10^{-1}	6.53×10^{-2}	6.45×10^{-2}	1.39×10^{-1}	1.23×10^{-1}
	3.9	5.91×10^{-1}	7.00×10^{-2}	6.89×10^{-2}	1.14×10^{-1}	1.04×10^{-1}
	4.2	5.79×10^{-1}	5.71×10^{-2}	5.63×10^{-2}	1.11×10^{-1}	1.02×10^{-1}
	4.8	5.21×10^{-1}	7.72×10^{-2}	7.57×10^{-2}	1.01×10^{-1}	1.11×10^{-1}
	5.5	3.55×10^{-1}	9.73×10^{-2}	9.42×10^{-2}	8.20×10^{-2}	1.48×10^{-1}
	6.5	4.11×10^{-1}	1.77×10^{-1}	1.67×10^{-1}	9.26×10^{-2}	1.91×10^{-1}
	7.5	2.05×10^{-1}	3.71×10^{-1}	2.14×10^{-1}	6.41×10^{-2}	2.23×10^{-1}
	8.5	4.42×10^{-1}	6.98×10^{-1}	3.33×10^{-1}	1.24×10^{-1}	2.81×10^{-1}

TABLE XIII. $R_{AA}(p_T^e)$ for (upper) 40%–60% and (lower) 60%–92% centrality classes. The p_T^e is in units of GeV/c. The yield and corresponding uncertainties are in units of (GeV/c)$^{-2}$.

Centrality	p_T^e	R_{AA}	Stat. error (+)	Stat. error (−)	Sys. error (+)	Sys. error (−)
40%–60%	0.35	7.29×10^{-1}	3.66×10^{-1}	2.01×10^{-1}	3.24×10^{-1}	3.03×10^{-1}
	0.45	1.04×10^{0}	4.19×10^{-1}	2.47×10^{-1}	3.40×10^{-1}	3.09×10^{-1}
	0.55	1.17×10^{0}	3.52×10^{-1}	2.33×10^{-1}	3.00×10^{-1}	2.77×10^{-1}
	0.65	1.10×10^{0}	3.28×10^{-1}	2.24×10^{-1}	2.63×10^{-1}	2.44×10^{-1}
	0.75	9.92×10^{-1}	2.29×10^{-1}	1.72×10^{-1}	1.81×10^{-1}	1.71×10^{-1}
	0.85	1.26×10^{0}	2.95×10^{-1}	2.18×10^{-1}	2.02×10^{-1}	1.91×10^{-1}
	0.95	1.17×10^{0}	2.49×10^{-1}	1.93×10^{-1}	1.59×10^{-1}	1.52×10^{-1}
	1.1	1.09×10^{0}	1.69×10^{-1}	1.41×10^{-1}	1.38×10^{-1}	1.32×10^{-1}
	1.3	1.49×10^{0}	3.02×10^{-1}	2.17×10^{-1}	1.83×10^{-1}	1.75×10^{-1}
	1.5	1.40×10^{0}	3.29×10^{-1}	2.25×10^{-1}	1.54×10^{-1}	1.47×10^{-1}
	1.7	1.19×10^{0}	2.80×10^{-2}	2.80×10^{-2}	2.19×10^{-1}	2.13×10^{-1}
	1.9	1.13×10^{0}	3.13×10^{-2}	3.13×10^{-2}	2.02×10^{-1}	1.97×10^{-1}
	2.1	1.14×10^{0}	3.62×10^{-2}	3.62×10^{-2}	1.93×10^{-1}	1.87×10^{-1}
	2.3	1.09×10^{0}	4.29×10^{-2}	4.29×10^{-2}	1.82×10^{-1}	1.77×10^{-1}
	2.5	1.10×10^{0}	5.04×10^{-2}	5.04×10^{-2}	1.77×10^{-1}	1.73×10^{-1}
	2.7	9.47×10^{-1}	5.75×10^{-2}	5.75×10^{-2}	1.94×10^{-1}	1.73×10^{-1}
	2.9	8.46×10^{-1}	6.63×10^{-2}	6.56×10^{-2}	1.75×10^{-1}	1.57×10^{-1}
	3.1	1.02×10^{0}	8.26×10^{-2}	8.17×10^{-2}	1.94×10^{-1}	1.73×10^{-1}
	3.3	8.30×10^{-1}	9.23×10^{-2}	9.09×10^{-2}	1.65×10^{-1}	1.48×10^{-1}
	3.5	8.44×10^{-1}	1.08×10^{-1}	1.06×10^{-1}	1.65×10^{-1}	1.48×10^{-1}
	3.7	1.04×10^{0}	1.33×10^{-1}	1.31×10^{-1}	1.90×10^{-1}	1.69×10^{-1}
	3.9	7.67×10^{-1}	1.42×10^{-1}	1.38×10^{-1}	1.49×10^{-1}	1.36×10^{-1}
	4.2	8.12×10^{-1}	1.17×10^{-1}	1.14×10^{-1}	1.52×10^{-1}	1.45×10^{-1}
	4.8	9.34×10^{-1}	1.73×10^{-1}	1.68×10^{-1}	1.68×10^{-1}	1.69×10^{-1}
	5.5	5.27×10^{-1}	2.03×10^{-1}	1.93×10^{-1}	1.16×10^{-1}	2.23×10^{-1}
	6.5	8.05×10^{-1}	4.40×10^{-1}	3.23×10^{-1}	1.60×10^{-1}	2.94×10^{-1}
	7.5	1.50×10^{-1}	8.27×10^{-1}	3.41×10^{-1}	7.53×10^{-2}	3.16×10^{-1}
60%–92%	0.35	1.11×10^{0}	5.69×10^{-1}	3.26×10^{-1}	4.14×10^{-1}	3.76×10^{-1}
	0.45	8.62×10^{-1}	3.80×10^{-1}	2.56×10^{-1}	3.25×10^{-1}	3.04×10^{-1}
	0.55	1.01×10^{0}	3.39×10^{-1}	2.51×10^{-1}	2.78×10^{-1}	2.59×10^{-1}
	0.65	1.25×10^{0}	4.05×10^{-1}	3.00×10^{-1}	2.95×10^{-1}	2.75×10^{-1}
	0.75	9.38×10^{-1}	2.64×10^{-1}	2.21×10^{-1}	1.86×10^{-1}	1.77×10^{-1}
	0.85	8.77×10^{-1}	2.78×10^{-1}	2.40×10^{-1}	1.74×10^{-1}	1.68×10^{-1}
	0.95	1.02×10^{0}	2.77×10^{-1}	2.39×10^{-1}	1.49×10^{-1}	1.43×10^{-1}
	1.1	1.14×10^{0}	2.22×10^{-1}	1.97×10^{-1}	1.44×10^{-1}	1.38×10^{-1}
	1.3	1.40×10^{0}	2.84×10^{-1}	2.05×10^{-1}	1.85×10^{-1}	1.78×10^{-1}
	1.5	1.30×10^{0}	3.07×10^{-1}	2.12×10^{-1}	1.67×10^{-1}	1.61×10^{-1}
	1.7	1.14×10^{0}	4.65×10^{-2}	4.65×10^{-2}	2.24×10^{-1}	2.19×10^{-1}
	1.9	1.05×10^{0}	5.45×10^{-2}	5.45×10^{-2}	2.05×10^{-1}	2.01×10^{-1}
	2.1	7.76×10^{-1}	6.15×10^{-2}	6.15×10^{-2}	1.72×10^{-1}	1.69×10^{-1}
	2.3	8.13×10^{-1}	7.61×10^{-2}	7.54×10^{-2}	1.70×10^{-1}	1.66×10^{-1}
	2.5	8.78×10^{-1}	9.29×10^{-2}	9.18×10^{-2}	1.71×10^{-1}	1.68×10^{-1}
	2.7	7.45×10^{-1}	1.07×10^{-1}	1.05×10^{-1}	1.78×10^{-1}	1.64×10^{-1}
	2.9	6.86×10^{-1}	1.25×10^{-1}	1.23×10^{-1}	1.67×10^{-1}	1.54×10^{-1}
	3.1	8.73×10^{-1}	1.57×10^{-1}	1.54×10^{-1}	1.86×10^{-1}	1.70×10^{-1}
	3.3	6.19×10^{-1}	1.74×10^{-1}	1.69×10^{-1}	1.52×10^{-1}	1.41×10^{-1}
	3.5	7.31×10^{-1}	2.10×10^{-1}	2.03×10^{-1}	1.63×10^{-1}	1.51×10^{-1}
	3.7	9.70×10^{-1}	2.62×10^{-1}	2.53×10^{-1}	1.92×10^{-1}	1.75×10^{-1}
	3.9	7.02×10^{-1}	2.89×10^{-1}	2.76×10^{-1}	1.54×10^{-1}	1.46×10^{-1}
	4.2	5.40×10^{-1}	2.17×10^{-1}	2.09×10^{-1}	1.28×10^{-1}	1.27×10^{-1}
	4.8	3.82×10^{-2}	2.49×10^{-1}	2.33×10^{-1}	7.09×10^{-2}	1.30×10^{-1}
	6.5	3.81×10^{-1}	9.20×10^{-1}	4.85×10^{-1}	1.13×10^{-1}	3.32×10^{-1}

TABLE XIV. p_T^e-integrated nuclear modification factors $R_{\rm AA}$.

p_T^e (GeV/c)	$N_{\rm part}$	$R_{\rm AA}$	Stat. error (+)	Stat. error (−)	Sys. error (±)	Common fractional error from $p + p$ cross section.
>0.30	14.5	1.04×10^{0}	7.65×10^{-2}	7.57×10^{-2}	3.89×10^{-1}	$+2.33 \times 10^{-1} - 1.59 \times 10^{-1}$
	59.95	9.86×10^{-1}	3.91×10^{-2}	3.87×10^{-2}	2.54×10^{-1}	
	140.4	9.44×10^{-1}	2.29×10^{-2}	2.26×10^{-2}	2.19×10^{-1}	
	234.6	1.03×10^{0}	2.39×10^{-2}	2.35×10^{-2}	2.43×10^{-1}	
	325.2	1.09×10^{0}	2.21×10^{-2}	2.18×10^{-2}	2.72×10^{-1}	
>0.60	14.5	1.04×10^{0}	7.20×10^{-2}	7.13×10^{-2}	3.50×10^{-1}	$+1.32 \times 10^{-1} - 1.04 \times 10^{-1}$
	59.95	9.86×10^{-1}	3.73×10^{-2}	3.69×10^{-2}	2.09×10^{-1}	
	140.4	9.44×10^{-1}	2.12×10^{-2}	2.10×10^{-2}	1.72×10^{-1}	
	234.6	1.03×10^{0}	2.12×10^{-2}	2.09×10^{-2}	1.60×10^{-1}	
	325.2	1.09×10^{0}	1.85×10^{-2}	1.82×10^{-2}	1.60×10^{-1}	
>0.80	14.5	1.07×10^{0}	7.34×10^{-2}	7.24×10^{-2}	3.33×10^{-1}	$+1.11 \times 10^{-1} - 9.07 \times 10^{-2}$
	59.95	1.21×10^{0}	3.86×10^{-2}	3.80×10^{-2}	1.99×10^{-1}	
	140.4	1.09×10^{0}	2.16×10^{-2}	2.13×10^{-2}	1.50×10^{-1}	
	234.6	1.04×10^{0}	2.15×10^{-2}	2.11×10^{-2}	1.36×10^{-1}	
	325.2	9.84×10^{-1}	1.83×10^{-2}	1.80×10^{-2}	1.30×10^{-1}	
>2.0	14.5	7.65×10^{-1}	3.39×10^{-2}	3.34×10^{-2}	2.64×10^{-1}	$+1.05 \times 10^{-1} - 8.65 \times 10^{-2}$
	59.95	1.04×10^{0}	1.90×10^{-2}	1.89×10^{-2}	1.94×10^{-1}	
	140.4	8.53×10^{-1}	1.04×10^{-2}	1.04×10^{-2}	1.39×10^{-1}	
	234.6	7.59×10^{-1}	9.72×10^{-3}	9.69×10^{-3}	1.15×10^{-1}	
	325.2	6.25×10^{-1}	7.58×10^{-3}	7.56×10^{-3}	9.94×10^{-2}	
>3.0	14.5	6.56×10^{-1}	7.85×10^{-2}	7.35×10^{-2}	2.23×10^{-1}	$+1.39 \times 10^{-1} - 1.09 \times 10^{-1}$
	59.95	8.79×10^{-1}	4.12×10^{-2}	3.99×10^{-2}	1.58×10^{-1}	
	140.4	6.83×10^{-1}	2.05×10^{-2}	2.02×10^{-2}	1.07×10^{-1}	
	234.6	5.80×10^{-1}	1.91×10^{-2}	1.87×10^{-2}	8.48×10^{-2}	
	325.2	4.47×10^{-1}	1.43×10^{-2}	1.40×10^{-2}	7.02×10^{-2}	
>4.0	14.5	2.35×10^{-1}	1.54×10^{-1}	1.23×10^{-1}	1.08×10^{-1}	$+1.37 \times 10^{-1} - 1.08 \times 10^{-1}$
	59.95	7.34×10^{-1}	8.45×10^{-2}	7.74×10^{-2}	1.35×10^{-1}	
	140.4	4.87×10^{-1}	3.97×10^{-2}	3.77×10^{-2}	8.36×10^{-2}	
	234.6	4.60×10^{-1}	3.88×10^{-2}	3.61×10^{-2}	7.15×10^{-2}	
	325.2	2.86×10^{-1}	2.75×10^{-2}	2.57×10^{-2}	5.30×10^{-2}	

TABLE XV. Heavy-flavor $e^{\pm}$ v_2 from Au + Au collisions, for the centralities indicated. The p_T is in units of GeV/c.

Centrality	p_T	v_2	Stat. error	Syst. error
0%–92%	0.55	4.01×10^{-2}	6.36×10^{-3}	1.89×10^{-2}
	0.65	4.08×10^{-2}	7.12×10^{-3}	1.88×10^{-2}
	0.75	3.85×10^{-2}	7.42×10^{-3}	1.68×10^{-2}
	0.85	6.26×10^{-2}	7.67×10^{-3}	1.45×10^{-2}
	0.95	6.25×10^{-2}	8.61×10^{-3}	1.37×10^{-2}
	1.09	5.63×10^{-2}	6.99×10^{-3}	1.18×10^{-2}
	1.29	6.98×10^{-2}	9.23×10^{-3}	1.15×10^{-2}
	1.52	9.20×10^{-2}	1.03×10^{-2}	1.12×10^{-2}
	1.83	8.70×10^{-2}	1.52×10^{-2}	1.07×10^{-2}
	2.20	6.92×10^{-2}	1.81×10^{-2}	9.31×10^{-3}
	2.70	7.06×10^{-2}	3.08×10^{-2}	8.42×10^{-3}
	3.24	3.08×10^{-2}	4.65×10^{-2}	7.89×10^{-3}
	4.05	9.86×10^{-3}	6.45×10^{-2}	9.57×10^{-3}
0%–20%	0.40	4.25×10^{-2}	8.06×10^{-3}	1.36×10^{-2}
	0.60	4.14×10^{-2}	5.86×10^{-3}	8.60×10^{-3}
	0.80	4.41×10^{-2}	6.01×10^{-3}	9.43×10^{-3}
	1.05	5.06×10^{-2}	6.37×10^{-3}	6.72×10^{-3}
	1.40	4.82×10^{-2}	6.77×10^{-3}	6.29×10^{-3}
	1.80	3.84×10^{-2}	1.11×10^{-2}	7.34×10^{-3}
	2.50	4.65×10^{-2}	1.45×10^{-2}	6.43×10^{-3}
	4.00	7.93×10^{-2}	3.70×10^{-2}	9.62×10^{-3}
20%–40%	0.40	6.55×10^{-2}	8.01×10^{-3}	1.82×10^{-2}
	0.60	7.34×10^{-2}	5.44×10^{-3}	1.36×10^{-2}
	0.80	1.12×10^{-1}	5.73×10^{-3}	1.05×10^{-2}
	1.05	9.47×10^{-2}	6.30×10^{-3}	1.01×10^{-2}
	1.40	1.30×10^{-1}	7.08×10^{-3}	8.69×10^{-3}
	1.80	1.27×10^{-1}	1.14×10^{-2}	8.36×10^{-3}
	2.50	8.48×10^{-2}	1.47×10^{-2}	8.17×10^{-3}
	4.00	8.15×10^{-2}	3.62×10^{-2}	6.29×10^{-3}
40%–60%	0.40	9.14×10^{-2}	1.57×10^{-2}	2.10×10^{-2}
	0.60	1.20×10^{-1}	1.13×10^{-2}	1.49×10^{-2}
	0.80	9.05×10^{-2}	1.31×10^{-2}	1.63×10^{-2}
	1.05	1.12×10^{-1}	1.49×10^{-2}	1.25×10^{-2}
	1.40	1.42×10^{-1}	1.73×10^{-2}	1.07×10^{-2}
	1.80	1.12×10^{-1}	2.88×10^{-2}	1.19×10^{-2}
	2.50	7.66×10^{-2}	3.53×10^{-2}	1.20×10^{-2}
	4.00	6.39×10^{-2}	8.55×10^{-2}	1.03×10^{-2}
0%–60%	0.40	5.35×10^{-2}	5.77×10^{-3}	1.86×10^{-2}
	0.60	5.82×10^{-2}	4.11×10^{-3}	1.29×10^{-2}
	0.80	6.75×10^{-2}	4.27×10^{-3}	1.27×10^{-2}
	1.05	6.85×10^{-2}	4.59×10^{-3}	9.98×10^{-3}
	1.40	7.97×10^{-2}	4.97×10^{-3}	8.96×10^{-3}
	1.80	7.04×10^{-2}	8.09×10^{-3}	9.88×10^{-3}
	2.50	6.08×10^{-2}	1.04×10^{-2}	9.20×10^{-3}
	4.00	7.81×10^{-2}	2.61×10^{-2}	1.06×10^{-2}

TABLE XVI. Differential invariant cross section of electrons $[(N_{e^+} + N_{e^-})/2]$ from heavy-flavor decays for 200 GeV $p + p$ collisions at midrapidity. The p_T^e is in units of GeV/c. The cross section and corresponding uncertainties are in units of mb.

p_T^e	Invariant yield	Stat. error	Sys. error
0.350	1.36×10^{-2}	4.45×10^{-3}	5.95×10^{-3}
0.450	6.05×10^{-3}	1.70×10^{-3}	2.39×10^{-3}
0.550	3.36×10^{-3}	7.56×10^{-4}	1.04×10^{-3}
0.650	1.81×10^{-3}	3.98×10^{-4}	5.12×10^{-4}
0.750	1.30×10^{-3}	2.28×10^{-4}	2.59×10^{-4}
0.850	7.50×10^{-4}	1.35×10^{-4}	1.35×10^{-4}
0.950	5.61×10^{-4}	9.14×10^{-5}	7.85×10^{-5}
1.10	3.18×10^{-4}	3.77×10^{-5}	3.64×10^{-5}
1.30	1.26×10^{-4}	2.10×10^{-5}	1.50×10^{-5}
1.50	6.58×10^{-5}	1.25×10^{-5}	6.56×10^{-6}
1.70	3.83×10^{-5}	2.07×10^{-6}	3.33×10^{-6}
1.90	1.89×10^{-5}	1.18×10^{-6}	1.65×10^{-6}
2.10	1.04×10^{-5}	7.44×10^{-7}	8.96×10^{-7}
2.30	6.08×10^{-6}	4.96×10^{-7}	5.09×10^{-7}
2.50	3.42×10^{-6}	3.63×10^{-7}	3.05×10^{-7}
2.70	2.06×10^{-6}	6.49×10^{-8}	2.80×10^{-7}
2.90	1.40×10^{-6}	4.77×10^{-8}	1.77×10^{-7}
3.10	8.64×10^{-7}	3.53×10^{-8}	1.10×10^{-7}
3.30	5.91×10^{-7}	2.73×10^{-8}	7.32×10^{-8}
3.50	4.11×10^{-7}	2.15×10^{-8}	4.90×10^{-8}
3.70	2.83×10^{-7}	1.70×10^{-8}	3.31×10^{-8}
3.90	1.91×10^{-7}	1.36×10^{-8}	2.26×10^{-8}
4.25	1.08×10^{-7}	5.95×10^{-9}	1.25×10^{-8}
4.75	4.84×10^{-8}	3.73×10^{-9}	5.53×10^{-9}
5.50	1.59×10^{-8}	1.79×10^{-9}	1.93×10^{-9}
6.50	5.30×10^{-9}	9.26×10^{-10}	6.03×10^{-10}
7.50	1.27×10^{-9}	5.73×10^{-10}	1.78×10^{-10}
8.50	8.19×10^{-10}	5.16×10^{-10}	8.85×10^{-11}

[1] K. Adcox *et al.* (PHENIX Collaboration), Nucl. Phys. A **757**, 184 (2005).
[2] I. Arsene *et al.* (BRAHMS Collaboration), Nucl. Phys. A **757**, 1 (2005).
[3] B. B. Back *et al.* (PHOBOS Collaboration), Nucl. Phys. A **757**, 28 (2005).
[4] J. Adams *et al.* (STAR Collaboration), Nucl. Phys. A **757**, 102 (2005).
[5] K. Adcox *et al.* (PHENIX Collaboration), Phys. Rev. Lett. **88**, 022301 (2001).
[6] S. S. Adler *et al.* (PHENIX Collaboration), Phys. Rev. Lett. **91**, 072301 (2003).
[7] J. Adams *et al.* (STAR Collaboration), Phys. Rev. Lett. **91**, 172302 (2003).
[8] P. Huovinen *et al.*, Phys. Lett. B **503**, 58 (2001).
[9] R. J. Fries, B. Muller, C. Nonaka, and S. A. Bass, Phys. Rev. C **68**, 044902 (2003).
[10] S. S. Adler *et al.* (PHENIX Collaboration), Phys. Rev. Lett. **91**, 182301 (2003).
[11] J. Adams *et al.* (STAR Collaboration), Phys. Rev. Lett. **92**, 052302 (2004).
[12] P. Arnold, J. Lenaghan, G. D. Moore, and L. G. Yaffe, Phys. Rev. Lett. **94**, 072302 (2005).
[13] D. Molnar and S. A. Voloshin, Phys. Rev. Lett. **91**, 092301 (2003).
[14] P. K. Kovtun, D. T. Son, and A. O. Starinets, Phys. Rev. Lett. **94**, 111601 (2005).
[15] D. Acosta *et al.*, Phys. Rev. Lett. **91**, 241804 (2003).
[16] M. Cacciari, Report No. LPTHE-P04-03, July 2004, p. 41.
[17] Y. L. Dokshitzer and D. E. Kharzeev, Phys. Lett. B **519**, 199 (2001).
[18] N. Armesto, A. Dainese, C. A. Salgado, and U. A. Wiedemann, Phys. Rev. D **71**, 054027 (2005).
[19] F. W. Busser *et al.*, Phys. Lett. B **53**, 212 (1974).
[20] C. Albajar *et al.* (UA1 Collaboration), Phys. Lett.B **256**, 121 (1991).
[21] O. Botner *et al.* (UA2 Collaboration), Phys. Lett. B **236**, 488 (1990).
[22] D. Acosta *et al.* (CDF collaboration), Phys. Rev. D **65**, 052007 (2002).
[23] S. Abachi *et al.* (D0 collaboration), Phys. Rev. Lett. **74**, 3548 (1995).
[24] K. Adcox *et al.* (PHENIX Collaboration), Phys. Rev. Lett. **88**, 192303 (2002).
[25] S. S. Adler *et al.* (PHENIX Collaboration), Phys. Rev. Lett. **96**, 032001 (2006).
[26] S. S. Adler *et al.* (PHENIX Collaboration), Phys. Rev. Lett. **94**, 082301 (2005).
[27] S. S. Adler *et al.* (PHENIX Collaboration), Phys. Rev. C **72**, 024901 (2005).
[28] S. S. Adler *et al.* (PHENIX Collaboration), Phys. Rev. Lett. **96**, 032301 (2006).
[29] A. Adare *et al.* (PHENIX Collaboration), Phys. Rev. Lett. **97**, 252002 (2006).
[30] A. Adare *et al.* (PHENIX Collaboration), Phys. Rev. Lett. **98**, 172301 (2007).
[31] K. Adcox *et al.* (PHENIX Collaboration), Nucl. Instrum. Methods Phys. Res., Sect. A **499**, 469 (2003).
[32] S. H. Aronson *et al.* (PHENIX Collaboration), Nucl. Instrum. Methods Phys. Res., Sect. A **499**, 480 (2003).
[33] K. Adcox *et al.* (PHENIX Collaboration), Nucl. Instrum. Methods Phys. Res., Sect. A **499**, 489 (2003).
[34] M. Aizawa *et al.* (PHENIX Collaboration), Nucl. Instrum. Methods Phys. Res., Sect. A **499**, 508 (2003).
[35] L. Aphecetche *et al.* (PHENIX Collaboration), Nucl. Instrum. Methods Phys. Res., Sect. A **499**, 521 (2003).
[36] M. Allen *et al.* (PHENIX Collaboration), Nucl. Instrum. Methods Phys. Res., Sect. A **499**, 549 (2003).
[37] C. Adler *et al.* (PHENIX Collaboration), Nucl. Instrum. Methods Phys. Res., Sect. A **470**, 488 (2001).
[38] Y. Akiba *et al.* (PHENIX Collaboration), Nucl. Instrum. Methods Phys. Res., Sect. A **433**, 143 (1999).
[39] S. S. Adler *et al.* (PHENIX Collaboration), Phys. Rev. C **71**, 034908 (2005).
[40] A. Adare *et al.* (PHENIX Collaboration), Phys. Rev. D **76**, 051106(R) (2007).
[41] S. S. Adler *et al.* (PHENIX Collaboration), Phys. Rev. Lett. **96**, 012304 (2006).
[42] S. S. Adler *et al.* (PHENIX Collaboration), Phys. Rev. Lett. **91**, 241803 (2003).
[43] R. J. Glauber and G. Matthiae, Nucl. Phys. B **21**, 135 (1970).
[44] M. L. Miller *et al.*, Annu. Rev. Nucl. Part. Sci. **57**, 205 (2007).
[45] D. Ben-Tzvi and M. B. Sandler, Patt. Rec. Lett. **11**, 167 (1990).
[46] M. Ohlsson *et al.*, Comput. Phys. Commun. **71**, 77 (1992).
[47] J. T. Myrhiem and L. Bugge, Nucl. Instrum. Methods Phys. Res., Sect. A **160**, 43 (1979).
[48] A. Chikanian *et al.*, Nucl. Instrum. Methods Phys. Res., Sect. A **371**, 480 (1996).
[49] *GEANT 3.2.1 Manual* (1994), CERN W5013, [http://wwwasdoc.web.cern.ch/wwwasdoc/pdfdir/geant.pdf].
[50] S. S. Adler *et al.* (PHENIX Collaboration), Phys. Rev. C **74**, 024904 (2006).
[51] S. S. Adler *et al.* (PHENIX Collaboration), Phys. Rev. Lett. **98**, 172302 (2007).
[52] T. Sjöstrand *et al.*, Comput. Phys. Commun. **135**, 238 (2001).
[53] A. Adare *et al.* (PHENIX Collaboration), Phys. Rev. Lett. **101**, 232301 (2008).
[54] S. S. Adler *et al.* (PHENIX Collaboration), Phys. Rev. C **69**, 034909 (2004).
[55] S. S. Adler *et al.* (PHENIX Collaboration), Phys. Rev. Lett. **96**, 202301 (2006).
[56] S. S. Adler *et al.* (PHENIX Collaboration), Phys. Rev. C **75**, 024909 (2007).
[57] A. Adare *et al.* (PHENIX Collaboration), Phys. Rev. D **83**, 032001 (2011).
[58] R. Averbeck, PHENIX Internal Note (2001).
[59] V. G. Ryabov, Nucl. Instrum. Methods Phys. Res., Sect. A **419**, 363 (1998).
[60] S. S. Adler *et al.* (PHENIX Collaboration), Phys. Rev. Lett. **98**, 012002 (2007).
[61] S. S. Adler *et al.* (PHENIX Collaboration), Phys. Rev. Lett. **94**, 232301 (2005).
[62] A. Adare *et al.* (PHENIX Collaboration), Phys. Rev. Lett. **104**, 132301 (2010).
[63] A. Adare *et al.* (PHENIX Collaboration), Phys. Rev. C **81**, 034911 (2010).
[64] A. Adare *et al.* (PHENIX Collaboration), Phys. Rev. D **82**, 012001 (2010).
[65] A. Adare *et al.* (PHENIX Collaboration) (unpublished).
[66] B. I. Abelev *et al.* (STAR Collaboration), Phys. Rev. C **80**, 064912 (2009).

[67] A. Adare *et al.* (PHENIX Collaboration), Phys. Lett. B **670**, 313 (2009).
[68] A. Frawley, T. Ullrich, and R. Vogt, Phys. Rep. **462**, 125 (2008).
[69] W. Vogelsang (private communication).
[70] J. Pumplin *et al.*, J. High Energy Phys. 07, (2002) 012.
[71] A. Adare *et al.* (PHENIX Collaboration), Phys. Rev. Lett. **98**, 232301 (2007).
[72] Y.-S. Tsai, Rev. Mod. Phys. **46**, 815 (1974).
[73] W. M. Yao *et al.*, J. Phys. **33**, 1 (2006).
[74] J.-Y. Ollitrault, arXiv:nucl-ex/9711003.
[75] A. M. Poskanzer and S. A. Voloshin, Phys. Rev. C **58**, 1671 (1998).
[76] A. Adare *et al.* (PHENIX Collaboration), Phys. Rev. Lett. **98**, 162301 (2007).
[77] M. Cacciari, P. Nason, and R. Vogt, Phys. Rev. Lett. **95**, 122001 (2005).
[78] H. Agakishiev *et al.* (STAR Collaboration), Phys. Rev. D **83**, 052006 (2011).
[79] S. S. Adler *et al.* (PHENIX Collaboration), Phys. Rev. D **74**, 072002 (2006).
[80] M. L. Mangano, P. Nason, and G. Ridolfi, Nucl. Phys. B **405**, 507 (1993).
[81] H. L. Lai *et al.*, Eur. Phys. J. C **12**, 375 (2000).
[82] A. Adare *et al.* (PHENIX Collaboration), Phys. Rev. Lett. **103**, 082002 (2009).
[83] N. Armesto *et al.*, Phys. Lett. B **637**, 362 (2006).
[84] G. D. Moore and D. Teaney, Phys. Rev. C **71**, 064904 (2005).
[85] H. van Hees, V. Greco, and R. Rapp, Phys. Rev. C **73**, 034913 (2006).
[86] H. van Hees, M. Mannarelli, V. Greco, and R. Rapp, Phys. Rev. Lett. **100**, 192301 (2008).
[87] P. B. Gossiaux and J. Aichelin, Phys. Rev. C **78**, 014904 (2008).
[88] P. B. Gossiaux, R. Bierkandt, and J. Aichelin, Phys. Rev. C **79**, 044906 (2009).
[89] P. B. Gossiaux and J. Aichelin, J. Phys. G **36**, 064028 (2009).
[90] S. Wicks *et al.*, Nucl. Phys. A **784**, 426 (2007).
[91] A. Adil and I. Vitev, Phys. Lett. B **649**, 139 (2007).
[92] O. Linnyk, E. Bratkovskaya, and W. Cassing, Int. J. Mod. Phys. E **17**, 1367 (2008).
[93] M. G. Mustafa, Phys. Rev. C **72**, 014905 (2005).
[94] C. Y. Wong, Phys. Rev. C **72**, 034906 (2005).
[95] B. I. Abelev *et al.* (STAR Collaboration), Phys. Rev. Lett. **97**, 152301 (2006).
[96] S. H. Lee, K. Ohnishi, S. Yasui, I. K. Yoo, and C. M. Ko, Phys. Rev. Lett. **100**, 222301 (2008).
[97] P. Sorensen and X. Dong, Phys. Rev. C **74**, 024902 (2006).
[98] G. Martinez-Garcia, S. Gadrat, and P. Crochet, Phys. Lett. B **663**, 533 (2008).
[99] V. Greco, C. Ko, and R. Rapp, Phys. Lett. B **595**, 202 (2004).
[100] B. Zhang, L. W. Chen, and C. M. Ko, Phys. Rev. C **72**, 024906 (2005).
[101] X. N. Wang and M. Gyulassy, Phys. Rev. D **44**, 3501 (1991).
[102] G. Policastro, D. T. Son, and A. O. Starinets, J. High Energy Phys. 09, (2002) 043.
[103] P. Danielewicz and M. Gyulassy, Phys. Rev. D **31**, 53 (1985).
[104] R. Rapp and H. van Hees, arXiv:0803.0901 [hep-ph].
[105] R. A. Lacey *et al.*, Phys. Rev. Lett. **98**, 092301 (2007).
[106] H.-J. Drescher, A. Dumitru, C. Gombeaud, and J.-Y. Ollitrault, Phys. Rev. C **76**, 024905 (2007).
[107] S. Gavin and M. Abdel-Aziz, Phys. Rev. Lett. **97**, 162302 (2006).
[108] A. Dumitru, E. Molnar, and Y. Nara, Phys. Rev. C **76**, 024910 (2007).
[109] P. Romatschke and U. Romatschke, Phys. Rev. Lett. **99**, 172301 (2007).
[110] M. Luzum and P. Romatschke, Phys. Rev. C **78**, 034915 (2008); **79**, 039903(E) (2009).